การพัฒนาโปรแกรมการวิเคราะห์เชิงคณิตศาสตร์สำหรับข้อมูลทางอินฟราเรด
สเปกโทรสโกปีของระบบหลายองค์ประกอบ

นายอรุณชัย ตั้งเจริญบำรุงสุข

DEVELOPMENT OF MATHEMATICAL ANALYSIS PROGRAM
FOR INFRARED SPECTROSCOPIC DATA
OF MULTICOMPONENT SYSTEM

Mr. Arunchai Tangcharoenbumrungsuk

Thesis Title   Development of Mathematical Analysis Program for Infrared Spectroscopic Data of Multicomponent System

By   Mr. Arunchai Tangcharoenbumrungsuk

Field of Study   Chemistry

Thesis Advisor   Assistant Professor Sanong Ekgasit, Ph.D.

Thesis Co-advisor Associate Professor Vudhichai Parasuk, Ph.D.

Accepted by the Faculty of Science, Chulalongkorn University in Partial Fulfillment of the Requirements for the Doctor's Degree

…………………………………………………………….. Dean of the Faculty of Science

(Professor Piamsak Menasveta, Ph.D.)

THESIS COMMITTEE

………………………………………………………………..……………… Chairman

(Associate Professor Sirirat Kokpol, Ph.D.)

………………………………………………………………..……………… Thesis Advisor

(Assistant Professor Sanong Ekgasit, Ph.D.)

………………………………………………………………..……………… Thesis Co-advisor

(Associate Professor Vudhichai Parasuk, Ph.D.)

………………………………………………………………..……………… Member

(Associate Professor Supot Hannongbua, Ph.D.)

………………………………………………………………..……………… Member

(Associate Professor Supason Wanichweacharangrung, Ph.D.)

………………………………………………………………..……………… Member

(Associate Professor Prapin Wilairat, Ph.D.)

อรุณชัย ตั้งเจริญบำรุงสุข : การพัฒนาโปรแกรมการวิเคราะห์เชิงคณิตศาสตร์สำหรับข้อมูล
ทางอินฟราเรดสเปกโทรสโกปีของระบบหลายองค์ประกอบ. (DEVELOPMENT OF
MATHEMATICAL ANALYSIS PROGRAM FOR INFRARED SPECTROSCOPIC
DATA OF MULTICOMPONENT SYSTEM) อาจารย์ที่ปรึกษา : ผศ. ดร. สนอง เอกสิทธิ์,
อาจารย์ที่ปรึกษาร่วม : รศ. ดร. วุฒิชัย พาราสุข, 119 หน้า. ISBN 974-17-6016-7

ได้ทำการพัฒนาเทคนิคการตรวจสอบองค์ประกอบของของผสมขึ้น โดยพัฒนาโปรแกรม
WizardIR รุ่น 1.0 เพื่อใช้ในการแยกอินฟราเรดสเปกตรัมของสารผสมพหุองค์ประกอบให้เป็น
เศษส่วนของปริมาตรและค่าคงตัวทางทัศนศาสตร์ของแต่ละองค์ประกอบในสารผสมโดยใช้การ
แยกชัดเส้นโค้งเชิงพหุตัวแปรและการแปลงคราเมอสโครนิก โปรแกรมที่พัฒนาอยู่ในสิ่งแวดล้อม
ของโปรแกรม MATLAB v6.5 ของบริษัท MathWorks ประสิทธิภาพและการพิสูจน์ความถูกต้อง
ของโปรแกรมหลักและ โปรแกรมย่อยได้รับการตรวจสอบจากแบบจำลองจากองค์ประกอบที่
ประดิษฐ์ขึ้นตามทฤษฎีคลาสสิคัลฮาร์มอนิก ผลการทำนายของโปรแกรมสอดคล้องกับตัวแปรที่ตั้ง
ไว้เป็นอย่างดี เทคนิคที่พัฒนาขึ้นสามารถใช้ในการวิเคราะห์องค์ประกอบของการทดลองจริง โดย
ใช้วิเคราะห์สเปกตรัมจากการทดลองของระบบที่เกิดการระเหยของ acetone, methanol และ
toluene โดยใช้การทดลองแบบแอตเทนูเอเทดโททัลอินเทอนาลรีแฟลกชัน ผลการวิเคราะห์จาก
โปรแกรมสอดคล้องเป็นอย่างดีกับสเปกตรัมอ้างอิงของสารประกอบบริสุทธิ์แต่ละชนิด นอกจาก
นั้นยังได้ใช้เทคนิคที่พัฒนาขึ้นสำหรับศึกษาระบบการเกิดผลึกของพอลิเมอร์ poly(3-
hydroxybutyrate-CO-3-hydroxyhexanoate) สเปกตรัมซึ่งขึ้นกับเวลาของพอลิเมอร์ได้ถูกวิเคราะห์
เพื่อให้ทราบถึงพฤติกรรมของการเกิดผลึกของแต่ละองค์ประกอบในระบบ

ภาควิชา ....เคมี............. ลายมือชื่อนิสิต ....

สาขาวิชา ....เคมี............. ลายมือชื่ออาจารย์ที่ปรึกษา ....

ปีการศึกษา ....2547............. ลายมือชื่ออาจารย์ที่ปรึกษาร่วม ....

ARUNCHAI TANGCHAROENBUMRUNGSUK : DEVELOPMENT OF MATHEMATICAL ANALYSIS PROGRAM FOR INFRARED SPECTROSCOPIC DATA OF MULTICOMPONENT SYSTEM. THESIS ADVISOR : ASST. PROF. SANONG EKGASIT, THESIS CO-ADVISOR : ASSOC. PROF. VUDHICHAI PARASUK, 119 pp. ISBN: 974-17-6016-7.

A technique for characterization of multicomponent system has been developed. The program WizardIR version 1.0 was developed to resolve the infrared spectra of multicomponent mixtures in order to reveal the profiles of volume fractions and optical constants of each component in the mixtures by multivariate curve resolution and Kramers-Kronig transformations. The program was implemented in MATLAB v6.5 (MathWorks, Inc.). The efficiency and validation of the program and the subprograms were tested with simulated spectra which were generated via classical harmonic theory. The program predictions agreed very well with the preset values. The program was later used to resolve the experimental spectra of evaporating system of acetone, methanol and toluene obtained using attenuated total internal reflection. The results agreed very well with the reference spectra of each pure compound. In addition, the program was used to study the crystallization of poly(3-hydroxybutyrate-*co*-3-hydroxyhexanoate). The time-dependent spectra of the polymer were resolved to obtain the behavior of crystallization of each component in the system.

Department ....Chemistry........ Student's signature ....

Field of study ....Chemistry........ Advisor's signature ....

Academic year ....2004........ Co-advisor's signature ....

ACKNOWLEDGEMENTS

CONTENTS

Pages

LIST OF FIGURES

Pages

LIST OF TABLES

CHAPTER I

INTRODUCTION

1.1 Research Inspiration

Infrared (IR) spectroscopy has been well established since the early 1970s, with the commercial development of Fourier transform infrared (FT-IR) spectrometers, which were first available in 1975. Nowadays, FT-IR spectroscopy has become a common technique for identification and classification of unknown samples due to the highly molecular specific fingerprints of the vibrational spectra.[1] The instrumental evolution of the FT-IR technique, accompanied by developments of both new accessories and auxiliary optics, is continually being made in order to access a wide range of samples. However, problems occur when infrared spectra are obtained under some situations, such as:

(*i*) Infrared spectra under different experimental setups, *i.e.*, different modes of reflection technique and different angles of incidence show different features. As a result, development of infrared characterization technique that do not depend on the experimental setups is of interest.

(*ii*) The complication and variation of multicomponent samples, such as biological samples and chemical waste make separation techniques such as high-performance liquid chromatography (HPLC), gas chromatography (GC), capillary electrophoresis (CE) impractical in laboratories. In addition, these techniques produce more chemical wastes in the analytical process. The characteristic absorption bands, which are directly related to chemical structure and compositions would represent all components in an unknown sample and bring about the problem of spectral interpretation. Our focus lies on how to resolve complex observed spectra and perform the identification with high accuracy.

To overcome the problems described above, mathematical analysis and chemometric methods are employed. Since the optical constants are the intrinsic

properties of materials and do not depend on experimental setups, it can be used for characterizing a sample for different experimental setups. However, the optical constants cannot be measured directly. To obtain the optical constants, mathematical analysis, such as Kramers-Kronig transformation, has to be applied on the observed spectrum. Although the highly-overlapped bands of multicomponent samples are complicated, chemometric methods with various mathematical tools such as principal component analysis and multivariate curve resolution can be employed for resolving the complex spectra of mixture.

1.2 Generalization of Chemometrics and Factor Analysis

Chemometrics is a chemical discipline that uses mathematics, statistics, and formal logic to: [2-3]

        a) design or select optimal experimental procedures.

        b) provide maximum relevant chemical information.

        c) obtain knowledge about chemical systems.

Chemometric methods such as factor analysis, principal component analysis and multivariate curve resolution basically treat the spectra as a data matrix ($\mathbf{D}$) consisting of r rows of wavenumbers or spectral channels and c columns of samples.

$$\mathbf{D} = \begin{array}{c} \text{column designee} \\ \text{row designee} \begin{bmatrix} d_{11} & d_{12} & d_{13} & ... & d_{1c} \\ d_{21} & d_{22} & d_{23} & ... & d_{2c} \\ d_{31} & d_{32} & d_{33} & ... & d_{2c} \\ \vdots & \vdots & \vdots & & \vdots \\ d_{r1} & d_{r2} & d_{r3} & ... & d_{rc} \end{bmatrix} \end{array} \qquad (1.1)$$

The row and column headings of the matrix are called *designee*. The symbol d_{ik} represents the data point associated with the ith row and k^{th} column of the matrix.

In the factor analysis, it is assumed that each point in the data matrix must be a linear sum of product terms. The number of terms in the sum, *n*, is called the *number of factors*. The d_{ik} can be expressed as:

$$d_{ik} \;=\; \sum_{j=1}^{n} r_{ij} c_{jk} \qquad (1.2)$$

where r_{ij} and c_{jk} are called row and column factors, respectively.

For data modeled by eq. 1.2, the data matrix can be decomposed into two matrices

$$\mathbf{D} \;=\; \mathbf{R}_{abstract} \cdot \mathbf{C}_{abstract} \qquad (1.3)$$

data matrix   row matrix   column matrix

where

factor

$$\mathbf{R}_{abstract} = \text{row designee} \begin{bmatrix} r_{11} & r_{12} & r_{13} & \cdots & r_{1n} \\ r_{21} & r_{22} & r_{23} & \cdots & r_{2n} \\ r_{31} & r_{32} & r_{33} & \cdots & r_{2n} \\ \vdots & \vdots & \vdots & & \vdots \\ r_{r1} & r_{r2} & r_{r3} & \cdots & r_{rn} \end{bmatrix}$$

column designee

$$\mathbf{C}_{abstract} = \text{factor} \begin{bmatrix} c_{11} & c_{12} & c_{13} & \cdots & c_{1c} \\ c_{21} & c_{22} & c_{23} & \cdots & c_{2c} \\ c_{31} & c_{32} & c_{33} & \cdots & c_{2c} \\ \vdots & \vdots & \vdots & & \vdots \\ c_{n1} & c_{n2} & c_{n3} & \cdots & c_{nc} \end{bmatrix}.$$

Since this solution is purely mathematical, it devoids physical meaning. These matrices are called *abstract matrices*. Explicitly, the factor analytical solution isolates the row-designee factors from the column-designee factors.

The following step of the factor analysis is the development of a complete and physically meaningful model for the data. In an attempt to achieve the mathematical

solution, the abstract factors are "transformed" into physically significant, "real" factors. Even though transforming the abstract solution into a real solution is difficult, this step is the goal of factor analysis.

To carry out the transformations, an appropriate information matrix $\mathbf{T}$ is required. By postmultiplying $\mathbf{R}_{abstract}$ by $\mathbf{T}$ and premultiplying $\mathbf{C}_{abstract}$ by the inverse of the transformation $\mathbf{T^{-1}}$, the data matrix in eq. 1.3 can be expressed as[3]

$$
\begin{aligned}
\mathbf{D} \quad &= \quad \left\{\mathbf{R}_{abstract}\mathbf{T}\right\} \cdot \left\{\mathbf{T^{-1}C}_{abstract}\right\} \\
&= \quad \mathbf{R}_{transformed} \cdot \mathbf{C}_{transformed} \qquad\qquad (1.4)
\end{aligned}
$$

If the transformed solution can be shown to have physical significance, a real solution to the problem can be found, thus

$$
\mathbf{D} \quad = \quad \mathbf{X}_{real}\mathbf{Y}_{real} \qquad\qquad (1.5)
$$

where $\mathbf{X}_{real} = \mathbf{R}_{transformed}$ and $\mathbf{Y}_{real} = \mathbf{C}_{transformed}$.

1.3 Objectives of this Research

The objectives of this research is to develop a program for resolving the infrared spectra of multicomponent mixture to reveal the profiles of volume fractions and optical constants of each component in the mixture.

1.4 Scope of this Research

In this research, the program WizardIR version 1.0 was developed. The program was written in MATLAB v6.5 (MathWorks, Inc.). The main application here is to resolve the infrared spectra of multicomponent mixture using the chemometric methods such as principal component analysis and multivariate curve resolution. The final results are the profiles of each component which are used to determine the optical constants (*n* and *k*) via Kramers-Kronig transformations. The program was validated with simulated spectra. The program is then applied to the experimental

spectra of the mixture of acetone, methanol and toluene. In addition, the program was tested with the polymer crystallization of poly(3-hydroxybutyrate-*co*-3-hydroxyhexanoate).

CHAPTER II

THEORETICAL CONSIDERATION

This chapter summaries methodologies of the mathematical analysis of the developed techniques. As stated earlier, the aim of this research was to resolve the infrared spectra of multicomponent mixtures to reveal the optical constants and concentrations (or volume fractions) of each component. Therefore, the mathematical analysis used in this research was divided into 3 parts:

    2.1 Optical constants determination

    2.2 Spectral resolution

    2.3 Absorptance of multicomponent mixtures

2.1 Optical Constants Determination

Since the optical constants are intrinsic properties of materials that do not depend on experimental setups, the observed spectra can be employed for the calculation of the optical constants.[4-5] Optical constants, or sometimes called complex refractive index ($\hat{n}$), are composed of 2 parts: refractive index n and absorption index k. Both n and k depend on frequency or wavenumber of light.

In infrared spectroscopy, there are several methods for determining the n and k of materials.[5] For example:

- Photometric method: the method measures the spectra with s- and p-polarization and solves for n and k via Fresnel equation.
- Polarimetric method: the method measures the spectra for various angles of incidence and solves for n and k via Fresnel equation.
- Special method: the method measures the spectra in reflection and transmission modes simultaneously and solves for n and k via Fresnel equation.

These methods have disadvantages such as

- It is not possible to obtain absolute pure *s*- and *p*-polarized lights when using polarizer.
- Various angles of incidence cannot be set with a high precision and the certain accessories are required at high cost.
- Measurement of reflection and transmission simultaneously is not available in commonly available instrument.

The aim of this work is to determine the n and k from a single spectrum by the Kramers-Kronig transformations. There are four theoretical aspects:

2.1.1   Kramers-Kronig transformations of n and k

2.1.2   Fresnel equation

2.1.3   Kramers-Kronig transformations from reflectance to phase shift

2.1.4   Conversion of reflectance to n and k

2.1.1 Kramers-Kronig Transformations of n and k

The Kramers-Kronig (KK) transformations, based on the principle of causality, connect the real and imaginary parts of many complex quantities in physics.[6] The transformations are valid for any complex functions that meet certain conditions.[4] The derivation of Kramers-Kronig transformations are given in Refs. 4 and 7. The general formulas are

$$f_R(z_0) \quad = \quad \frac{2}{\pi} P \int_0^\infty \frac{z \cdot f_I(z)}{z^2 - z_0^2} dz \qquad (2.1)$$

$$f_I(z_0) \quad = \quad -\frac{2z_0}{\pi} P \int_0^\infty \frac{f_R(z)}{z^2 - z_0^2} dz \qquad (2.2)$$

where $f_R(z)$ and $f_I(z)$ are the real and imaginary parts of the complex function of argument z, z_0 is a point in z that a pole is created when $z = z_0$, and P is the principal value of integration (usually taken to be 1).

In infrared spectroscopy, the complex refractive index also hold the conditions of Kramers-Kronig transformation. As a result, the n and k are related as

$$n(\nu_a) \quad = \quad n_\infty + \frac{2}{\pi} P \int_0^\infty \frac{\nu \cdot k(\nu)}{\nu^2 - \nu_a^2} d\nu \tag{2.3}$$

$$k(\nu_a) \quad = \quad -\frac{2\nu_a}{\pi} P \int_0^\infty \frac{n(\nu) - n_\infty}{\nu^2 - \nu_a^2} d\nu \tag{2.4}$$

where n_∞ is the refractive index at infinite wavenumber.

According to the literatures,[6,8-9] there are (at least) 3 methods for evaluating the integration in eqs. 2.3 and 2.4.

  a) Numerical integration such as trapezoidal and Simpson's rules
  b) Maclaurin's formula
  c) Successive double Fourier transforms

Ohta and Ishida[8] compared the accuracy of these methods, and concluded that Maclaurin's formula is the best technique. The Maclaurin's formula for n and k transformations are:

$$n(\nu_i) \quad = \quad n_\infty + \frac{2}{\pi} \sum_{j=1}^m \frac{\nu_j \cdot k(\nu_j)}{\nu_j^2 - \nu_i^2} \Delta \nu_j \tag{2.5}$$

$$k(\nu_i) \quad = \quad -\frac{2\nu_i}{\pi} \sum_{j=1}^m \frac{n(\nu_j) - n_\infty}{\nu_j^2 - \nu_i^2} \Delta \nu_j \tag{2.6}$$

where m is the number of wavenumbers. The singularity in eqs. 2.5 and 2.6 are avoided by integrating as

when i is odd, $j = 2, 4, 6, \ldots, i-1, i+1, \ldots$
when i is even, $j = 1, 3, 5, \ldots, i-1, i+1, \ldots$

However, in the case of transformation from n to k, it may contain negative values due to the incomplete decay of n to n_∞. In this work, the non-negativity is suggested to improve the accuracy of transformation. The results were demonstrated in Section 4.2.1.

2.1.2 Fresnel Equation

The relationships among the complex reflectivity $\hat{r}$, reflectance R and phase shift δ are given by the following expression.[5-6]

$$\hat{r} \quad = \quad \sqrt{R} \cdot e^{i\delta} \tag{2.7a}$$

and

$$\ln \hat{r} \quad = \quad \frac{1}{2}\ln R + i\delta \tag{2.7b}$$

By applying the Euler's formula,[10] the equation 2.7 can be rewritten as

$$
\begin{aligned}
\hat{r} \quad &= \quad \sqrt{R}\left(\cos\delta + i\sin\delta\right) \\
&= \quad \sqrt{R}\cos\delta + i\sqrt{R}\sin\delta
\end{aligned}
\tag{2.8}
$$

Therefore, the formulas of reflectance and phase shift are given in term of the complex reflectivity:

$$R \quad = \quad \left|\hat{r}\right|^2 \quad = \quad \mathrm{real}\left(\hat{r}\right)^2 + \mathrm{imag}\left(\hat{r}\right)^2 \tag{2.9}$$

$$\delta \quad = \quad \arctan\left[\frac{\mathrm{imag}\left(\hat{r}\right)}{\mathrm{real}\left(\hat{r}\right)}\right] \tag{2.10}$$

The Fresnel equation can be expressed in term of optical constants, according to the setup shown in Figure 2.1 by:

$$\hat{r}_s \quad = \quad \frac{n_0\cos\theta_0 - \hat{n}_1\cos\hat{\theta}_1}{n_0\cos\theta_0 + \hat{n}_1\cos\hat{\theta}_1} \tag{2.11}$$

and

$$\hat{r}_p \quad = \quad \frac{\hat{n}_1\cos\theta_0 - n_0\cos\hat{\theta}_1}{\hat{n}_1\cos\theta_0 + n_0\cos\hat{\theta}_1} \tag{2.12}$$

where θ_0 is the angle of incidence, n_0 is the refractive index of the incident media, $\hat{\theta}_1$ is the complex angle of refracted beam, $\hat{n}_1$ is the complex refractive index of the sample, and the subscription '*s*' and '*p*' indicate *s*- or *p*-polarization, respectively.
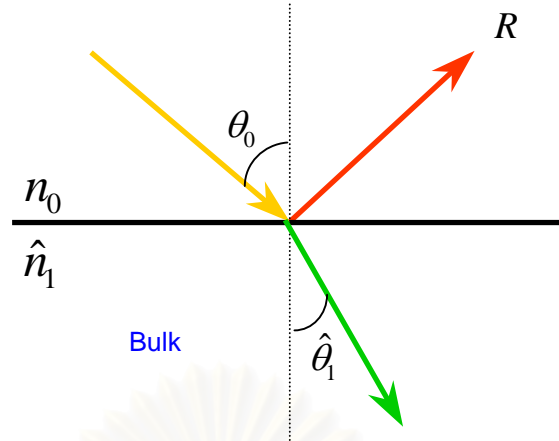
Figure 2.1 Optical configuration for light impinging on a flat surface.

According to the Snell's law[5]: $n_0 \sin \theta_0 = \hat{n}_1 \sin \hat{\theta}_1$, the eqs. 2.11 and 2.12 can be rewritten as

$$\hat{r}_s = \frac{n_0 \cos \theta_0 - \left(\hat{n}_1^2 - n_0^2 \sin^2 \theta_0 \right)^{\frac{1}{2}}}{n_0 \cos \theta_0 + \left(\hat{n}_1^2 - n_0^2 \sin^2 \theta_0 \right)^{\frac{1}{2}}} \quad (2.13)$$

and

$$\hat{r}_p = \frac{\hat{n}_1 \cos \theta_0 - n_0 \left(\hat{n}_1^2 - n_0^2 \sin^2 \theta_0 \right)^{\frac{1}{2}}}{\hat{n}_1 \cos \theta_0 + n_0 \left(\hat{n}_1^2 - n_0^2 \sin^2 \theta_0 \right)^{\frac{1}{2}}} \quad (2.14)$$

By different setting of n_1, n_0 and θ_0, three phenomena of reflections: external, internal and total internal reflections are observed and shown in Figure 2.2. The results for *s*- and *p*-polarizations were demonstrated in Section 4.2.2.

Fresnel Equation and Surface Plasmon Resonance Spectroscopy

Surface plasmon resonance (SPR) spectroscopy is a surface characterization technique that takes advantage of the enhanced evanescent field at the surface of a thin noble metal surface. The reflectance of an SPR curve is governed by the refractive index of the prism n_P, and layer architecture of a plane-boundary multilayer attached to the prism.
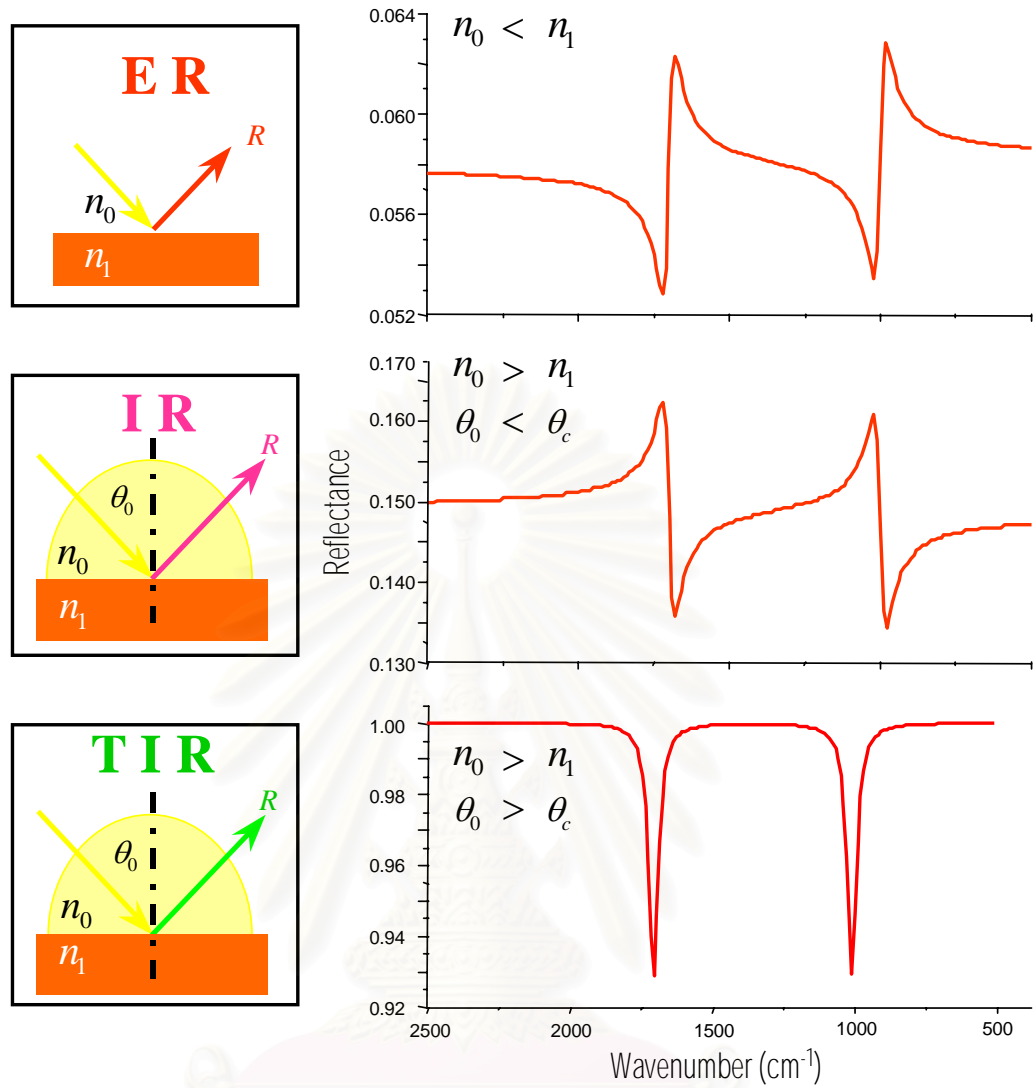
Figure 2.2 Three modes of reflection: external (upper), internal (middle) and total internal reflections (lower).

In an SPR setup under the Kretschmann-Raether ATR configuration, a thin noble metal film (*i.e.*, gold or silver with or without an adhesion promoter, for example, chromium or titatium) is deposited to the surface of a high refractive index prism. A dielectric substrate is then brought into contact with the metal film.[37]

For a simple three-phase system consisting of prism P/metal file M/dielectric substrate DS, the Fresnel complex reflectivity of a parallel-polarized radiation ($\hat{r}_{\parallel}$) can be expressed as below

$$\hat{r}_{\parallel} \quad = \quad \frac{\hat{r}_{P,M} + \hat{r}_{M,DS}e^{i2k_{ZM}d_M}}{1 + \hat{r}_{P,M}\hat{r}_{M,DS}e^{i2k_{ZM}d_M}} \qquad (2.15)$$

where $\hat{r}_{A,B}$ indicates reflection coefficient at the interface of media A and B, which is given by

$$\hat{r}_{A,B} \quad = \quad \frac{k_{zA}/\hat{n}_A^2 - k_{zB}/\hat{n}_B^2}{k_{zA}/\hat{n}_A^2 + k_{zB}/\hat{n}_B^2} \tag{2.16}$$

k_{zA} is the z-component of the wavevector in media A, which is given by

$$k_{zA} \quad = \quad \left[\left(\frac{2\pi}{\lambda}\right)^2 \hat{n}_A^2 - \left(\frac{2\pi}{\lambda}\right)^2 n_P^2 \sin^2\theta_0 \right]^{1/2} \tag{2.17}$$

and d_M is the thickness of metal film. The reflectance R is expressed in term of the complex reflectivity by $R = \left|\hat{r}_\parallel\right|^2$.

For a typical example of SPR system consisting of prism/metal film/nonabsorbing dielectric substrate with $n_P = 1.8458$, $\hat{n}_M = 0.1866 + 3.4835i$, $d_M = 50$ nm, and $n_{DS} = 1.333$, a conventional angle-scan SPR curve at $\lambda = 632.8$ nm was shown in Figure 2.3.
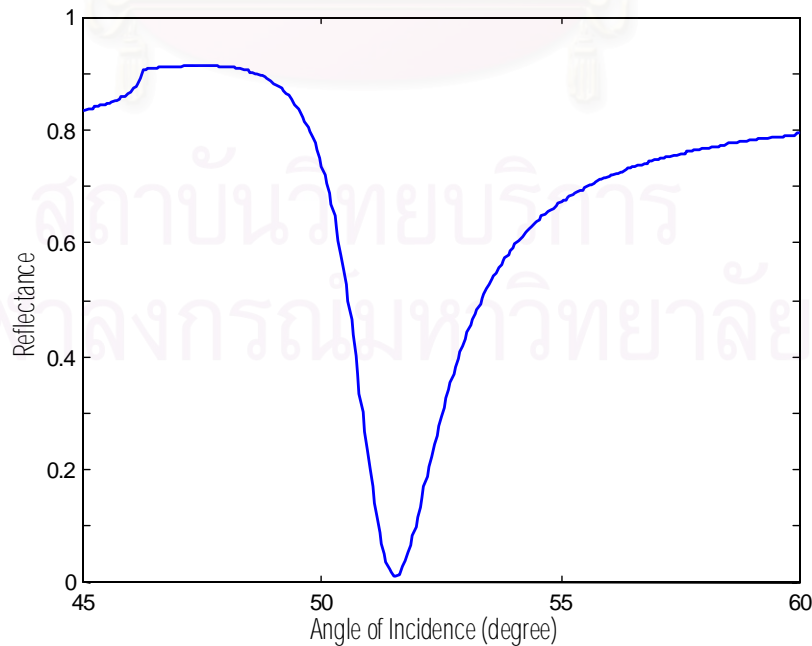
Figure 2.3 Conventional angle-scan SPR curve of prism/metal film/nonabsorbing dielectric substrate.

Under the total internal reflection condition, the reflectance can be expressed as the following equation:

$$R \quad = \quad 1 - \left(\frac{2\pi}{\lambda}\right)^2 \frac{1}{k_{zP}} \sum_{j=1}^{N} \left[\int_{z_j}^{z_{j+1}} \mathrm{Im}(\hat{\varepsilon}_j) \left\langle E_z^2(\theta_0) \right\rangle dz \right] \qquad (2.18)$$

where $\hat{\varepsilon}_j$ is the complex dielectric constant of the jth layer and $\left\langle E_z^2(\theta_0) \right\rangle$ is the mean square evanescent field at a distance z from the prism/metal interface. N is the number of the dielectric film that attached on the prism.

2.1.3 Kramers-Kronig Transformations from Reflectance to Phase Shift

Yamamoto et al.[11-13] introduced the equations for transformation of reflectance to phase shift as:

$$\delta_s(v_a) \quad = \quad -\frac{v_a}{\pi} \int_0^\infty \frac{\ln\left[R_s(v)\right] - \ln\left[R_s(v_a)\right]}{v^2 - v_a^2} dv \qquad (2.19)$$

$$\delta_p(v_a) \quad = \quad \frac{v_a}{\pi} \int_0^\infty \frac{\ln\left[R_p(v)\right] - \ln\left[R_p(v_a)\right]}{v^2 - v_a^2} dv \qquad (2.20)$$

Bertie et al.[14-15] introduced the another equation for both s- and p-polarizations as below

$$\delta(v_a) \quad = \quad -\frac{2}{\pi} \int_0^\infty \frac{v \ln\left[R(v)\right]^{1/2}}{v^2 - v_a^2} dv \qquad (2.21)$$

According to our investigation, Yamamoto's approach gave a better result in the case of external and internal reflections while Bertie's approach worked well for the case of total internal reflection. In this work, both approaches were employed and the results are shown in Section 4.2.3.

2.1.4 Conversion of Reflectance to n and k

In this section, the equations used to determine the n and k from reflectance were derived by assuming an isotropic media.

According to the Fresnel's equation, complex reflectivity are expressed as

$$\hat{r} = \frac{\hat{n}_1 \cos \hat{\theta}_1 - n_0 \cos \theta_0}{\hat{n}_1 \cos \hat{\theta}_1 + n_0 \cos \theta_0}$$

The above expression can be rewritten as:

$$\frac{1+\hat{r}}{1-\hat{r}} = \frac{\hat{n}_1 \cos \hat{\theta}_1}{n_0 \cos \theta_0} \tag{2.22}$$

By taking square of eq. 2.22 and applying the Snell's law, the eq. 2.23 is obtained.

$$\frac{\hat{n}_1^2}{n_0^2} = \sin^2 \theta_0 + \left(\frac{1+\hat{r}}{1-\hat{r}}\right)^2 \cos^2 \theta_0 \tag{2.23}$$

The term in bracket of eq. 2.23 can be rewritten in term of R and δ as

$$\frac{1+\hat{r}}{1-\hat{r}} = \frac{\left(1+\hat{r}\right)\cdot\left(1-\hat{r}^*\right)}{\left(1-\hat{r}\right)\cdot\left(1-\hat{r}^*\right)} = \frac{1-\hat{r}^* + \hat{r} - \hat{r}^2}{1-\hat{r}-\hat{r}^* - \hat{r}^2}$$

$$= \frac{1-R+\left(2\sqrt{R}\sin\delta\right)i}{1+R-\left(2\sqrt{R}\cos\delta\right)} \tag{2.24}$$

where the superscription * represents the conjugate of the complex number. By substituting eq. 2.24 into eq. 2.23, the following equation is obtained.

$$\frac{\hat{n}_1^2}{n_0^2} = \sin^2 \theta_0 + \frac{\cos^2 \theta_0 \left[(1-R)^2 - 4R\sin^2 \delta\right]}{\left(1+R-2\sqrt{R}\cos\delta\right)^2} + \frac{\cos^2 \theta_0 \left[4(1-R)\sqrt{R}\sin\delta\right]}{\left(1+R-2\sqrt{R}\cos\delta\right)^2}i \tag{2.25}$$

Since the complex dielectric constant ($\hat{\varepsilon}$) is defined as

$$\hat{\varepsilon} \quad = \quad \hat{n}_1^2 \quad = \quad \varepsilon' + \varepsilon''i \tag{2.26}$$

$$= \quad n_1^2 - k_1^2 + 2n_1k_1i \tag{2.27}$$

By solving eqs. 2.26 and 2.27, the equations of n and k are obtained as below

$$n_1 \quad = \quad \sqrt{\frac{\varepsilon' + \sqrt{\varepsilon'^2 + \varepsilon''^2}}{2}} \tag{2.28}$$

$$k_1 \quad = \quad \frac{\varepsilon''}{2\sqrt{\frac{\varepsilon' + \sqrt{\varepsilon'^2 + \varepsilon''^2}}{2}}} \tag{2.29}$$

ε' and ε'' are obtained by substituting eq. 2.26 into 2.25.

$$\varepsilon' \quad = \quad n_0^2 \left(\sin^2 \theta_0 + \frac{\cos^2 \theta_0 \left[(1-R)^2 - 4R\sin^2 \delta \right]}{\left(1 + R - 2\sqrt{R}\cos\delta \right)^2} \right) \tag{2.30}$$

and

$$\varepsilon'' \quad = \quad n_0^2 \left(\frac{\cos^2 \theta_0 \left[4(1-R)\sqrt{R}\sin\delta \right]}{\left(1 + R - 2\sqrt{R}\cos\delta \right)^2} \right) \tag{2.31}$$

2.2 Spectral Resolution

Spectral resolution is a division of chemometrics that concerns about mathematics, statistics and formal logic in chemical data.[2-3] The aim of spectral resolution is to resolve the spectra in order to reveal absorptivities and concentrations of each component that contribute to the observed spectra.

In this work, the method of spectral resolution composes of two aspects:

2.2.1   Principal component analysis and error analysis

2.2.2   Multivariate curve resolution

2.2.1 Principal Component Analysis and Error Analysis

Principal component analysis (PCA) is a tool in chemometrics that decomposes the data matrix into eigenvector space.[3,16] Suppose the data matrix ($\mathbf{D}$) consisting of r rows and c columns as

$$\mathbf{D} = \underset{\text{row designee}}{} \begin{bmatrix} d_{11} & d_{12} & d_{13} & ... & d_{1c} \\ d_{21} & d_{22} & d_{23} & ... & d_{2c} \\ d_{31} & d_{32} & d_{33} & ... & d_{2c} \\ \vdots & \vdots & \vdots & & \vdots \\ d_{r1} & d_{r2} & d_{r3} & ... & d_{rc} \end{bmatrix} \qquad (2.32)$$

column designee

In infrared spectroscopy, the rows and columns of the data matrix are corresponding to the spectral channel (or wavenumber) and the measured solution, respectively. The procedure of PCA was described below.

a) Construct the covariance matrix ($\mathbf{Z}$) by premultiplying the data matrix by its transpose:

$$\mathbf{Z} = \mathbf{D}' \cdot \mathbf{D} \qquad (2.33)$$

b) Make an initial guess of the first eigenvector ($\mathbf{c}_1$) and then multiply to the covariance matrix:

$$\mathbf{Z}\mathbf{c}_1 = \lambda_1 \mathbf{c}_1 \qquad (2.34)$$

where λ_1 is the eigenvalue of the first eigenvector. The product of $\mathbf{Z}\mathbf{c}_1$ is then normalized to obtain the new $\mathbf{c}_1$ and again multiplied to $\mathbf{Z}$ to give a better approximation to $\mathbf{c}_1$ and λ_1. This process is repeated until better approximations of $\mathbf{c}_1$ and λ_1 are obtained.

c) Create the first-residual matrix ($\mathbf{R}_1$):

$$\mathbf{R}_1 = \mathbf{Z} - \lambda_1 \mathbf{c}_1 \mathbf{c}_1' \qquad (2.35)$$

d) Determine the second eigenvector by an iteration procedure analogous to the method used to obtain the first eigenvector:

$$\mathbf{R}_1\mathbf{c}_2 \quad = \quad \lambda_2\mathbf{c}_2 \qquad\qquad (2.36)$$

e) Calculate the second-residual matrix ($\mathbf{R}_2$):

$$\mathbf{R}_2 \quad = \quad \mathbf{R}_1 - \lambda_2\mathbf{c}_2\mathbf{c}_2' \qquad\qquad (2.37)$$

f) Carry out this computation to extract the remaining eigenvectors until the residual is essentially zero or the number of principal factors is equal to the number of columns or rows in the data matrix, whichever is smaller.

The eigenvectors that obtained from PCA are classified into two sets. The first set is called primary eigenvector that belongs to the (true) signal. And the second set is called secondary eigenvector that belongs to the random noise. Hence the number of primary eigenvectors is the number of components that truly contributed to the spectral data. To determine the number of primary eigenvectors, various error indicators are provided.

i) Residual standard deviation (RSD) is defined as[3,17-18]

$$\text{RSD} \quad = \quad \left[\frac{\sum\limits_{j=n+1}^{c} \lambda_j^0}{r(c-n)}\right]^{\frac{1}{2}} \qquad\qquad (2.38)$$

where λ^0 is the eigenvalue associated with the residual error. The criterion of judgement of number of primary eigenvectors is met when the RSD approximately equals to the (estimated) experimental error.

ii) Imbedded error (IE) function is defined as[3,17-18]

$$IE \quad = \quad \left[\frac{n \sum_{j=n+1}^{c} \lambda_j^0}{rc(c-n)} \right]^{\frac{1}{2}} \tag{2.39a}$$

$$= \quad RSD\sqrt{\frac{n}{c}} \tag{2.39b}$$

The IE function should decrease as more and more primary eigenvectors are used, and increase when the second eigenvectors are included.

iii) Malinowski's factor indicator function (IND) is defined as[3,19]

$$IND \quad = \quad \frac{RSD}{(c-n)^2} \tag{2.40}$$

The IND function, similar to the IE function, reaches a minimum when the correct number of primary eigenvectors are employed.

iv) Percent significance level (%SL) for F-distribution is defined as the probability that F would be as large as it is if the first sample's underlying distribution actually has smaller variance that the second's denoted by $Q\left(\frac{F}{f_1}, f_2 \right)$, where f_1 and f_2 are the number of degree of freedom in the first and second samples, respectively.[3,18,20]

$$\%SL \quad = \quad 100 \times Q\left(\frac{F}{f_1}, f_2 \right)$$

$$= \quad 100 \frac{\Gamma(f_1 + f_2)}{\Gamma(f_1)\Gamma(f_2)} \int_0^x F^{(f_1-1)} (1-F)^{(f_2-1)} \, dF \tag{2.41}$$

where $x = \dfrac{f_2}{f_2 + f_1 \cdot \frac{F}{2}}$ and $\Gamma(f)$ is the Gamma function of argument f that defined as

$$\Gamma(f) \quad = \quad \int\limits_{0}^{x} F^{(f-1)} e^{-F} dF \qquad (2.42)$$

The number of primary eigenvectors is determined when the significant level for n eigenvalues is less than some desired value such as 5% or 10%.[18]

When the true number of components (n) is determined, the *reduced* column matrix ($\bar{\mathbf{C}}$), is constructed by:

$$\bar{\mathbf{C}} \quad = \quad \begin{bmatrix} \mathbf{c}'_1 \\ \mathbf{c}'_2 \\ \vdots \\ \mathbf{c}'_n \end{bmatrix} \quad = \quad \begin{bmatrix} \mathbf{c}_1 & \mathbf{c}_2 & \cdots & \mathbf{c}_n \end{bmatrix}' \qquad (2.43)$$

The *reduced* row matrix ($\bar{\mathbf{R}}$) is obtained by premultiplication of the inverse of the $\bar{\mathbf{C}}$ by data matrix as

$$\bar{\mathbf{R}} \quad = \quad \mathbf{D}\bar{\mathbf{C}}^{-1} \quad = \quad \mathbf{D}\bar{\mathbf{C}}' \qquad (2.44)$$

Then multiply $\bar{\mathbf{C}}$ by $\bar{\mathbf{R}}$ to generate the *reproduced* data matrix ($\bar{\mathbf{D}}$) as

$$\bar{\mathbf{D}} \quad = \quad \bar{\mathbf{R}}\bar{\mathbf{C}} \qquad (2.45)$$

At the end of this stage, the factor model is already compressed by deleting the error factors, and obtained the more accurate reproduced data. However, from the standpoint of a theoretical chemist, the analysis should not be terminated here. The next objective is to transform to obtain the absorptivity and concentration matrices from the reproduced data matrix as described in the next section.

2.2.2 Multivariate Curve Resolution

Multivariate curve resolution (MCR) is an effective tool in self-modeling technique of factor analysis.[21-26] The task of MCR is to determine the matrices of absorptivity ($\mathbf{K}$) and concentration ($\mathbf{C}$). Let's begin with the finding of some columns of $\bar{\mathbf{D}}$ (selective variables) where unique contribution of the c different

components. Then $\mathbf{C}$ can be approximately by these columns and pure component spectra can be obtained by a least-squares procedure as

$$\mathbf{K} \quad = \quad \mathbf{C}^{+} \cdot \bar{\mathbf{D}} \tag{2.46}$$

where $\mathbf{C}^{+}$ is the pseudoinverse of $\mathbf{C}$ matrix. Then the new estimation of concentration is obtained by a least-squares procedure as

$$\mathbf{C} \quad = \quad \bar{\mathbf{D}} \cdot \mathbf{K}^{+} \tag{2.47}$$

where $\mathbf{K}^{+}$ is the pseudoinverse of $\mathbf{K}$ matrix. The process is iterative until no any significant differences between successive estimations.

To reduce the ambiguity of transformations in eqs. 2.46 and 2.47, two constraints are applied: (1) non-negativity – all concentration and absorptivity values must be positive, and (2) constant total concentrations – the total concentrations (*i.e.*, volume fraction) of each solution must be equal or normalized.

2.3 Absorptance of Multicomponent Mixtures

When an electromagnetic radiation impinges on the surface of material, there are several components of radiation that can be observed as shown in Figure 2.4. According to the conservation of energy, the following relationship is attained

$$I_{0} \quad = \quad I_{T} + I_{R} + I_{A} \tag{2.48}$$

where I_{0}, I_{T}, I_{R} and I_{A} are intensities of incident radiation, transmitted beam, reflected beam, and absorbed radiation, respectively. When divide the eq. 2.48 with I_{0}, the following equation are obtained.

$$1 \quad = \quad T + R + A \tag{2.49}$$

where T, R and A are called transmittance, reflectance and absorptance, respectively.[6,35]

21
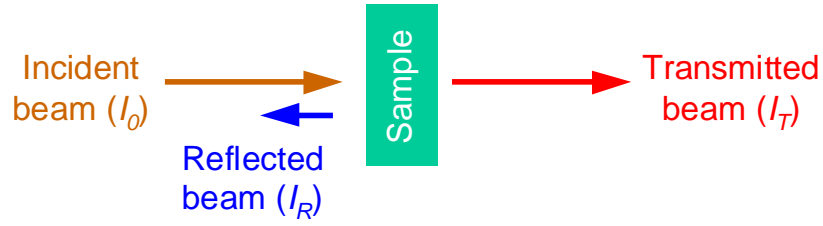
Figure 2.4 Interaction of light with sample.

Under the condition of attenuated total internal reflection, the absorptance of a pure component is well defined as[27]

$$A \quad = \quad 1 - R \quad = \quad \frac{4\pi\nu}{n_0 \cos\theta_0} \int_0^\infty n_1 k_1 \left\langle E_z^2(\theta_0, \nu) \right\rangle_{k=0} dz \qquad (2.50)$$

where $\left\langle E_z^2(\theta_0, \nu) \right\rangle_{k=0}$ is called mean square evanescent field (MSEvF). The decay characteristics of the MSEvF is given in term of the penetration depth (d_p) as

$$\left\langle E_z^2(\theta_0, \nu) \right\rangle_{k=0} \quad = \quad \left\langle E_{z=0}^2(\theta_0, \nu) \right\rangle_{k=0} \exp\left(-\frac{2z}{d_p}\right) \qquad (2.51)$$

and
$$d_p \quad = \quad \frac{1}{2\pi\nu n_0 \left[\sin^2\theta_0 - \left(\dfrac{n_1}{n_0}\right)^2\right]^{1/2}} \qquad (2.52)$$

where $\left\langle E_{z=0}^2(\theta_0, \nu) \right\rangle_{k=0}$ is the MSEvF at the interface ($z = 0$). For s- and p-polarizations, the $\left\langle E_{z=0}^2(\theta_0, \nu) \right\rangle_{k=0}$ are given as[28]

$$\left\langle E_{s,z=0}^2(\theta_0, \nu) \right\rangle_{k=0} \quad = \quad \frac{4\cos^2\theta_0}{1 - \left(\dfrac{n_1}{n_0}\right)^2} \qquad (2.53)$$

and $\quad \left\langle E_{p,z=0}^2(\theta_0, \nu) \right\rangle_{k=0} \quad = \quad \dfrac{4\cos^2\theta_0 \left[\sin^2\theta_0 - \left(\dfrac{n_1}{n_0}\right)^2\right] + 4\cos^2\theta_0 \sin^2\theta_0}{\left[1 - \left(\dfrac{n_1}{n_0}\right)^2\right]\left\{\left[1 + \left(\dfrac{n_1}{n_0}\right)^2\right]\sin^2\theta_0 - \left(\dfrac{n_1}{n_0}\right)^2\right\}} \qquad (2.54)$

Hence the expression for the absorptance of multicomponent mixtures is assumed to be the same as that of pure component by replacing $n_1 k_1$ by $n_{mix} k_{mix}$ as

$$A_{mix} = \frac{4\pi\nu}{n_0 \cos\theta_0} \int_0^\infty n_{mix} k_{mix} \left\langle E_z^2(\theta_0, \nu) \right\rangle_{k=0} dz \qquad (2.55)$$

where n_{mix} and k_{mix} are the refractive and absorption indices of mixtures. In addition, d_p and MSEvF for s- and p-polarizations of the mixture are assumed to be the same as that of the pure component except for the term n_{mix}.

$$d_{p,mix} = \frac{1}{2\pi\nu n_0 \left[\sin^2\theta_0 - \left(\dfrac{n_{mix}}{n_0}\right)^2 \right]^{1/2}} \qquad (2.56)$$

$$\left\langle E_{s,z=0}^2(\theta_0,\nu) \right\rangle_{k=0,mix} = \frac{4\cos^2\theta_0}{1 - \left(\dfrac{n_{mix}}{n_0}\right)^2} \qquad (2.57)$$

and $\left\langle E_{p,z=0}^2(\theta_0,\nu) \right\rangle_{k=0,mix} = \dfrac{4\cos^2\theta_0 \left[\sin^2\theta_0 - \left(\dfrac{n_{mix}}{n_0}\right)^2 \right] + 4\cos^2\theta_0 \sin^2\theta_0}{\left[1 - \left(\dfrac{n_{mix}}{n_0}\right)^2 \right] \left\{ \left[1 + \left(\dfrac{n_{mix}}{n_0}\right)^2 \right] \sin^2\theta_0 - \left(\dfrac{n_{mix}}{n_0}\right)^2 \right\}}$ (2.58)

Since the complex dielectric constant of mixture ($\hat{\varepsilon}_{mix}$) is defined as[29]

$$\hat{\varepsilon}_{mix} = \sum_{j=1}^p \phi_j \hat{\varepsilon}_j \qquad (2.59)$$

where ϕ_j and $\hat{\varepsilon}_j$ are the volume fraction and complex dielectric constant of the jth component, respectively, and p is the number of components in mixture.

Analogous to the complex dielectric constant of pure component as formulated in Section 2.1.4, the complex dielectric constant of mixture can be rewritten as

$$\hat{\varepsilon}_{mix} \quad = \quad \left(\hat{n}_{mix}\right)^2 \quad = \quad n_{mix}^2 - k_{mix}^2 + 2n_{mix}k_{mix}i \tag{2.60}$$

$$= \quad \sum_{j=1}^{p}\phi_j\left(n_j^2 - k_j^2 + 2n_j k_j i\right)$$

$$= \quad \sum_{j=1}^{p}\phi_j\left(n_j^2 - k_j^2\right) + i\sum_{j=1}^{p}2\phi_j n_j k_j \tag{2.61}$$

Evidently, the imaginary part of eq. 2.60 can be rewritten as

$$n_{mix}k_{mix} \quad = \quad \sum_{j=1}^{p}\phi_j n_j k_j \tag{2.62}$$

Substitute eqs. 2.56, 2.57 and 2.62 into eq. 2.55 and obtain

$$A_{mix} \quad = \quad \frac{4\pi\nu}{n_0\cos\theta_0}\cdot\frac{4\cos^2\theta_0}{1-\left(\dfrac{n_{mix}}{n_0}\right)^2}\cdot\frac{1}{2\pi\nu n_0\left[\sin^2\theta_0-\left(\dfrac{n_{mix}}{n_0}\right)^2\right]^{1/2}}\cdot\sum_{j=1}^{p}\phi_j n_j k_j$$

$$= \quad \frac{8\cos\theta_0}{n_0^2\left[1-\left(\dfrac{n_{mix}}{n_0}\right)^2\right]\left[\sin^2\theta_0-\left(\dfrac{n_{mix}}{n_0}\right)^2\right]^{1/2}}\cdot\left(\sum_{j=1}^{p}\phi_j n_j k_j\right) \tag{2.63}$$

Let's defined a new variable called absorptance coefficient (κ) as

$$\kappa_j \quad = \quad \frac{8\cos\theta_0}{n_0^2\left[1-\left(\dfrac{n_{mix}}{n_0}\right)^2\right]\left[\sin^2\theta_0-\left(\dfrac{n_{mix}}{n_0}\right)^2\right]^{1/2}}\cdot\left(n_j k_j\right) \tag{2.64}$$

Therefore, substitute eq. 2.64 into 2.63 and obtain

$$A_{mix} \quad = \quad \sum_{j=1}^{p}\kappa_j\phi_j \tag{2.65}$$

Arrive here, the goal of this section is met. There exist a linear relationship between absorptance and volume fraction of each component in mixtures. Moreover,

if the density (ρ) and molecular weight (MW) of each component are known, the concentration (c) of each component can be written as:

$$\phi_j = \frac{V_j}{V_{mix}} = \frac{MW_j}{\rho_j} c_j \qquad (2.66)$$

However, the linear relationship between absorptance and volume fraction is valid under the following assumptions:

a) The variation of n_{mix} is small. In fact, the refractive indices of most organic compounds are in the same range (*i.e.*, about 1.5). Therefore, the differences in n_{mix} is insignificant and thus, the linear relationship would be valid for most organic compounds.

b) The deviation from ideality of the multicomponent solution is small. Reports on this deviation are very limited, the closest example would be the deviation of ethanol/water solution which is about 5%.[36] However, the ideal or diluted solutions would be suggested for usage.

CHAPTER III

PROGRAM IMPLEMENTATION

The program `WizardIR` version 1.0 was developed in the environment of MATLAB v6.5 (MathWorks, Inc).[30] The main application is to resolve the absorptance spectra of multicomponent mixtures in order to reveal the profiles of volume fractions and optical constants. However, the program can also be further adapted to resolve other applications. The program manual and example were shown in Appendix.

The program `WizardIR` contains fourteen files which showed in Table 3.1. All subprograms were newly implemented except for the `Mpure.m` and `nnls.m` subprograms were modified from the original codes of Professor Dr. Roma Tauler and MathWorks, Inc.

It should be noted that the subprograms `MPFA.m`, `MErr.m` and `MFindPrimary.m` were invoked from previous research work, however, the detailed explanations of these subprograms were described in the literature.[31]

The program was separated into four parts:

    3.1 Main program
    3.2 Spectral resolution
    3.3 Optical constants determination
    3.4 Summary of the requirements for input and default values

3.1 Main Program

The main program was designed for user to input the spectra filename included elementary data, and to select the appropriate methodologies, which are:

- Spectra filename
- Range of monitoring time

- Selection of automatic or manual setting for initial guess of concentrations for MMCR subprogram
- Convergence in the procedure of MMCR subprogram
- Experimental setups: refractive index of incident media, angle of incidence and polarization of the light
- Convergence in the procedure of MRdel2nk subprogram
- Option for saving the results of prediction

The sequence of input was shown in Figure 3.1. The main program also controlled the program flows. In addition, the main program was invented to check the inputs and prevented the user's illegal operation.

Table 3.1 List of all files of the program WizardIR version 1.0.

File	Function
WizardIR.m	Main program.
MKKT.m	Subprogram for calculating the Kramers-Kronig transformation of *n* and *k*.
MsimRdel.m	Subprogram for calculating the Fresnel equation.
MR2del.m	Subprogram for calculating Kramers-Kronig transformation from reflectance to phase shift.
MRdel2nk.m	Subprogram for determination of *n* and *k* from reflectance and phase shift.
MMCR.m	Subprogram for performing the multivariate curve resolution.
Mpure.m	Subprogram for providing the initial guess for the MMCR.m subprogram.
MPFA.m	Subprogram for performing the principal factor analysis (PFA), *i.e.* synonym with the principal component analysis (PCA).
MErr.m	Subprogram for performing the error analysis.
MFindPrimary.m	Subprogram for determining the plausible number of primary eigenvectors.

Table 3.1 (Cont.)

File	Function
Mrms.m	Subprogram for calculating the root-mean-square error.
Mspecificwn.m	Subprogram for setting the spectral analysis range.
nnls.m	Subprogram for performing the non-negative least squares.
Mpof.m	Subprogram for setting the positions of figures.

3.2 Spectral Resolution

The part of spectral resolution was designed to perform the principal component analysis, error analysis and multivariate curve resolution. First, the spectra matrix was decomposed via the subprogram MPFA into the eigenvector space by principal component analysis as described in Section 2.2.1. The error indicators such as eigenvalue, RSD, IE, IND, and %SL were calculated via the subprogram MErr and used to determine the more possible number of primary eigenvectors via the subprogram MFindPrimary. When the correct number of components was identified, the more accurate, reproduced data were computed. The program would continue to execute the multivariate curve resolution via the subprogram MMCR to extract the profiles of volume fractions and absorptance coefficients of each component that contributed to the spectra as described in Section 2.2.2 and 2.3. The procedure of this part was listed in Figure 3.2. The algorithm of MMCR was illustrated in Figure 3.3.
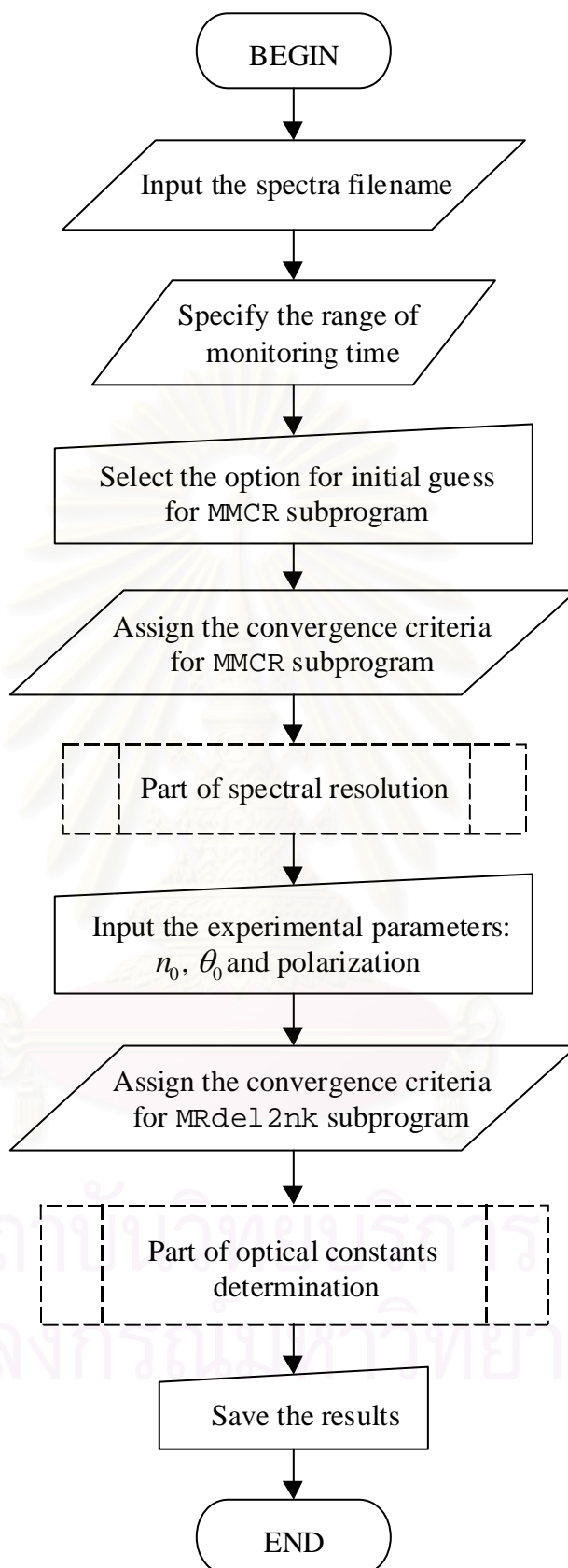
Figure 3.1 Flowchart of the main program of `WizardIR` version 1.0.
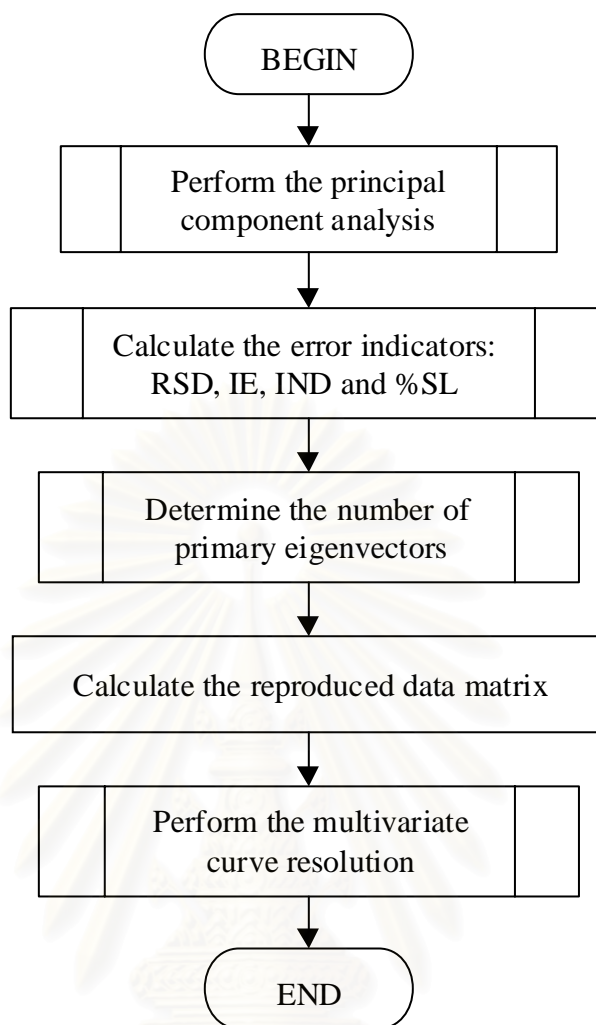
Figure 3.2 Flowchart of the part of spectral resolution.
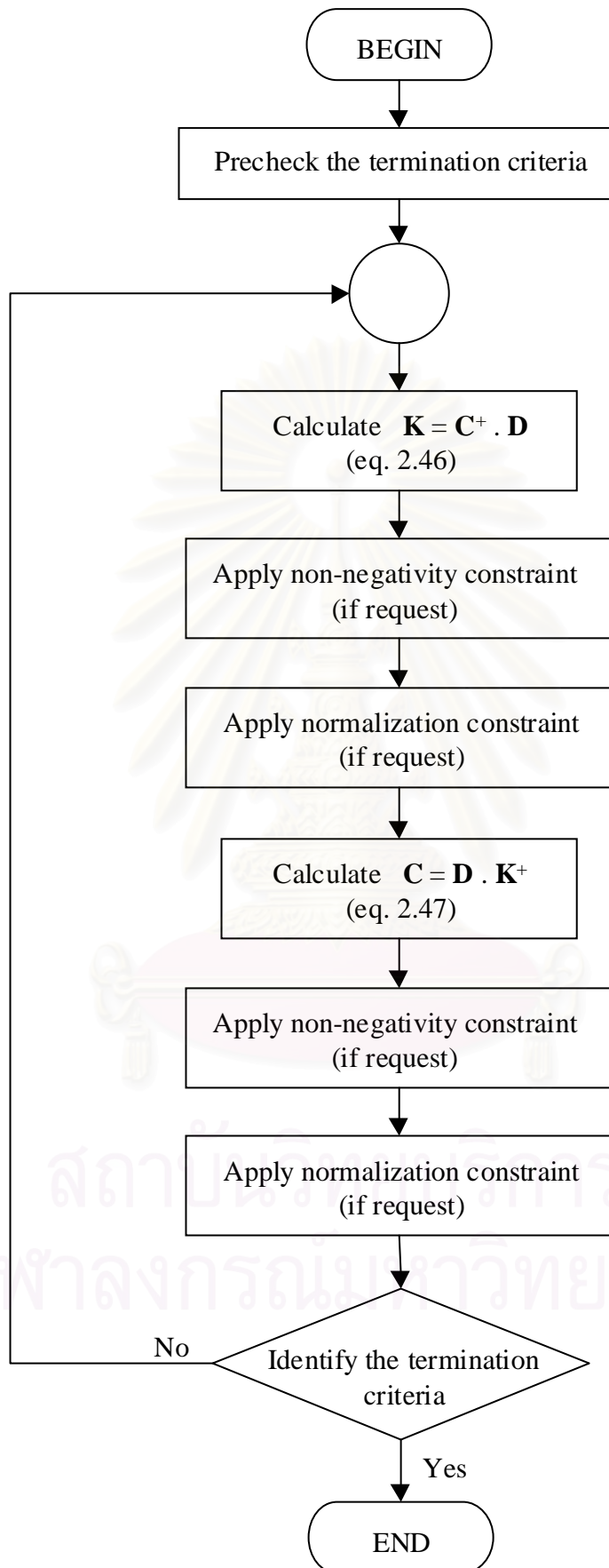
Figure 3.3 Flowchart of the subprogram MMCR.

3.3 Optical Constants Determination

The subprogram for optical constants determination was designed to calculate the n and k from reflectance R and phase shift δ. The estimated absorptance coefficient of each component was calculated in term of R. The δ was generated from R via the subprogram MR2del by Kramers-Kronig transformation as described in Section 2.1.3. The R and δ were used as inputs for the subprogram MRdel2nk to calculate the n and k profiles of each component as described in Section 2.1.4. The procedure of this part and the algorithm of MRdel2nk subprogram were shown in Figure 3.4.

3.4 Summary of Input Requirements and Default Values

The followings are input requirements and default values.

i) Prepare the spectra as a *.txt file with ASCII format.

ii) Specify the range of monitoring time.

iii) Select an option for setting the automatic or manual for initial guess for MMCR subprogram. The automatic option is recommended for general purposes.

iv) Set convergence criteria for MMCR subprogram. The default values are: maximum cycle = 100 and tolerance = 1×10^{-8}

v) Input the experimental parameters: refractive index of incident media, angle of incidence (in the unit of degree) and polarization of the light. The default polarization is *s*-polarization.

vi) Set the convergence criteria for MRdel2nk subprogram. The default values are: maximum cycle = 20 and tolerance = 1×10^{-8}

vii) Select an option for saving the results.
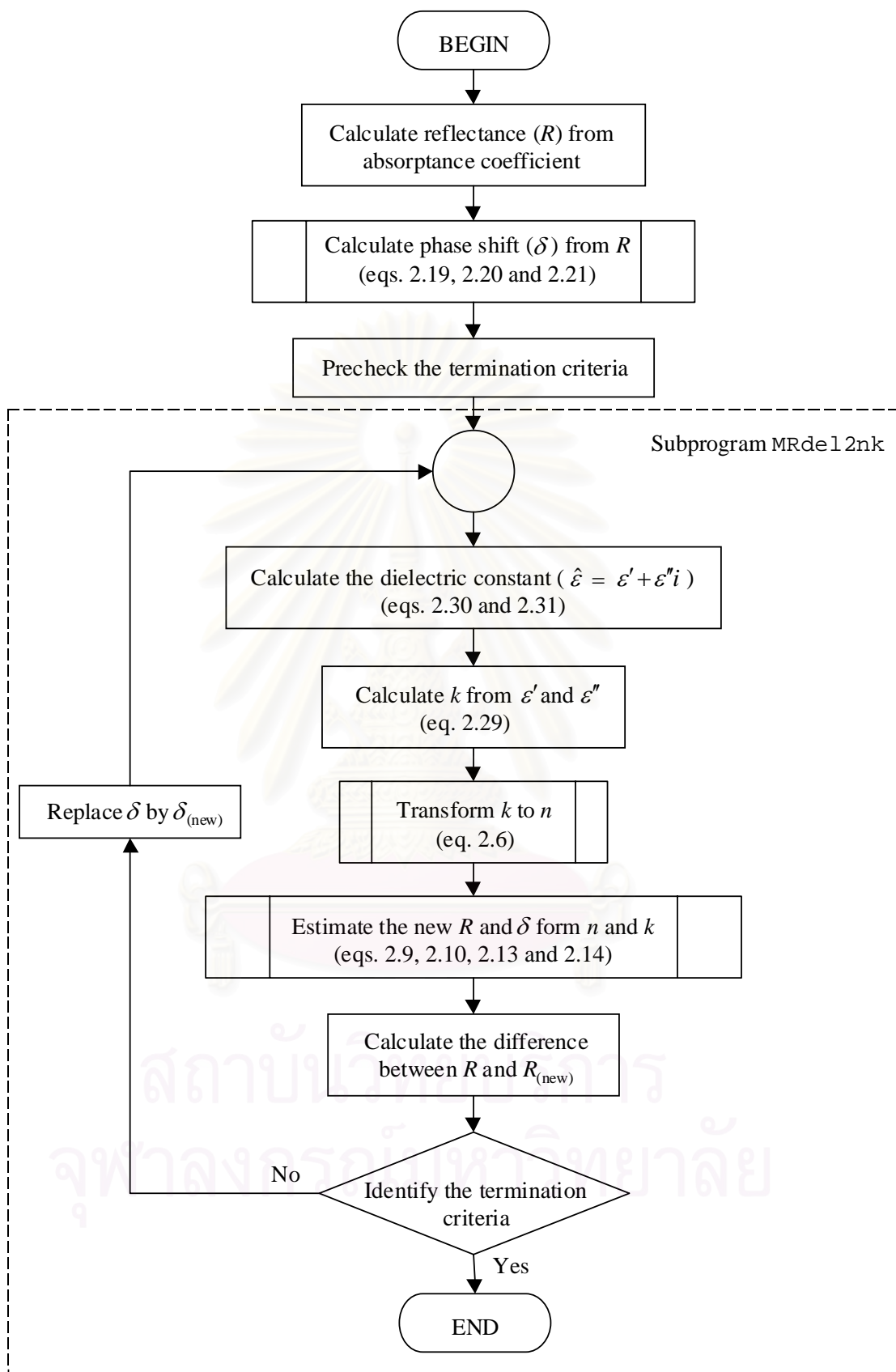
Figure 3.4   Flowchart of the subprograms of optical constants determination
and the subprogram `MRdel2nk` (in dash frame).

CHAPTER IV

VALIDATION OF PROGRAM

The program validation is an important part of the program development. The purposes of the validation are to test the validity of the program and to determine the accuracy and efficiency of the program under defined situations. There are (at least) 2 ways for the program validation. The first one is to test with simulated system that all parameters or measured properties are preset and known. Along this way, the presetting properties are first assumed to be unknown , then the program is applied to determine the desired properties. This test is sometimes called 'blind test'.[16] The second one is to test the program with known experiments, and then the results are compared with literatures or references. For both ways, when the results correspond to the presetting and/or references under the acceptable range of error, the program is validated.

In this chapter, the first way was selected to validate the program WizardIR. The second technique will be shown in Chapters 5 and 6. The simulated spectral data were created to examine the program which includes the important subprograms used to perform Kramers-Kronig transformations and multivariate curve resolution.

4.1 Validation Approach

According to the program, there are two facets to be examined:
  (I) Validation of the subprograms
  (II) Validation of the whole program

The first facet involves the calculations of matrix algebra, Kramers-Kronig transformations, Fresnel equation, and multivariate curve resolution. Calculations and sensible logic of all subprograms were verified and tested individually and/or in group.

The second facet is validated with the simulated system of three volatile components with different rates of evaporation.

In the context of testing, the error was expressed in terms of the following indicators:

$$\text{Norm of error} \quad = \quad \sqrt{\sum_{i=1}^{r}\sum_{j=1}^{c}\left(d_{ij} - \hat{d}_{ij}\right)^2} \tag{4.1}$$

$$\text{Root-mean-square (rms) error} \quad = \quad \sqrt{\frac{\sum_{i=1}^{r}\sum_{j=1}^{c}\left(d_{ij} - \hat{d}_{ij}\right)^2}{r \times c}} \tag{4.2}$$

$$\text{Normalized root-mean-square (nrms) error} \quad = \quad 100 \times \sqrt{\sum_{i=1}^{r}\sum_{j=1}^{c}\left(\frac{d_{ij} - \hat{d}_{ij}}{d_{ij}}\right)^2} \tag{4.3}$$

where d_{ij} and $\hat{d}_{ij}$ are the respective presetting and estimated data. The r and c are the numbers of row and column of data matrix, respectively.

These indicators are slightly different. Norm of error expresses the whole error of data. The rms error expresses the average error of each datum, while the nrms error, on the other hand, expresses the percentage of relative rms error.

4.2 Validation of the Subprograms

As stated in Chapter 3, the program WizardIR composes of 5 important subprograms

        4.2.1   MKKT subprogram

        4.2.2   MsimRdel subprogram

        4.2.3   MR2del and MRdel2nk subprograms

        4.2.4   MMCR subprogram

4.2.1 **MKKT** Subprogram

The subprogram MKKT was created to perform the Kramers-Kronig transformation of *n* and *k* by Maclaurin's formula as described in Section 2.1.1. To verify the subprogram, two sets of simulated spectra were generated by antisymmetric linear combination of Lorentzian functions.[6,32] Spectral Set A consists of two absorption bands with well-defined peak separation. Spectral Set B, on the other hand, is a near-real spectrum. It consists of seven absorption bands with different degree of peak overlapping. The simulated spectra were shown in Figures 4.1 and 4.2.

The subprogram MKKT was tested by transforming from *n* to *k* and *k* to *n* for both spectra sets. The graphical results were shown in Figures 4.3-4.6 and the numerical results were shown in Table 4.1. The transformation results were also compared with the originally simulated data by numerical integration along trapezoidal rule.

From Table 4.1, The nrms error of the calculation of Maclaurin's formula was less than that of trapezoidal rule, *i.e.*, one order of magnitude. It can be concluded that the Kramers-Kronig transformation by Maclaurin's formula (also for MKKT) is more accurate than trapezoidal approach. As a result, the estimated spectra agree very well with the preset values for both transformations from *n* to *k* and *k* to *n*. In addition, the transformation from *k* to *n* is more accurate than that from *n* to *k*.

4.2.2 **MsimRdel** Subprogram

The subprogram MsimRdel was created to calculate the reflectance (R) and phase shift (δ) for *s*- and *p*-polarizations via Fresnel equation as described in Section 2.1.2. Due to the near-reality of spectral Set B in Section 4.2.1, the *n* and *k* spectra were invoked to test the subprogram. For a set of presetting of *n*, *k*, refractive index of incident media (n_0), and angle of incidence (θ_0), the reflectance and phase shift from three modes of reflections: external, internal and total internal reflections were calculated by eqs. 2.9 and 2.10, and shown in Figure 4.7-4.9.
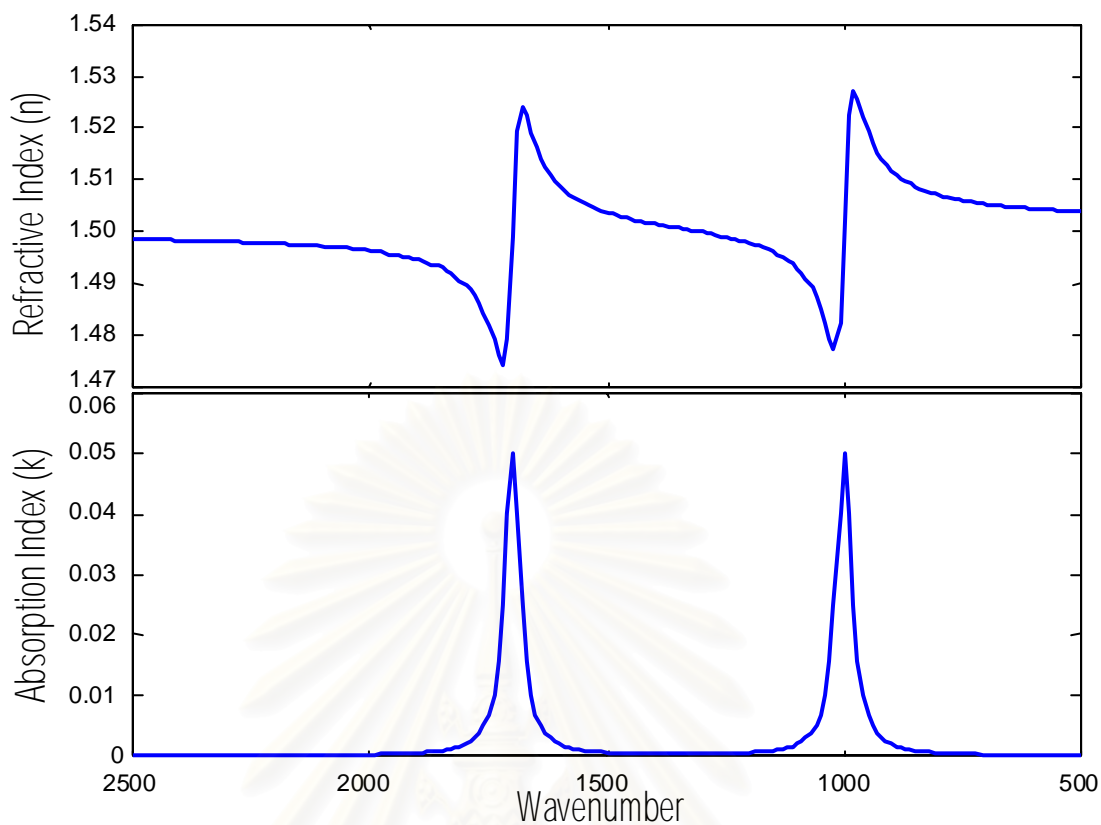
Figure 4.1 Simulated refractive index and absorption index spectra (Set A) in
the mid-infrared region.
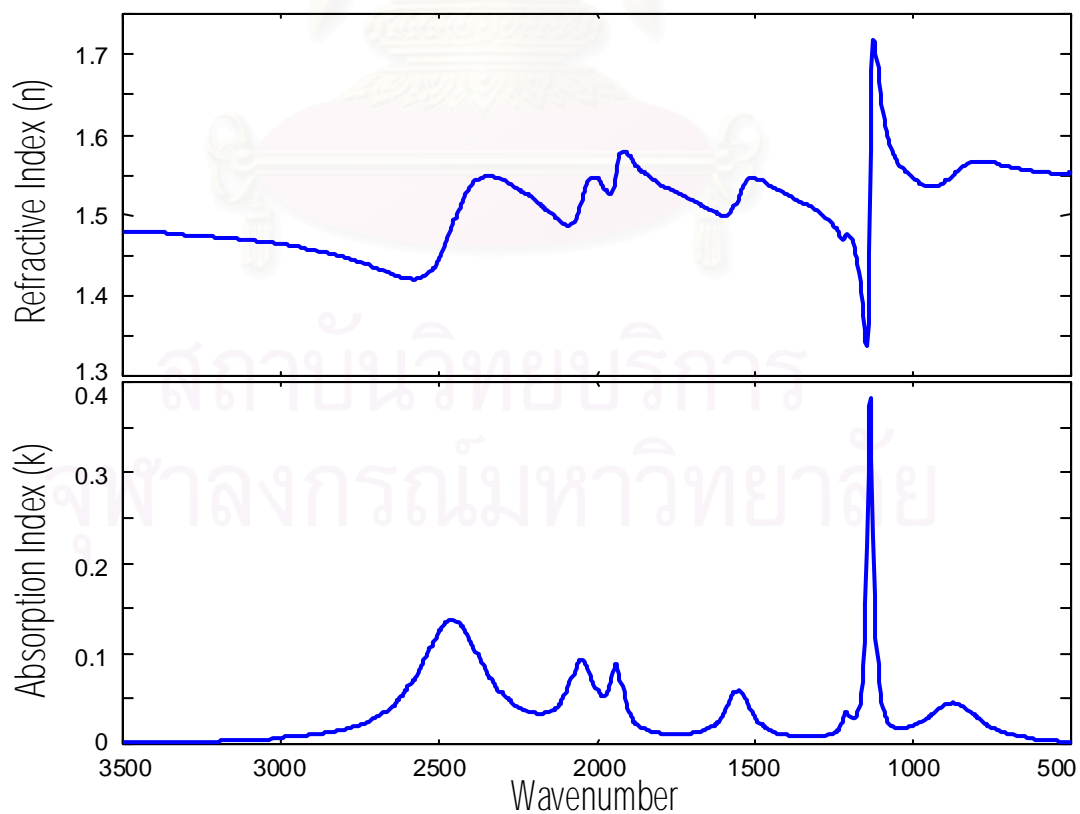
Figure 4.2 Simulated refractive index and absorption index spectra (Set B) in
the mid-infrared region.
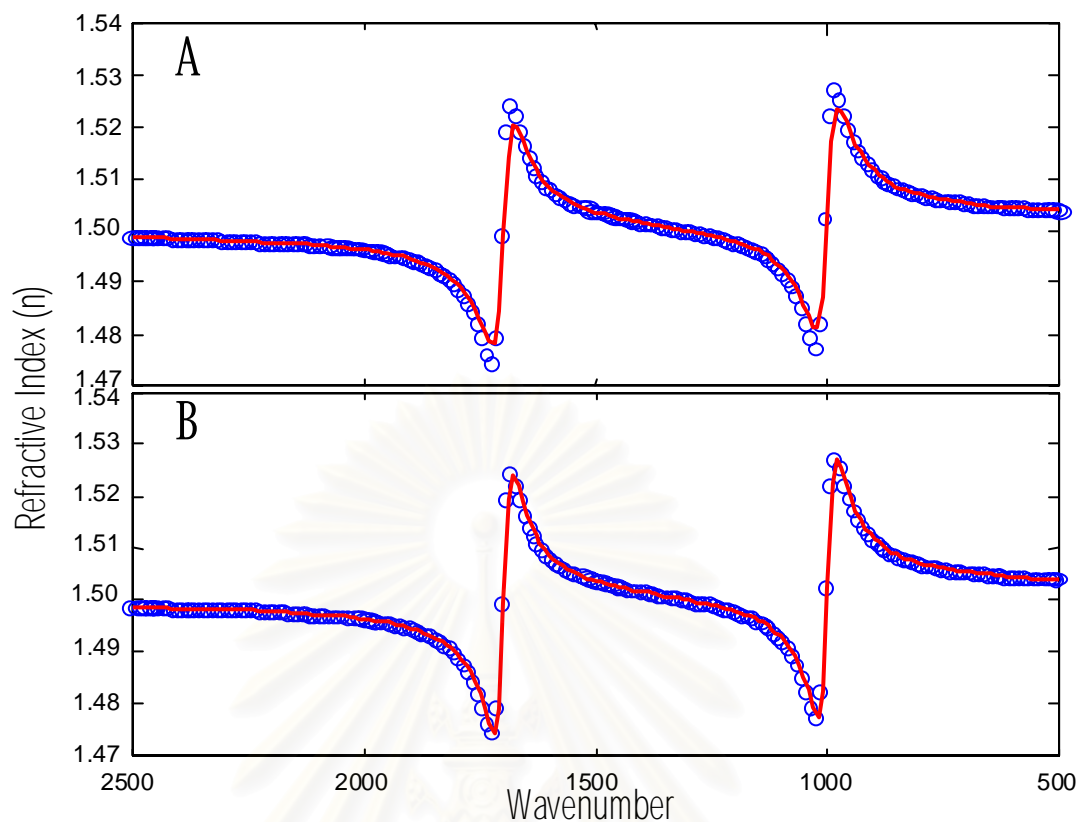
Figure 4.3 Comparison of transformations from *k* to *n* by trapezoidal rule (A) and Maclaurin's formula (B): calculation (solid lines), and presetting (open circles).
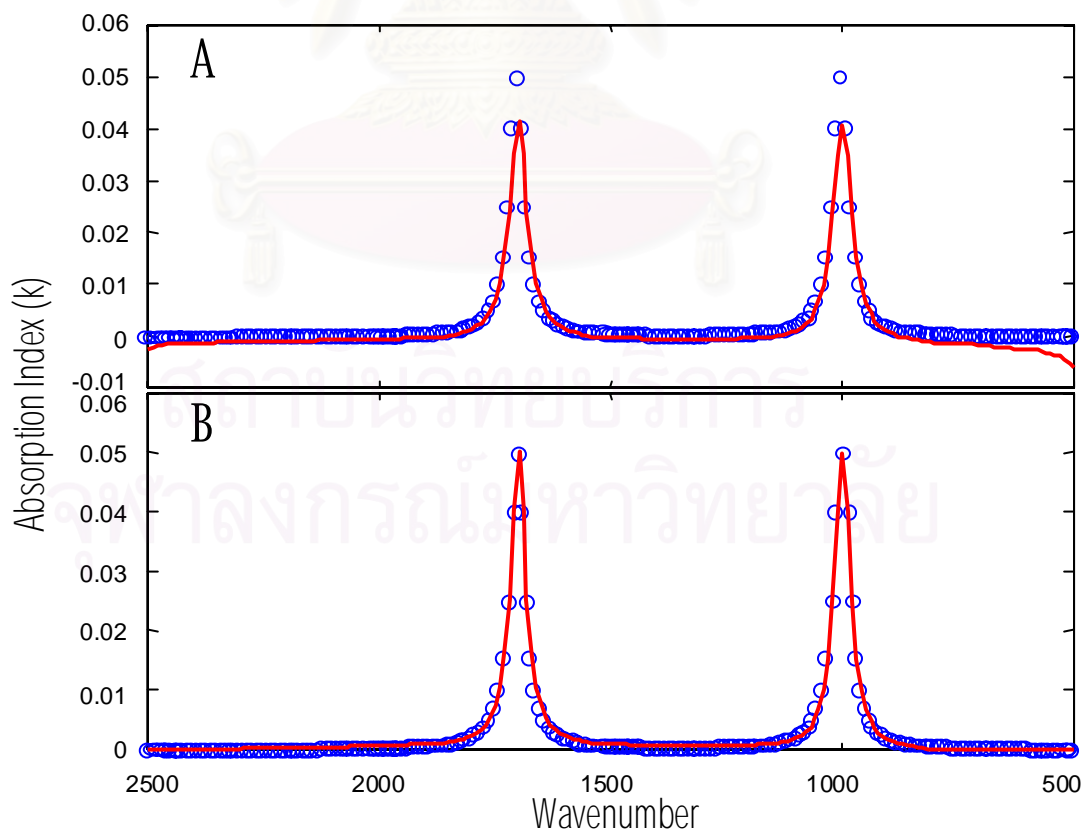
Figure 4.4 Comparison of transformations from *n* to *k* by trapezoidal rule (A) and Maclaurin's formula (B): calculation (solid lines), and presetting (open circles).
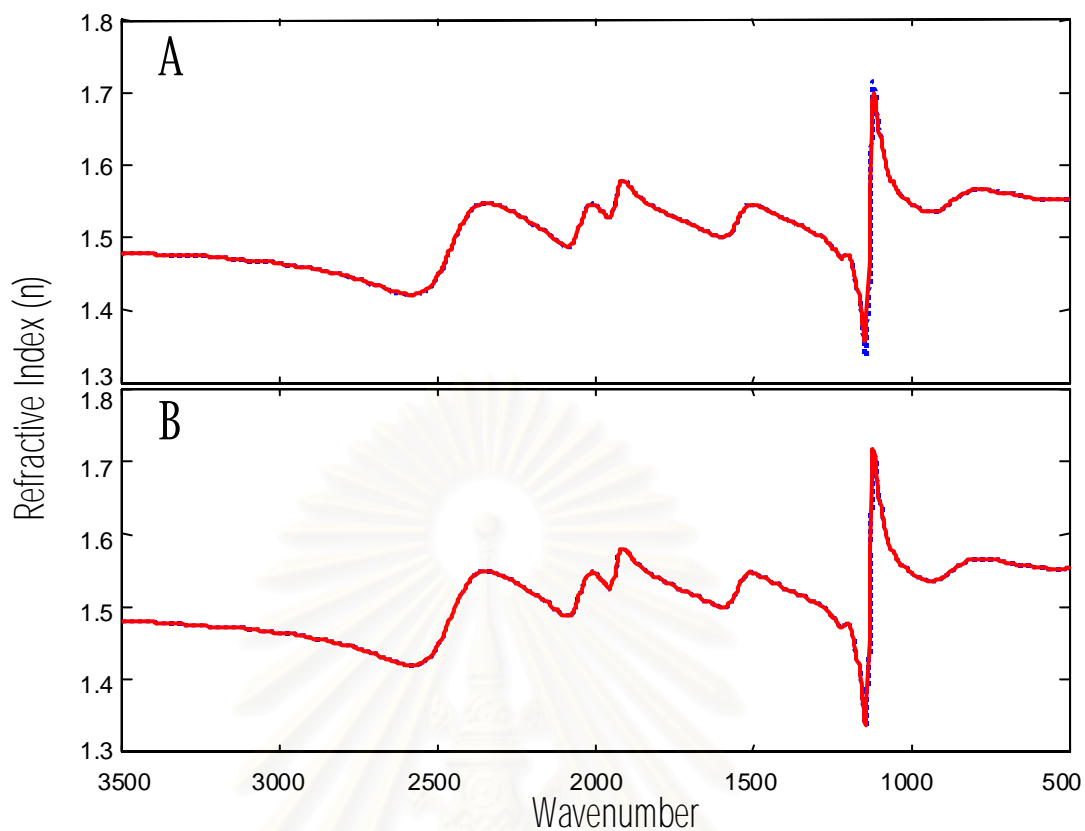
Figure 4.5 Comparison of transformations from *k* to *n* by trapezoidal rule (A) and Maclaurin's formula (B): calculation (solid lines), and presetting (dotted lines).
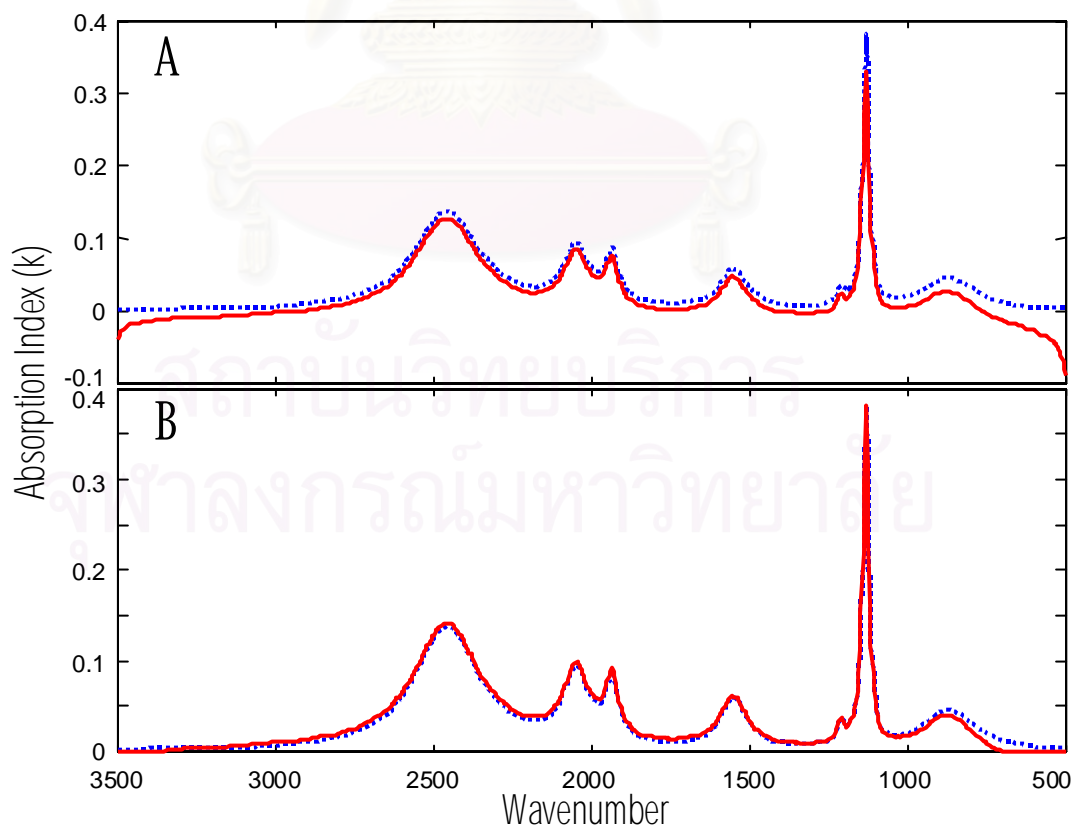
Figure 4.6 Comparison of transformations from *n* to *k* by trapezoidal rule (A) and Maclaurin's formula (B): calculation (solid lines), and presetting (dotted lines).

Table 4.1 Testing results of Kramers-Kronig transformation of *n* and *k*.

Simulated Spectra	Trapezoidal Rule			Maclaurin's Formula		
	Norm	rms	nrms	Norm	rms	nrms
Set A: *k* to *n*	0.0141	9.923×10^{-4}	0.1	0.0005	3.501×10^{-5}	0.002
n to *k*	0.0261	1.839×10^{-3}	20.8	0.0029	2.097×10^{-4}	2.37
Set B: *k* to *n*	0.0652	2.379×10^{-3}	0.2	0.0039	3.278×10^{-5}	0.04
n to *k*	0.4538	1.656×10^{-2}	31.0	0.1073	3.915×10^{-3}	7.33
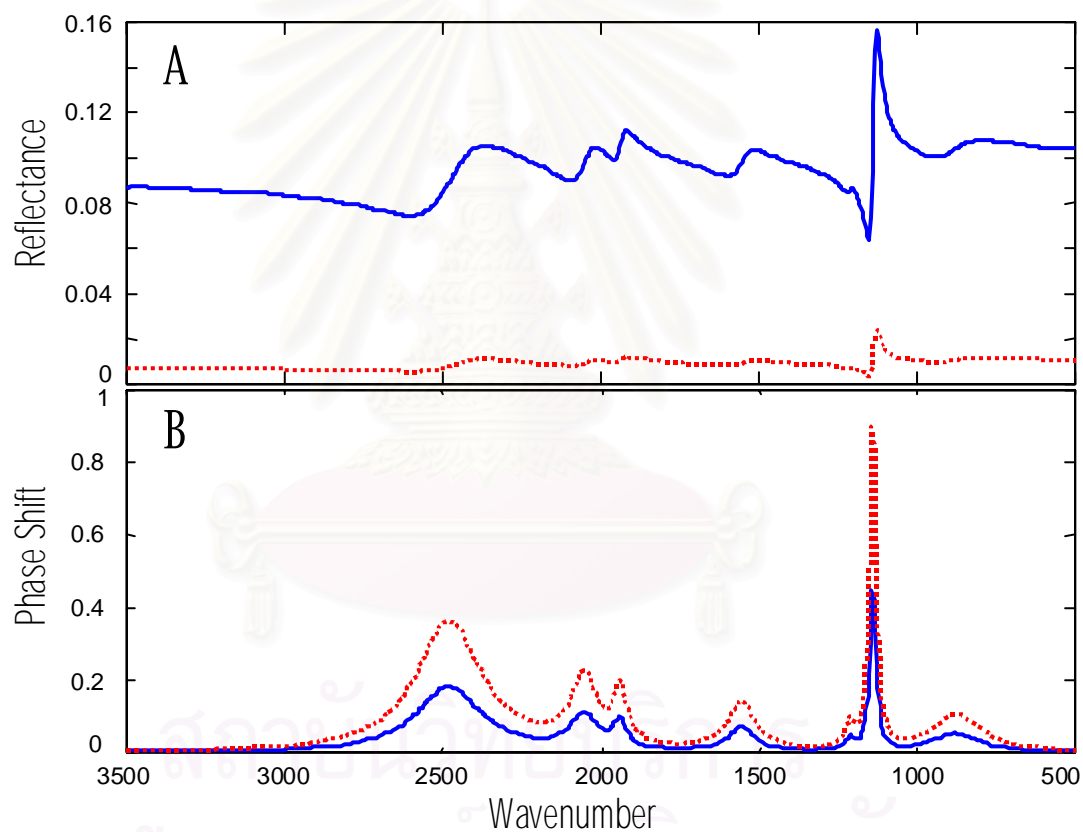
Figure 4.7 Reflectance (A) and phase shift (B) under the external reflection ($n_0 = 1$ and $\theta_0 = 45$): *s*-polarization (solid lines), and *p*-polarization (dotted lines).
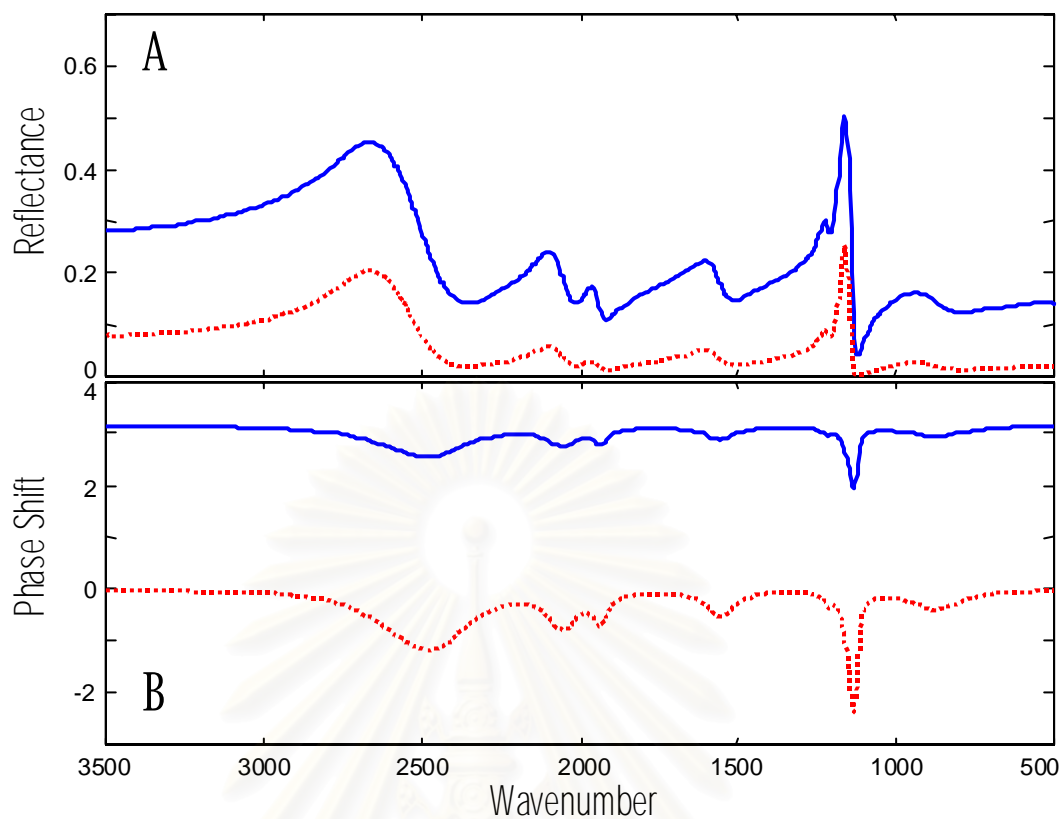
Figure 4.8 Reflectance (A) and phase shift (B) under the internal reflection ($n_0 = 2$ and $\theta_0 = 45$): *s*-polarization (solid lines), and *p*-polarization (dotted lines).
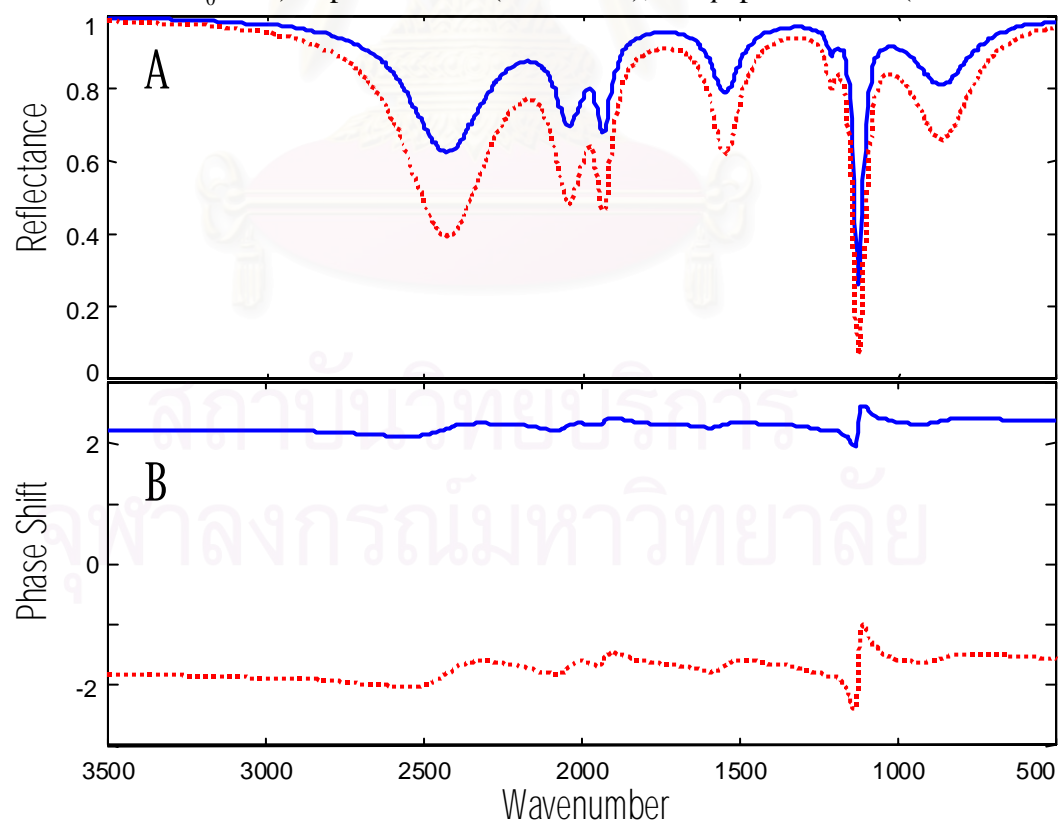
Figure 4.9 Reflectance (A) and phase shift (B) under the total internal reflection ($n_0 = 2.4$ and $\theta_0 = 45$): *s*-polarization (solid lines), and *p*-polarization (dotted lines).

As seen in Figures 4.7 (A), 4.8 (A) and 4.9 (A), the calculated reflectance spectra were differential-type spectra for the cases of external and internal reflections while the absorption-type spectra were observed for the case of total internal reflection. The obtained results were in good agreement with those reported in literatures.[11-12] In addition, the simulation also showed the special phenomena that when $\theta_0 = 45°$, the calculated reflectance in p-polarization equals to the square of reflectance in s-polarization for all reflection modes.[5]

4.2.3 `MR2del` and `MRdel2nk` Subprograms

The subprogram `MR2del` was created to transform reflectance to phase shift by Kramers-Kronig transformation as described in Section 2.1.3. To verify the subprogram, the reflectance and phase shift in Section 4.2.2 were used for presetting, and then the reflectance was transformed to obtain the estimated phase shift. The error of prediction from `MR2del` subprogram was reported in Table 4.2. Comparisons of estimated and presetting phase shifts were shown in Figure 4.10.

From the Table 4.2 and Figure 4.10, it can be concluded that the `MR2del` subprogram worked well for transformation for all reflection modes. However, the error in the mode of external reflection (18.8%) is higher than internal (1.6%) and total internal (1.3%) reflections, respectively. The error of transformation is not important for this situation because the estimated phase shift would be refined again in the process of `MRdel2nk` subprogram.

Table 4.2 Testing results of `MR2del` subprogram.

Reflection Mode	Error of Prediction of Phase Shift		
	Norm	rms	nrms
Internal Reflection	1.3212	0.0482	1.6
Total Internal Reflection	0.8336	0.0304	1.3
External Reflection	0.3432	0.0125	18.8
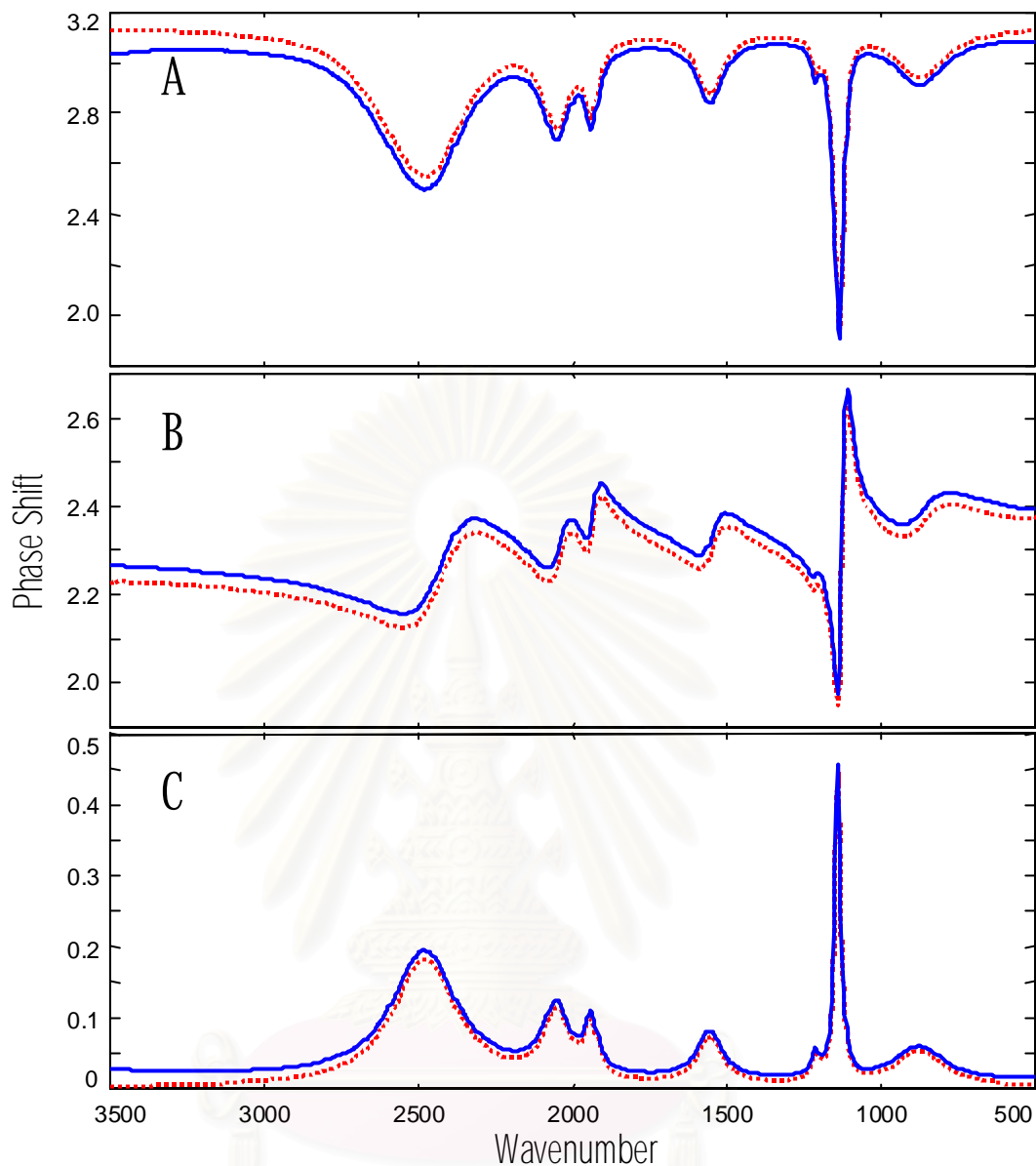
Figure 4.10   Comparison of estimated (solid lines) and presetting (dotted lines) phase shifts: internal (A), total internal (B), and external (C) reflections.

The subprogram MRdel2nk was implemented for determining the n and k from reflectance and phase shift. The algorithm of MRdel2nk was described in Section 2.1.4. To verify the subprogram, the reflectances in Section 4.2.2 were applied to the preset values, and input to the subprogram. The estimated n and k were compared to the true values in Figure 4.2. The numerical results are shown in Table 4.3 and Figures 4.11-4.13.

Table 4.3 Testing results of `MRdel2nk` subprogram.

Reflection Mode	Error of n Prediction			Error of k Prediction		
	Norm	rms	nrms	Norm	rms	nrms
External Reflection	0.1417	5.170×10^{-3}	0.3	0.2157	7.869×10^{-3}	14.7
Internal Reflection	0.0819	2.989×10^{-3}	0.2	0.1047	3.819×10^{-3}	7.2
Total Internal Reflection	0.0022	7.886×10^{-5}	0.005	0.0022	7.886×10^{-5}	0.1
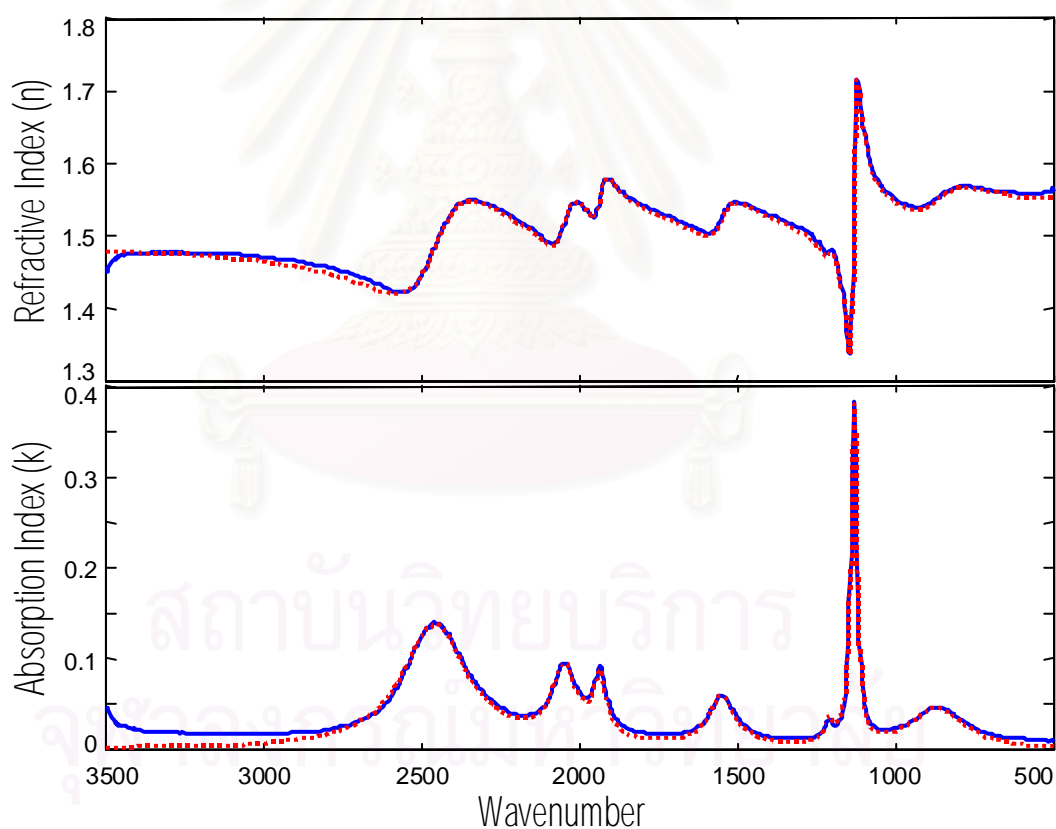
Figure 4.11 Comparison of estimated and presetting of n and k under the situation of external reflection: calculation (solid lines), and presetting (dotted lines).
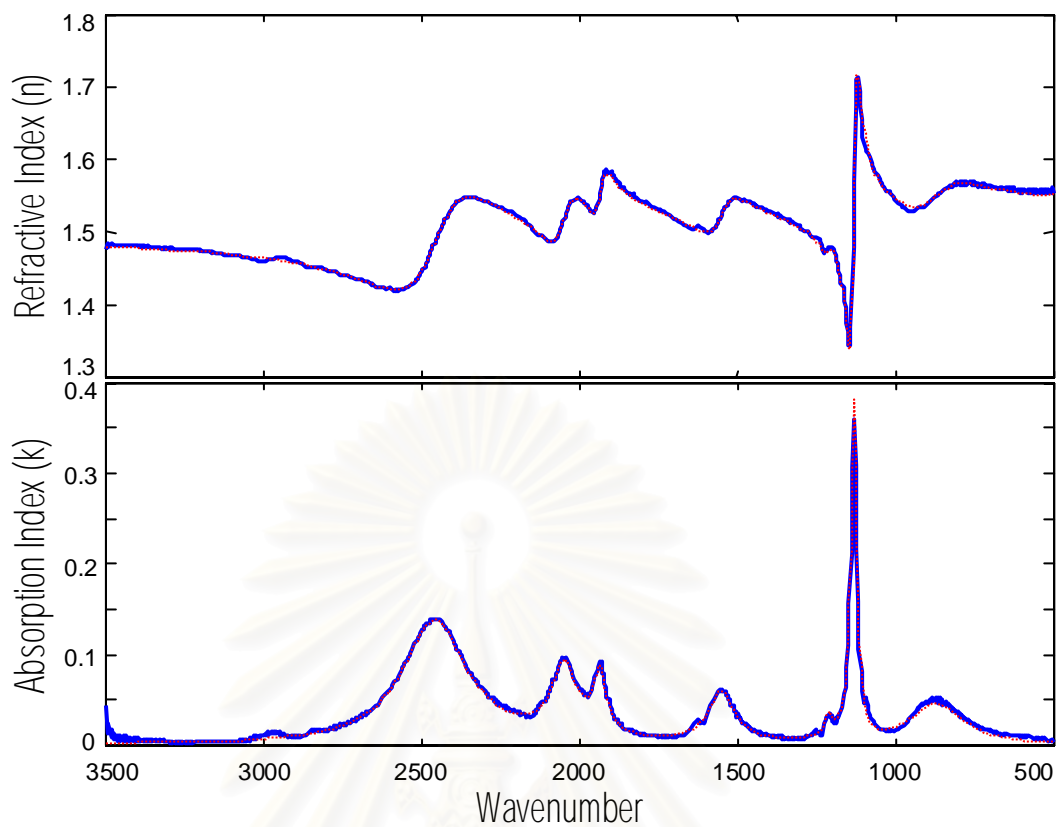
Figure 4.12 Comparison of estimated and presetting of *n* and *k* under the situation of internal reflection: calculation (solid lines), and presetting (dotted lines).
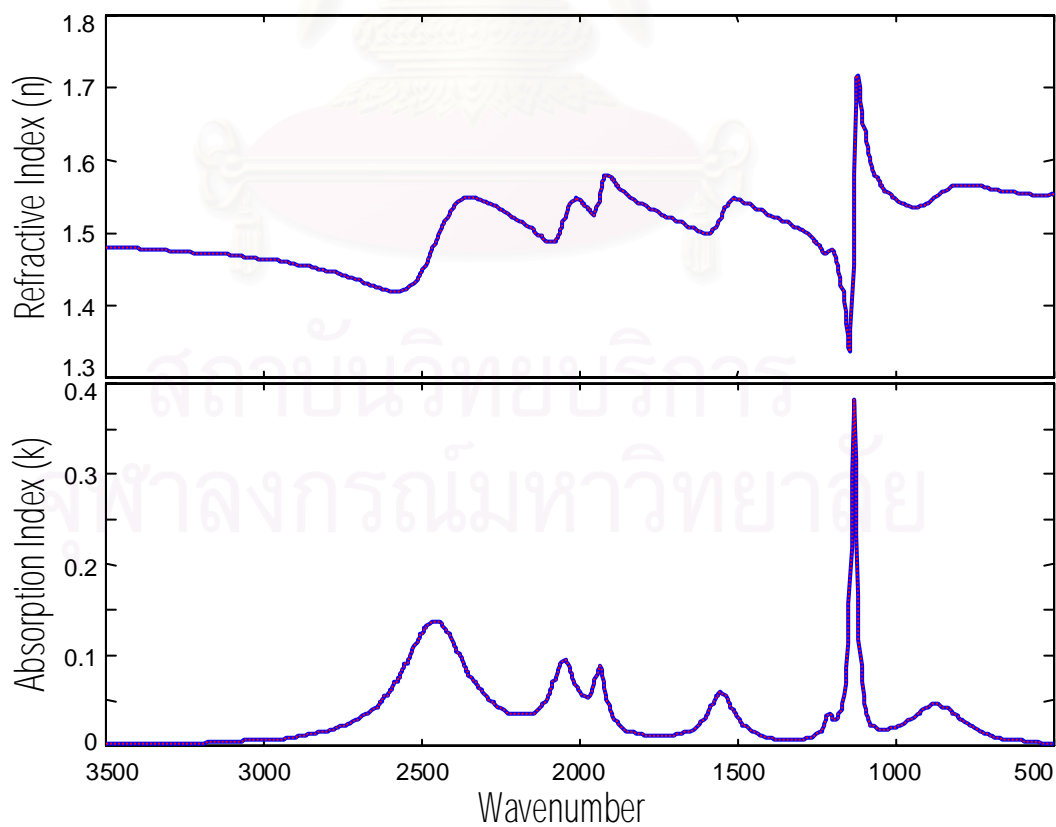
Figure 4.13 Comparison of estimated and presetting of *n* and *k* under the situation of total internal reflection: calculation (solid lines), and presetting (dotted lines).

According to the results shown in Figures 4.11, 4.12 and 4.13, the calculated n and k spectra yielding from the subprogram Rdel2nk were very closed to the preset values. From the Table 4.3, the error of n and k predictions for total internal reflection are very low, *i.e.*, 0.005% and 0.1% error of n and k predictions, respectively. However, the results are fair, *i.e.*, 0.2% and 7.2% error of n and k predictions for internal reflection, and 0.3% and 14.7% error for external reflection.

4.2.4 MMCR Subprogram

The subprogram MMCR was created to perform the multivariate curve resolution (MCR) as described in Section 2.2.2. MMCR was used to resolve the complicated spectra in order to reveal concentration and absorptivity profiles from a set of observed spectra. The algorithm of MMCR was shown in Section 3.2. To verify the subprogram, two simulated systems were employed: system of acid dissociation and system of zero-order kinetics. These two systems have different features in application. The first one represented the thermodynamic system, while the second one represented the kinetic system.

4.2.4.1 System of acid dissociation. In this case, an acid namely H_2A is dissociated and can be represented by the following expression.

$$H_2A \xrightleftharpoons{K_{a1}=1.23\times10^{-4}} H^+ + HA^-$$

$$HA^- \xrightleftharpoons{K_{a2}=2.34\times10^{-7}} H^+ + A^{2-} \tag{4.4}$$
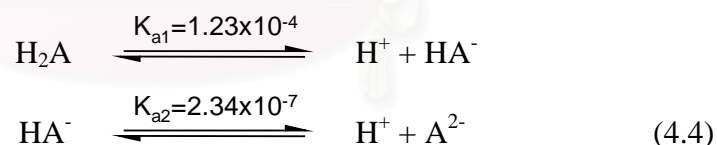
where K_{a1} and K_{a2} are represented the dissociation (or deprotonation) constants. Evidently, there are three components: H_2A, HA^- and A^{2-} in the system.

The absorptivities of each component were simulated by Gaussian and/or Lorentzian peak-shapes[6,32] and shown in Figure 4.14 (A). The concentrations of each component were calculated by the following expression.[31]

$$\frac{1}{\alpha_m} = \left(\sum_{i=0}^{m-1} \frac{\left[H^+\right]^i}{\prod\limits_{j=1}^{i} K_{a(m-j)}} \right) + \left(\sum_{\substack{i=1 \\ m<k+1}}^{k-m+1} \frac{\prod\limits_{j=m}^{i+m-1} K_{a(j)}}{\left[H^+\right]^i} \right) \tag{4.5}$$

where α_m is the degree of acid formation of the mth component (*i.e.* the mole ratio of the mth component with respect to all components). The concentration profiles of each component in the acid dissociation system were shown in Figure 4.14 (B).
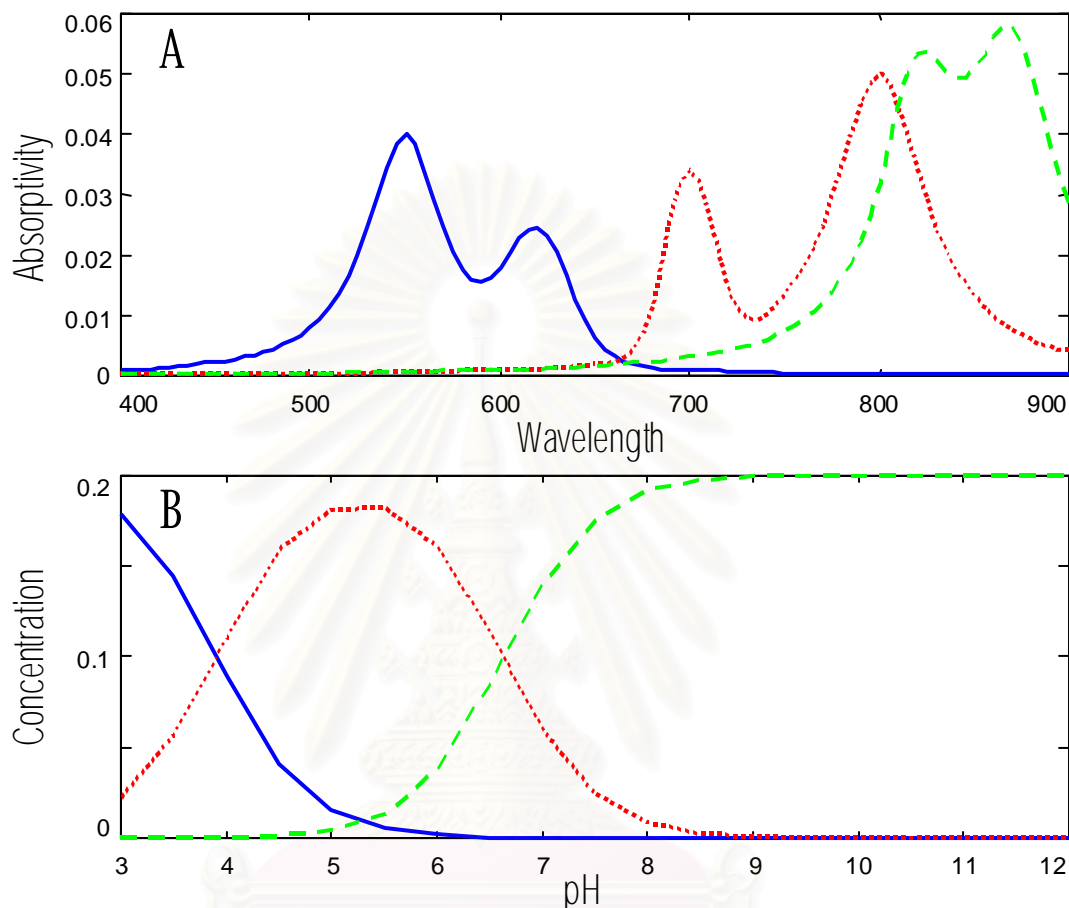
Figure 4.14   Simulated absorptivities (A) and concentration profiles (B) of all three components: H_2A (solid lines), HA^- (dotted lines) and A^{2-} (dash lines) in the acid dissociation system.

The spectra based on Beer's law of the system are simulated and shown in Figure 4.15 (A). Then the spectra were added with random noise of ±0.0001 absorbance unit (*i.e.*, approximate 10% of relative noise level of the mean absorbance values). This noise level is high enough to make the simulated spectra similar to the actual experimentally observed spectra. The spectra with added noise were shown in Figure 4.15 (B) and (C). The subprogram MMCR was invoked to resolve the spectra to obtain the estimated absorptivities and concentrations. The constraints of non-negativity and constant total concentration as described in Section 2.2.2 were employed in the calculation process. The predictions were compared to the set values, and shown in Table 4.4 and Figure 4.16.

To test the robustness of the subprogram, the pure spectra were added with random noise of various amplitudes from 0 to ±0.0005 absorbance unit, and input to the program. The results of prediction were shown in Table 4.5 and Figure 4.17.

Figure 4.15   Simulated noise-free spectra (A), noise-added spectra (B), and the corresponding 3D plot of the noise-added spectra (C).

Table 4.4 Testing results of absorptivities and concentrations of MMCR subprogram
of the simulated system of acid dissociation.

Prediction	Error of Prediction		
	Norm	rms	nrms
Absorptivity Profile	0.0075	4.286×10^{-4}	2.4
Concentration Profile	0.0267	3.530×10^{-3}	3.4
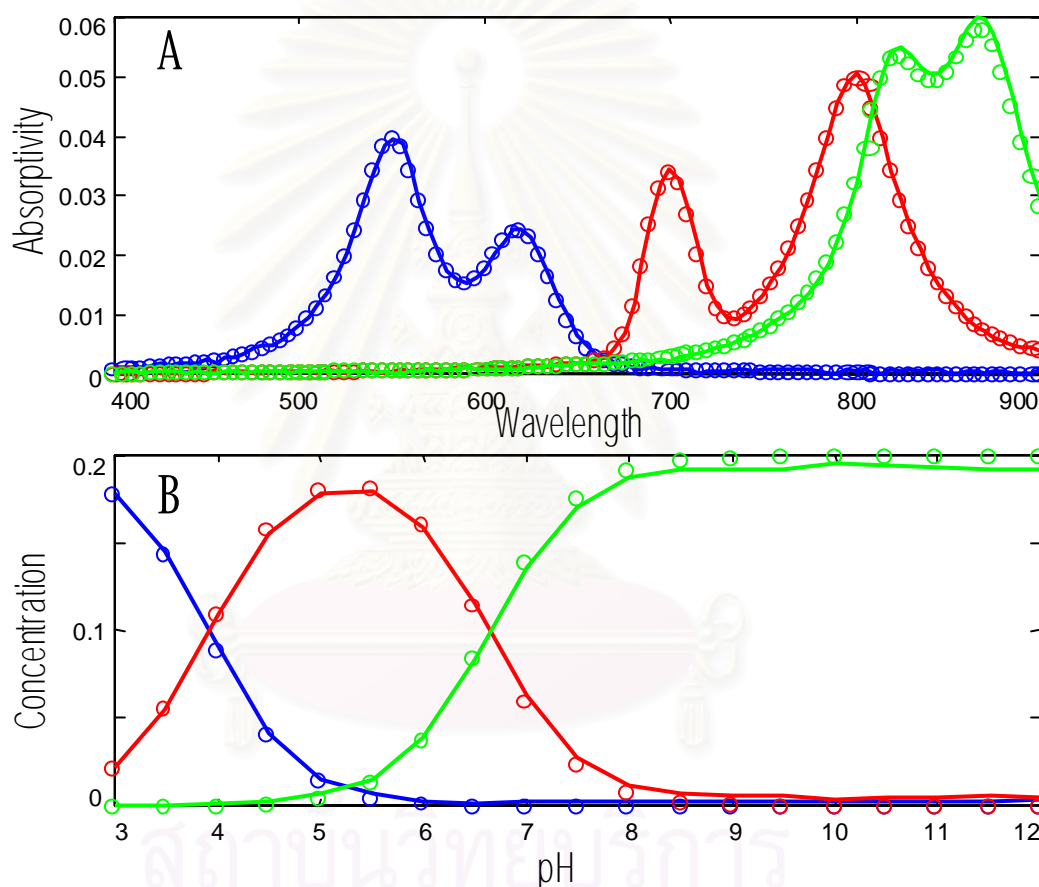
Figure 4.16 Comparison between estimated (solid lines) and presetting (open
circles) of absorptivity (A) and concentration (B) profiles.

From the results, the three components were explicitly resolved
without cross-contamination among each component. The absorptivity and
concentration profiles agree very well with the preset values (2.4% and 3.4% for the
error of predictions of absorptivity and concentration profiles, respectively). It can be
concluded that the subprogram MMCR worked well for the simulated system of acid
dissociation of three components with high accuracy.

Table 4.5 Testing results of the robustness of the MMCR subprogram.

Noise Level	Error of Absorptivity Prediction			Error of Concentration Prediction		
	Norm	rms	nrms	Norm	rms	nrms
0 (0%)	0.0068	3.886×10^{-4}	2.16	0.0267	3.538×10^{-3}	3.37
±0.0001 (9.09%)	0.0075	4.286×10^{-4}	2.38	0.0267	3.530×10^{-3}	3.37
±0.0002 (18.18%)	0.0071	4.064×10^{-4}	2.26	0.0135	1.799×10^{-3}	1.72
±0.0003 (27.27%)	0.0134	7.702×10^{-4}	4.28	0.0217	3.266×10^{-3}	3.11
±0.0004 (36.36%)	0.0255	1.466×10^{-3}	8.14	0.0471	6.242×10^{-3}	5.95
±0.0005 (45.45%)	0.0382	2.193×10^{-3}	12.18	0.1009	1.337×10^{-2}	12.74

Figure 4.17   Error of predictions of absorptivities (solid line) and concentrations (dotted line) at noise level from 0 to ±0.0005 absorbance unit.

According to Table 4.5 and Figure 4.17, the algorithm of MMCR subprogram is valid until the noise level is up to ±0.0003 absorbance unit or approximately 30% of the mean absorbance values. At a high noise level, the predictions were poor while the profiles of each component interfered with others.

4.2.4.2 System of zero-order kinetics. In this case, the technique was applied to resolve mixture consist of two components: A and B. The component A changed to B in the range of monitoring time. There are clearly two components in the system.

The absorptivities of each component were simulated by Gaussian and/or Lorentzian peak-shapes,[6,32] and shown in Figure 4.18 (A). The concentrations of each component were calculated by treating the reaction as zero-order kinetics as

$$\frac{d[A]}{dt} = -k_0 \tag{4.6a}$$

$$[A] = [A]_0 - k_0 t \tag{4.6b}$$

$$[B] = [A]_0 - [A] \tag{4.6c}$$

where k_0 is the zero-order rate constant, and t is the monitoring time. The concentration profiles were shown in Figure 4.18 (B).
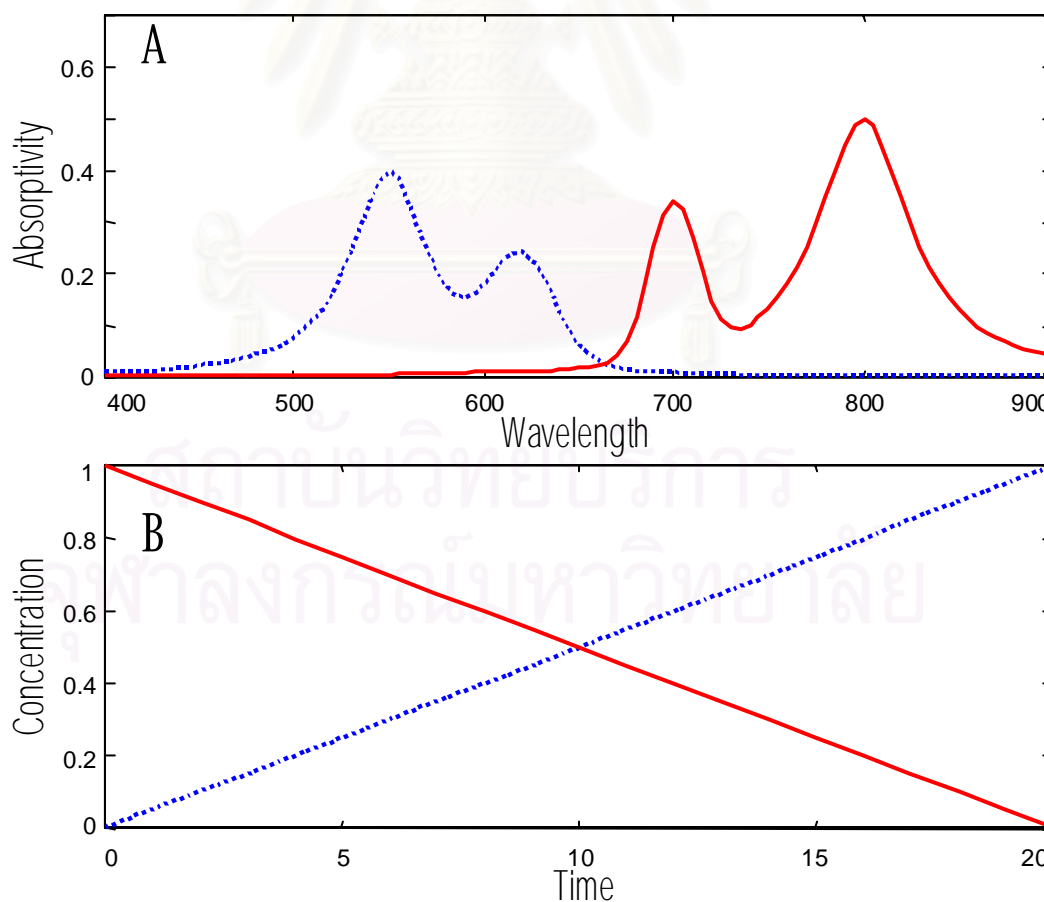
Figure 4.18 Simulated absorptivity (A) and concentration (B) profiles of component A (solid lines) and component B (dotted lines).

Analogous to the Section 4.2.4.1, the spectra were calculated by Beer's law and shown in Figure 4.19 (A). Then the spectra were added with random noise of ±0.005 absorbance unit (*i.e.*, approximately 10% of the mean absorbance values). The spectra with noise addition were shown in Figure 4.19 (B) and (C). Again the subprogram MMCR, and the constraints of non-negativity and constant total concentration were used to extract the absorptivity and concentration profiles from the noise-added spectra. The predictions were compared to the former setting, and shown in Table 4.6 and Figure 4.20.

The robustness of the subprogram to the system of zero-order kinetics was also investigated by varying the level of random noise from 0 to ±0.025 absorbance unit. The results of prediction were shown in Table 4.7 and Figure 4.21.

From the results, the system of zero-order kinetics was resolved by the MMCR subprogram to reveal the absorptivity and concentration profiles of each component. The profiles agree very well with the preset values (1.0% and 0.7% for the error of predictions of absorptivity and concentration profiles, respectively). It can be concluded that the subprogram MMCR worked well for the simulated system of zero-order kinetics with high accuracy. Moreover, the algorithm of the subprogram is valid for this system until the noise level is up to ±0.025 absorbance unit or 50% of the mean absorbance values.
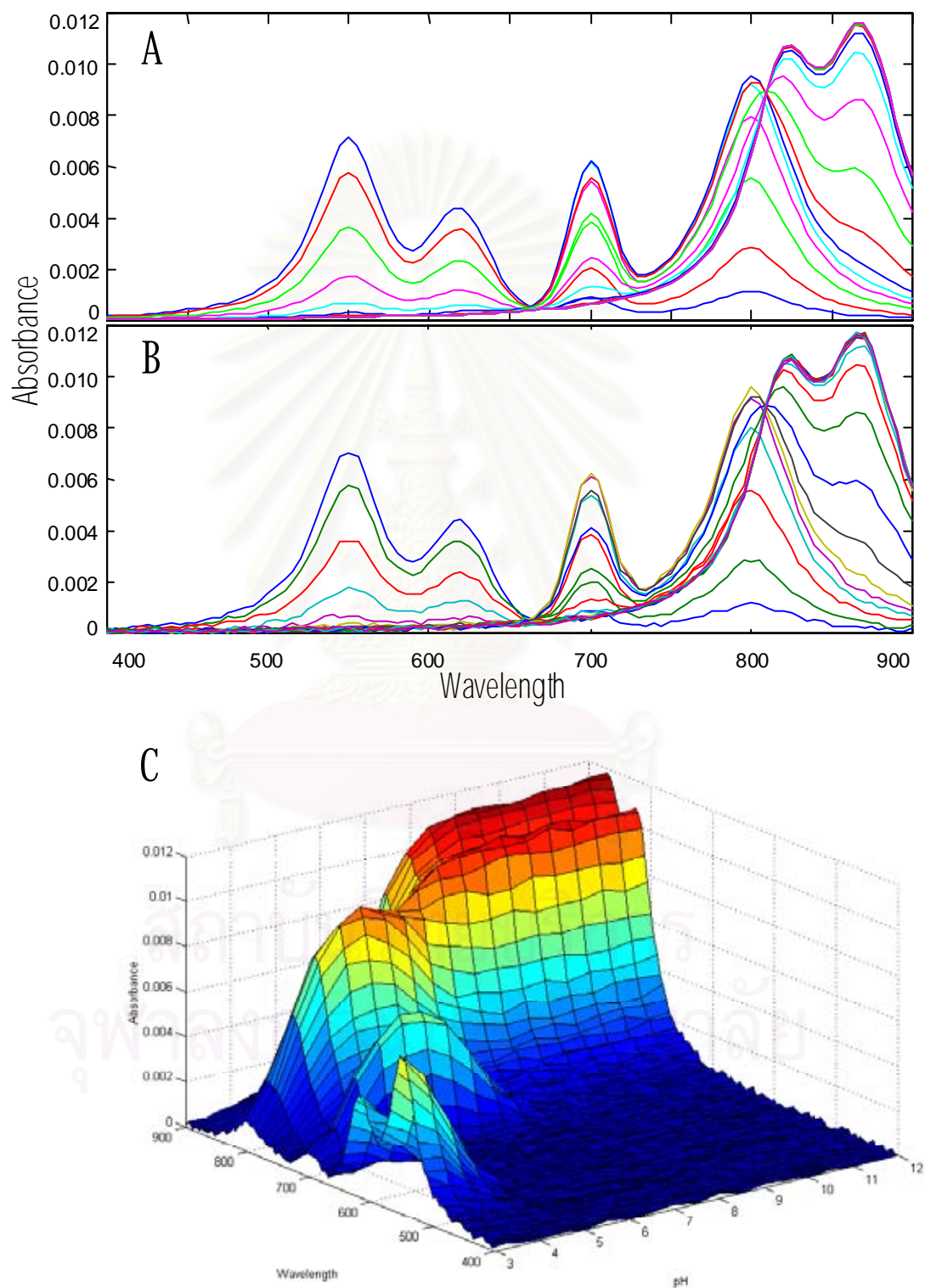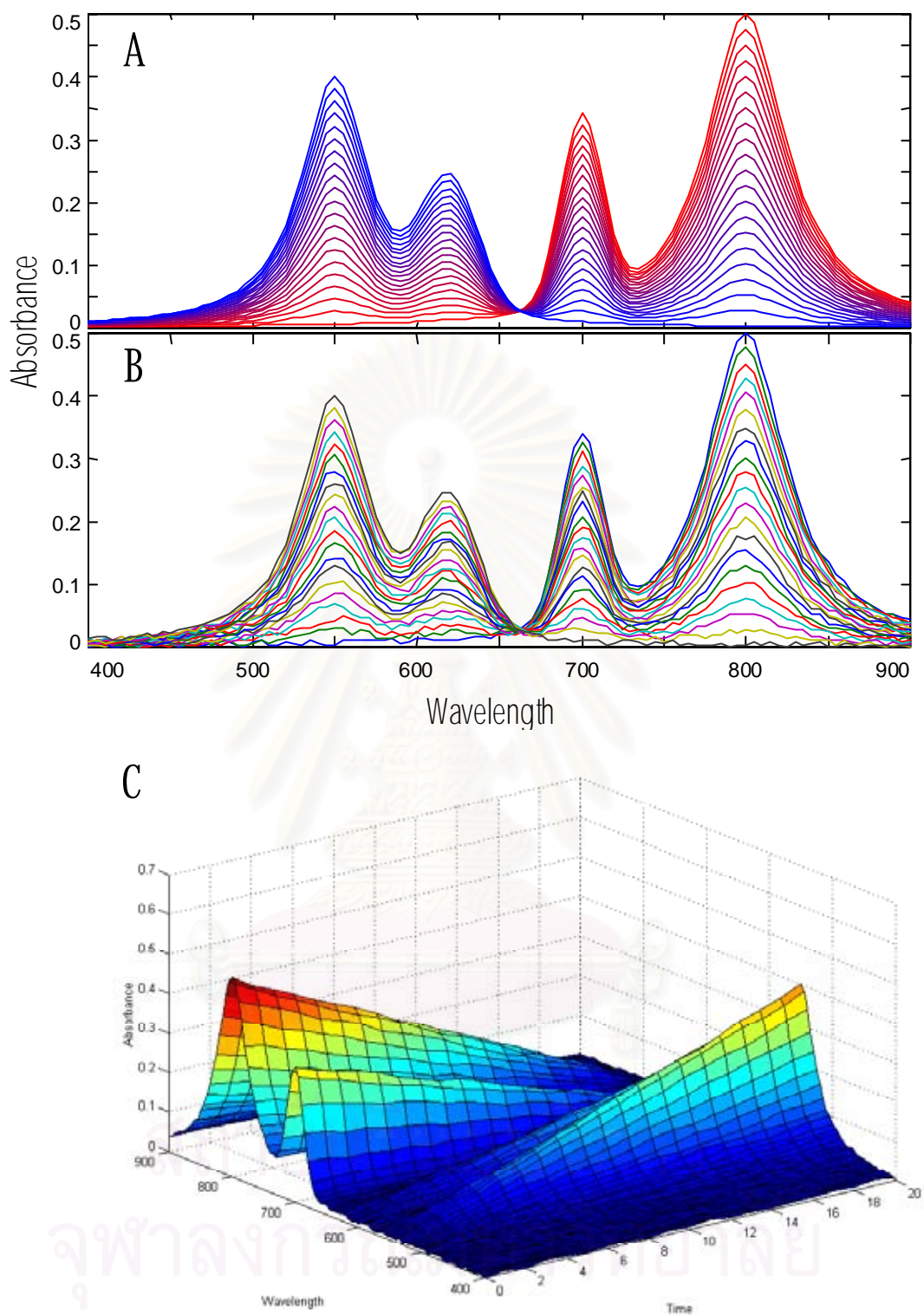
Figure 4.19 Simulated noise-free spectra (A), noise-added spectra (B), and
the corresponding 3D plot of the noise-added spectra (C).

Table 4.6 Testing results of absorptivities and concentrations of MMCR subprogram
of the simulated system of zero-order kinetics.

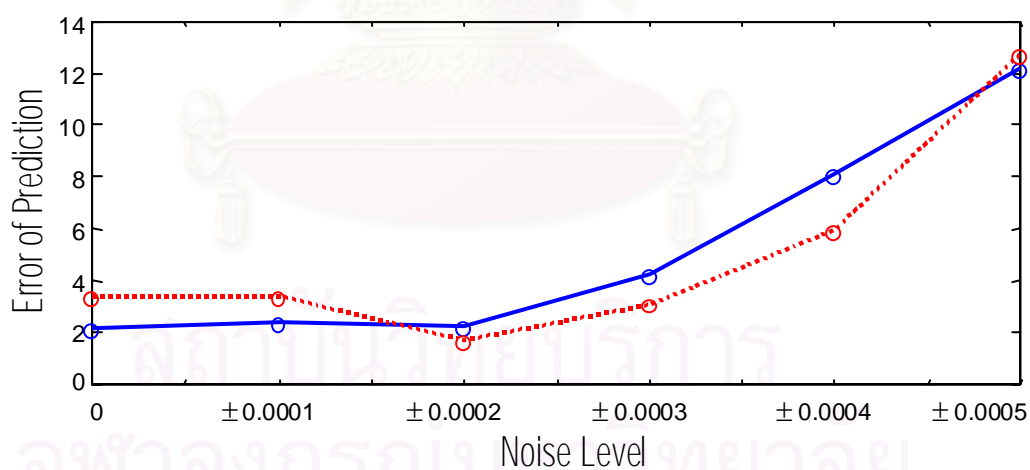| Prediction	Error of Prediction		
	Norm	rms	nrms
Absorptivity Profile	0.0217	1.523×10^{-3}	1.0
Concentration Profile	0.0275	4.243×10^{-3}	0.7
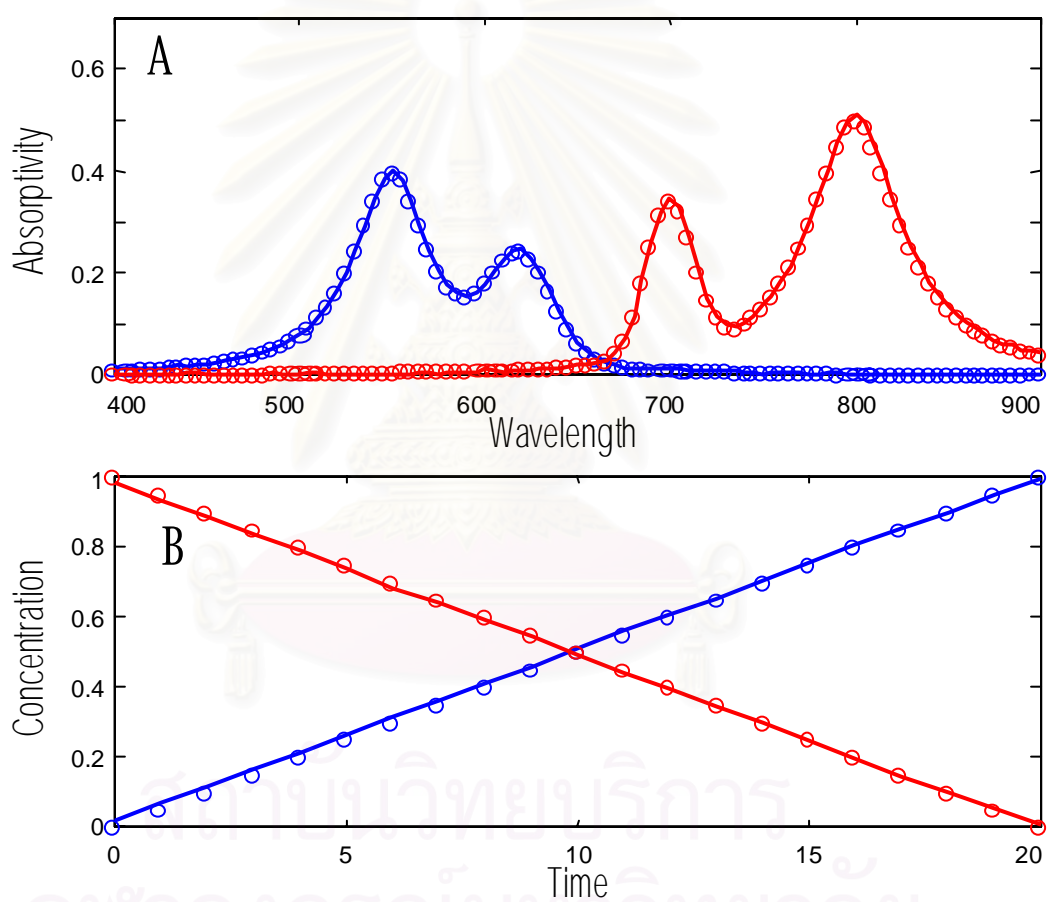
Figure 4.20 Comparison between estimated (solid lines) and presetting (open
circles) of absorptivity (A) and concentration (B) profiles.

Table 4.7 Testing results of the robustness of the MMCR subprogram.

Noise Level	Error of Absorptivity Prediction			Error of Concentration Prediction		
	Norm	rms	nrms	Norm	rms	nrms
0 (0%)	0.0167	1.177×10^{-3}	0.78	0.0302	4.665×10^{-3}	0.79
±0.005 (11.36%)	0.0227	1.597×10^{-3}	1.06	0.0266	4.109×10^{-3}	0.70
±0.010 (22.73%)	0.0370	2.605×10^{-3}	1.73	0.0274	4.226×10^{-3}	0.72
±0.015 (34.09%)	0.0562	3.956×10^{-3}	2.62	0.0479	7.393×10^{-3}	1.26
±0.020 (45.45%)	0.0729	5.133×10^{-3}	3.40	0.0582	8.977×10^{-3}	1.54
±0.025 (56.82%)	0.0919	6.465×10^{-3}	4.29	0.0635	9.797×10^{-3}	1.68
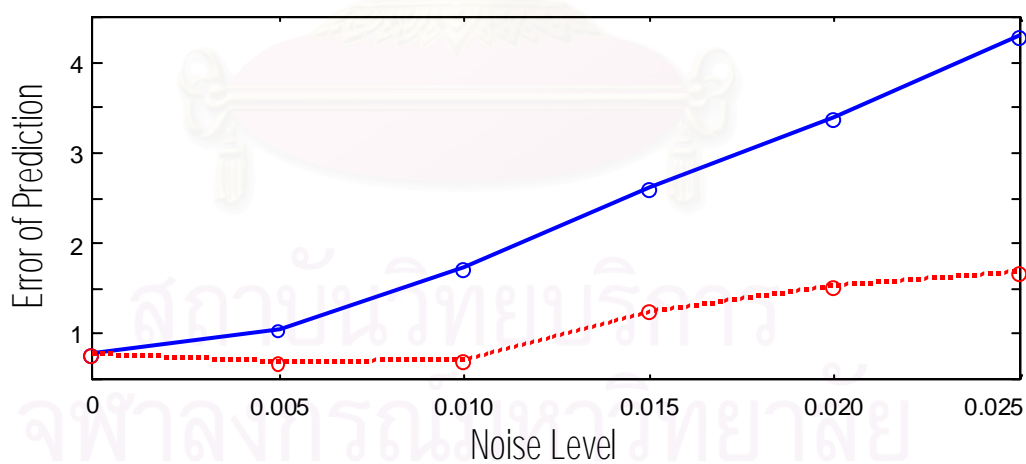
Figure 4.21 Error of predictions of absorptivities (solid line) and concentrations (dotted line) at noise level from 0 to ±0.025 absorbance unit.

4.3 Validation of the Whole Program

The program `WizardIR` was validated by the evaporated system of volatile mixtures. The system was simulated in such a way that the system is similar to the real experiment as described in Chapter 5 as possible. All mathematical formulations were described in Chapter 2.

The simulation composed of three artificial components: A, B and C. All components were mixed with equal starting volumes and treated as ideal solution.[36] The concentration variation in the system was initiated by the difference in the evaporation rate of each component. The absorptance spectra of mixtures at various compositions were calculated under the total internal reflection condition at specific periodic time interval.

As previous manner in the Section 4.2.1, the n and k spectra of three components were simulated by antisymmetric linear combination of Lorentzian functions and shown in Figure 4.22. Instead of using concentration as molarity, the volume fraction (ϕ) was used as the quantitative parameter. The profiles of volume fractions of the three components were calculated by eq. 2.66, and shown in Figure 4.22.

The absorptance of mixtures at any observed time was calculated by eq. 2.61 and shown in Figure 4.23 (A). Then the absorptance spectra were added with random noise of ±0.0005 absorptance unit (*i.e.* approximate 10% of the mean absorptance values). The spectra with added noise were shown in Figure 4.23 (B) and (C).

The program `WizardIR` was used to resolve the absorptance spectra by the subprogram `MMCR` to first obtain the estimated profiles of the volume fraction and the absorptance coefficient (κ). Then the n and k of each component were extracted from absorptance coefficient by the subprogram `MKKT`, `MsimRdel`, `MR2del` and `MRdel2nk`. The results of prediction were compared to the presetting, and shown in Figure 4.24 and Table 4.8.
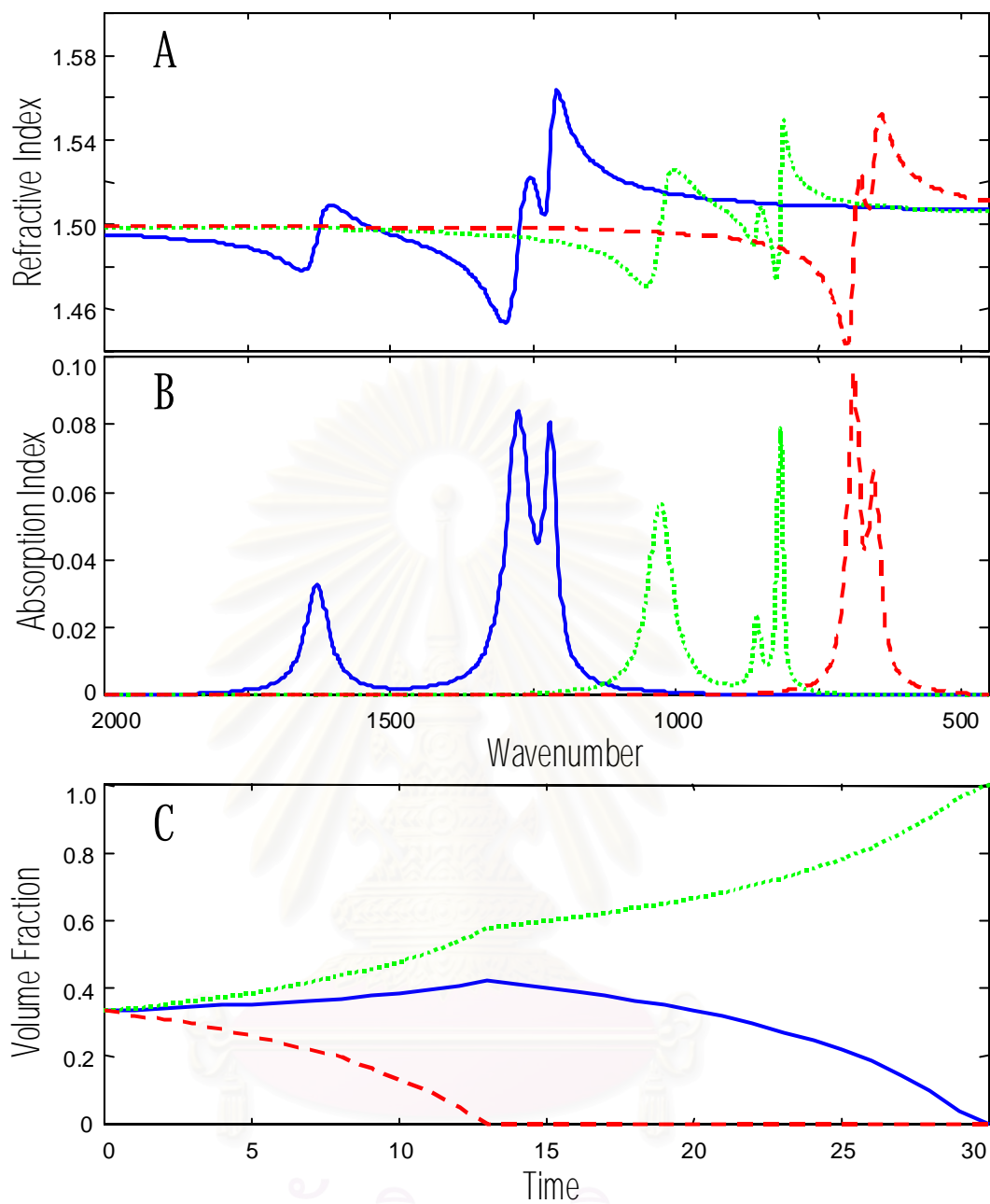
Figure 4.22 Simulated refractive index (A), absorption index (B) and volume fraction (C): component A (solid lines), component B (dotted lines) and component C (dash lines).
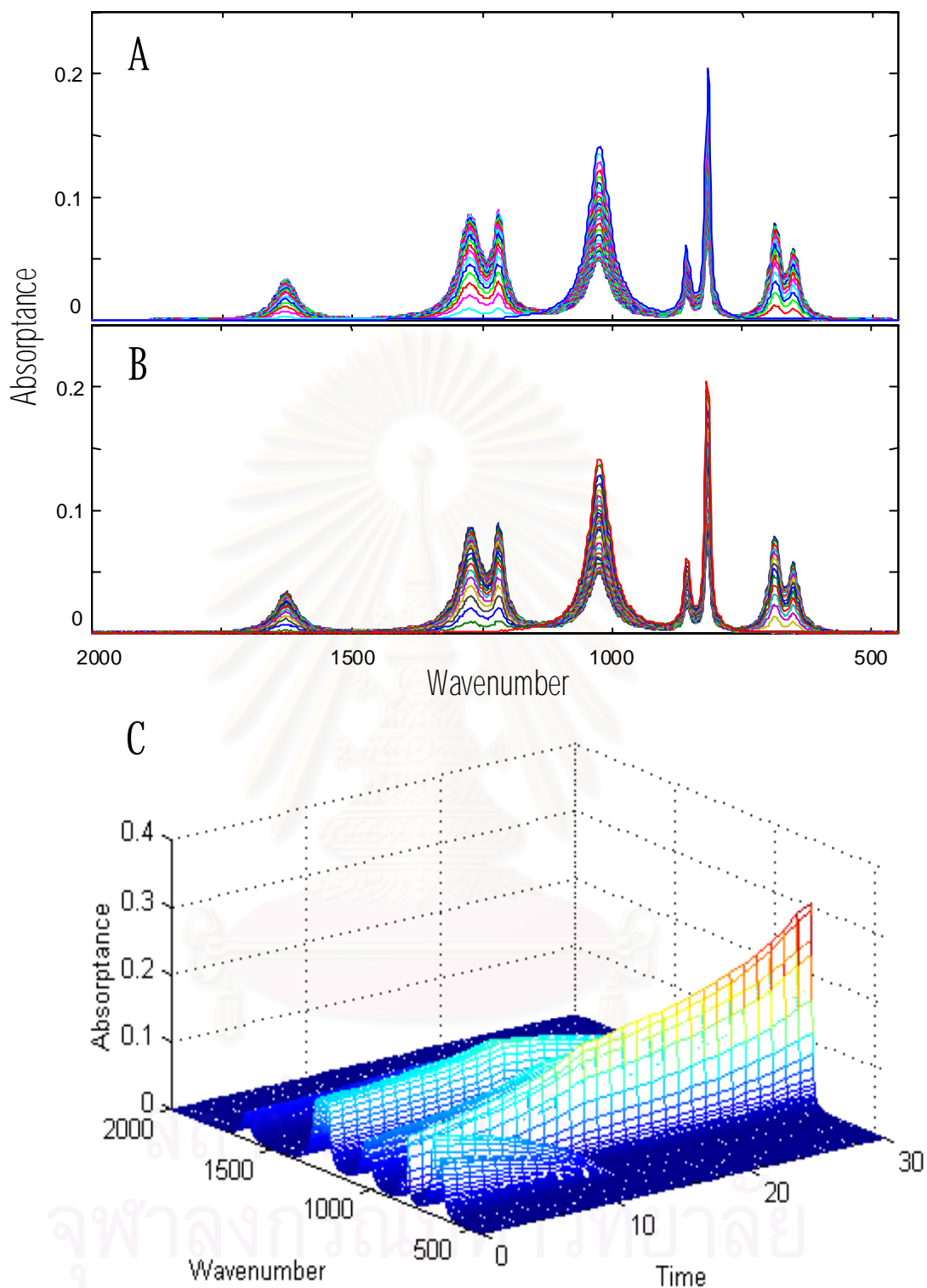
Figure 4.23 Simulated noise-free absorptance spectra (A), noise-added
absorptance spectra (B), and the corresponding 3D plot
of the noise-added spectra (C).
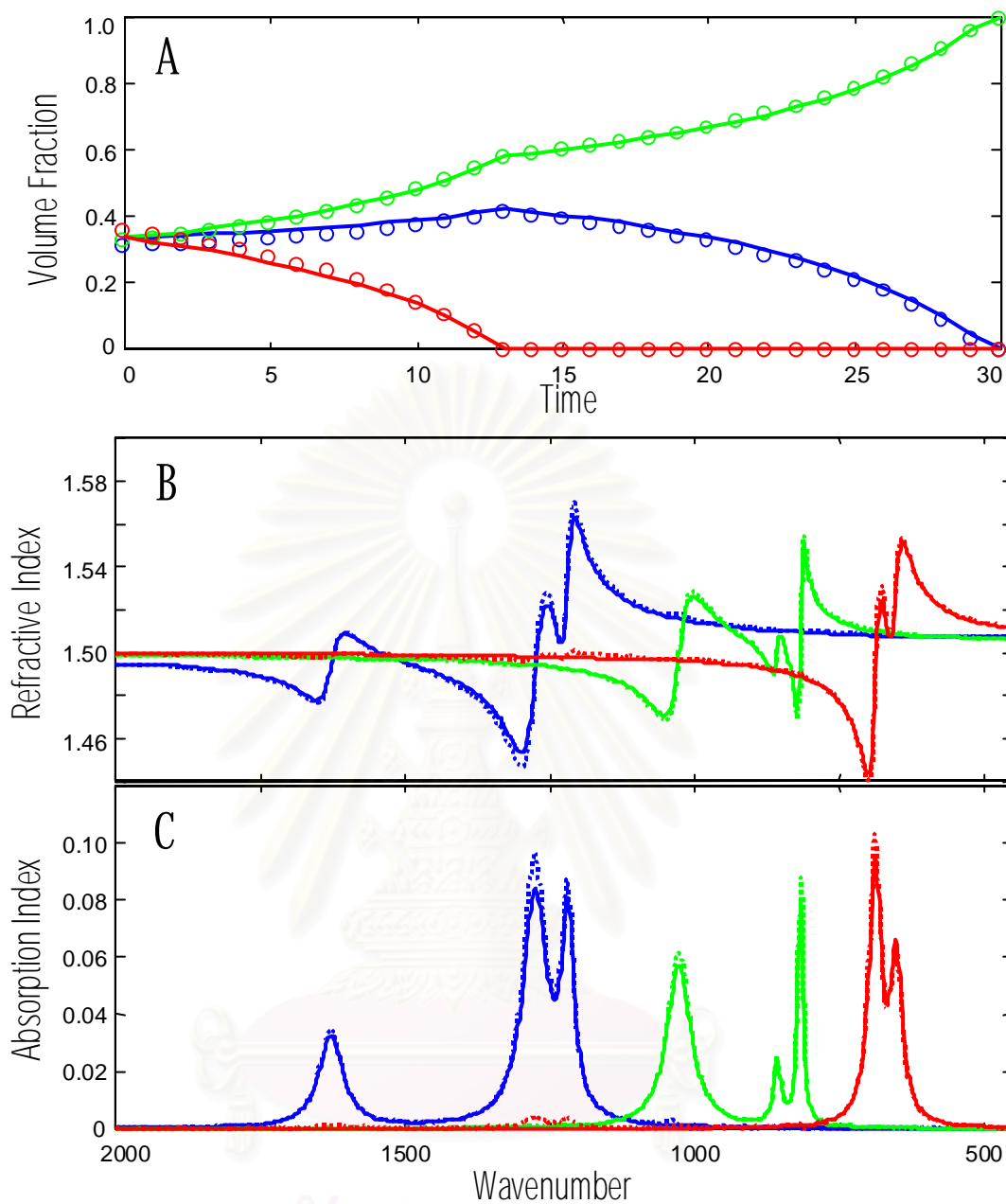
Figure 4.24 Comparison between estimated (open circles and dotted lines) and
presetting (solid lines) of volume fraction (A), refractive index (B)
and absorption index (C) profiles.

Table 4.8 Testing results of volume fraction, refractive index and absorption index of
the simulated system of three volatile components.

Prediction	Error of Prediction		
	Norm	rms	nrms
Volume Fraction	0.0416	4.317×10^{-3}	1.03
Refractive Index	0.0652	1.351×10^{-3}	0.09
Absorption Index	0.0656	1.365×10^{-3}	9.51

From the results, the program `WizardIR` could resolve the absorptance spectra of mixtures to reveal the profiles of each component. The obtained profiles of volume fraction agree very well (1.03% error) with the preset values.

It should be noted that the above simulation of three volatile components were treated as an ideal solution. The deviation may occur when the system of non-ideal solution was employed.

CHAPTER V

EXPERIMENTAL

In this research, the experiments were separated into 2 parts:

1 Mixture of three evaporated compounds
2 Polymer crystallization[33]

5.1 Mixture of Three Evaporated Compounds

5.1.1 Chemicals and Instruments

5.1.1.1 Chemicals. All used chemicals were tabulated in Table 5.1.

Table 5.1 List of the chemicals used.

Chemicals	Purity and Source
Methanol	99.8% from Merck
Toluene	99.5% from Carlo Erba
Acetone	99% from Merck

5.1.1.2 Instruments

1. Zinc selenide (ZnSe) liquid cell
2. FT-IR spectrometer: Nicolet Magna 750 Series II

5.1.2 Preparation of Solution

A mixture of acetone, methanol and toluene was prepared by pipetting of 3 mL of acetone, 3 mL of methanol and 1 mL of toluene into a beaker, and then swirling well for homogeneous mixing.

5.1.3 Measurements

1) ATR FT-IR spectra of the mixture were acquired using a commercial ATR accessory. A Zinc selenide ATR crystal was employed. Approximately 1 cm^3 of the solution was filled up into the liquid cell. The solution in the liquid cell was left in the sample chamber for a free evaporation. During the evaporation, ATR spectra of the solution were collected, and stored for further calculation.

2) All infrared spectra were recorded as a function of time with the following acquisition parameters.

Spectral resolution	4.0 cm^{-1}
Number of scans	8
Result spectrum	Absorbance
Gain amplifier	1
Light source	Globar
Detector	Deuterated triglycine sulfate (DTGS)
Beam splitter	KBr

3) Spectra of each pure component were measured using the same experimental condition.

5.2 Experiment of Polymer Crystallization

A sample film of poly(3-hydroxybutyrate-*co*-3-hydroxyhexanoate) was prepared by casting its chloroform solution on a CaF$_2$ window. After the solvent casting, the sample film was air-dried for 30 minutes before the measurements. The infrared spectrum of the sample film was measured after the solvent evaporated showed no spectroscopic evidence for the presence of chloroform. The time-dependent infrared spectra were collected at room temperature by using the Thermo Nicolet Magna-IR^{TM} 550 spectrometer with a time interval of 15 minutes until the crystal growth was completed (*i.e.*, no significant spectral change was observed after

prolonged measurement). The acquisition parameters for instrumental setup were listed below.

Spectral resolution	2.0 cm^{-1}
Number of scans	512
Result spectrum	Absorbance
Gain amplifier	1
Light source	Globar
Detector	Mercury cadmium telluride (MCT)
Beam splitter	KBr

CHAPTER VI

RESULTS AND DISCUSSION

6.1 Experiment of Three Evaporated Compounds

The mixture of acetone, methanol and toluene was prepared with volume ratio of 3:3:1. The solution is then filled into the ZnSe liquid cell. The infrared spectra of the mixture were recorded as a function of time as shown in Figure 6.1. The infrared spectra of each pure compound in the mixture were also taken separately and are shown in Figure 6.2. The spectra were converted to ASCII format and input to the program `WizardIR`. The program instruction was described in the Appendix. The results of prediction were shown in Figure 6.3.
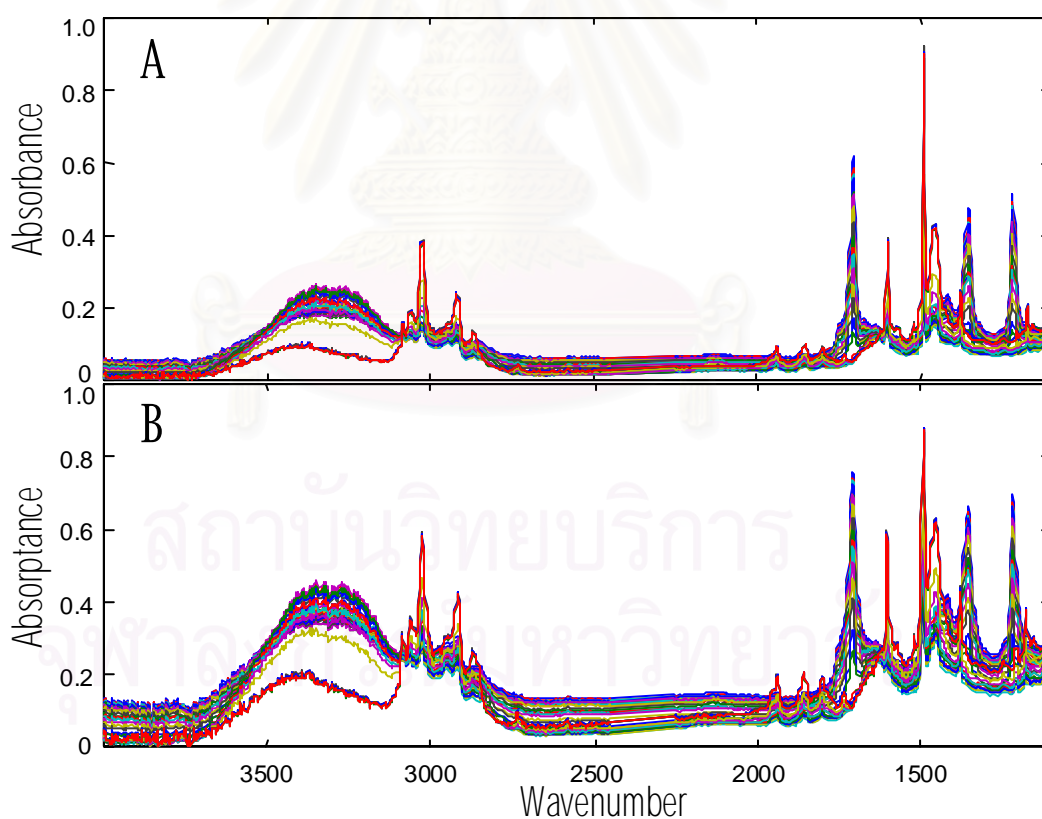
Figure 6.1 Absorbance (A) and absorptance (B) spectra of the mixture of acetone, methanol and toluene.
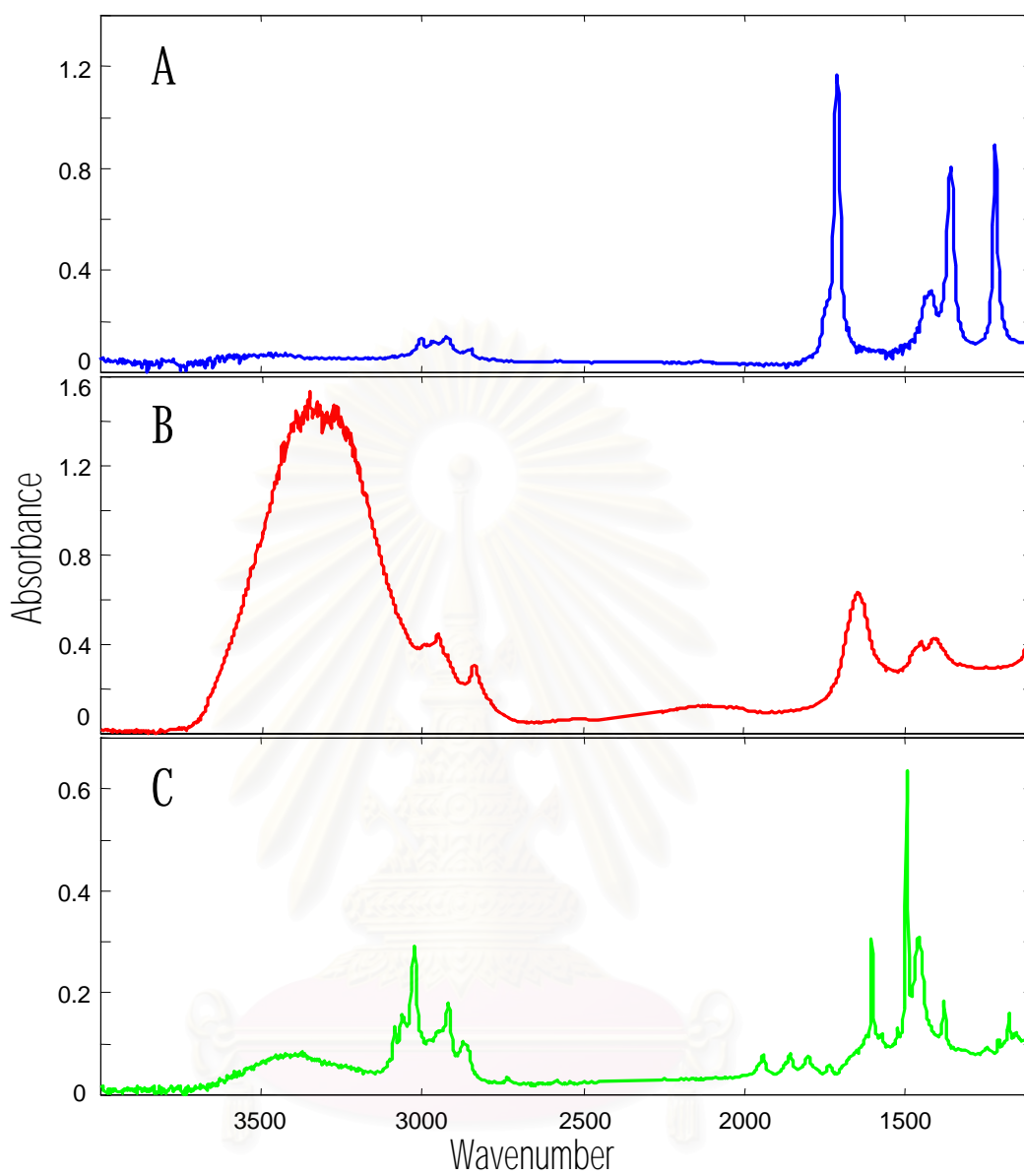
Figure 6.2 Absorbance spectra of the three pure compounds: acetone (A),
methanol (B) and toluene (C).
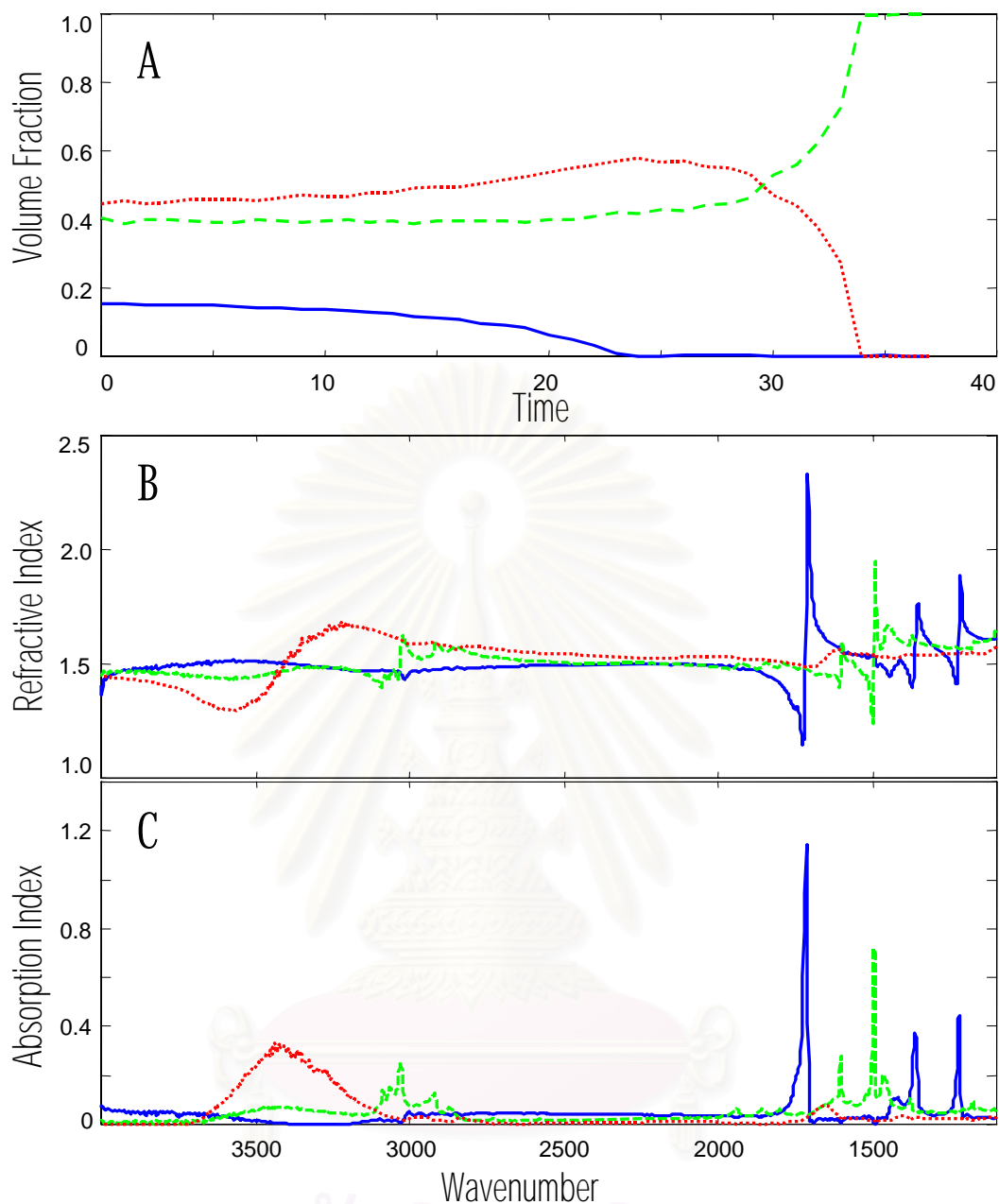
Figure 6.3 Estimated profiles of volume fraction (A), refractive index (B) and absorption index (C) of the three components in the mixture: acetone (solid lines), methanol (dotted lines) and toluene (dash lines).

According to Figure 6.3, acetone was fastest evaporation and toluene is the slowest evaporation compared in the solution. However the starting volume ratio of the three compounds were not agreed with the experimental setup. This is due to the facts that

i) the experiment was not real-time analysis,

ii) the time gap from solution preparation until the proper time of measurement may cause the changes in starting volume ratio,

iii) due to the problem of over-absorption in the spectra during the first five minutes of measurements. The spectra with over-absorption bands were discard.

To examine the accuracy of the prediction, the resolved spectra were compared to that of the reference spectra. The comparisons are shown in Figure 6.4. The program prediction agrees very well with the reference spectra. The characteristic peaks of each compound were matched as list below.

Acetone: $C = O$ stretching at 1725-1705 cm^{-1}
                  $C – CO – C$ skeletal at 1325-1215 cm^{-1}

Methanol: $O – H$ stretching at 3600-3100 cm^{-1}
                  $C – H$ asymmetric stretching at 2975-2950 cm^{-1}
                  $C – H$ symmetric stretching at 2885-2860 cm^{-1}

Toluene: $C – C$ stretching at 1600,1500 and 1480 cm^{-1}
                  $C – H$ stretching at 3100-3000 cm^{-1}
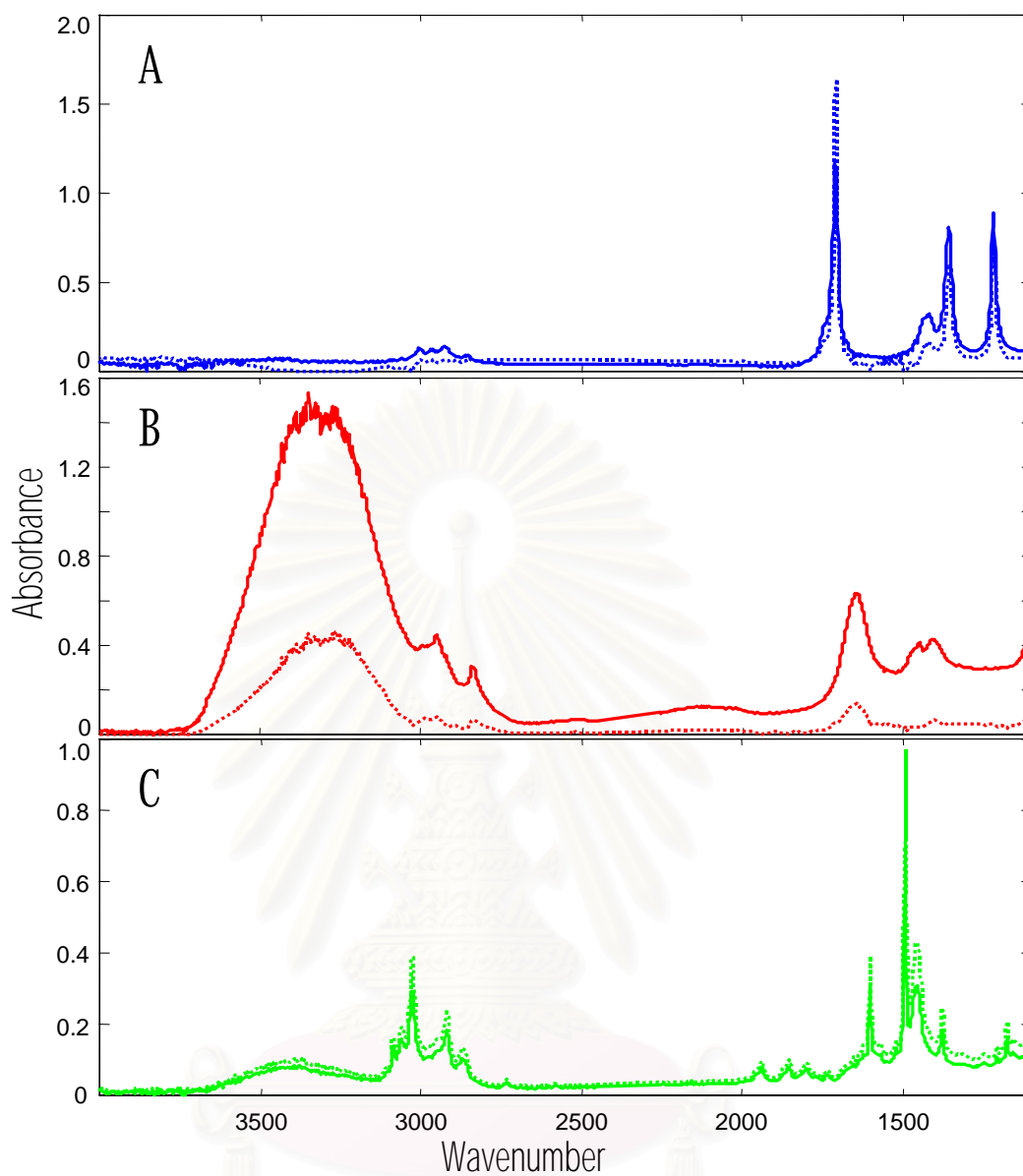
Figure 6.4 Comparison between the estimated (dotted lines) and pre-known
(solid lines) absorbance spectra of the three components in
mixture: acetone (A), methanol (B) and toluene (C).

6.2 Experiment of Polymer Crystallization

The time-dependent spectra of polymer crystallization were shown in Figure 6.5. The spectra were converted into ASCII format and input to the program. The results of prediction were shown in Figure 6.6.
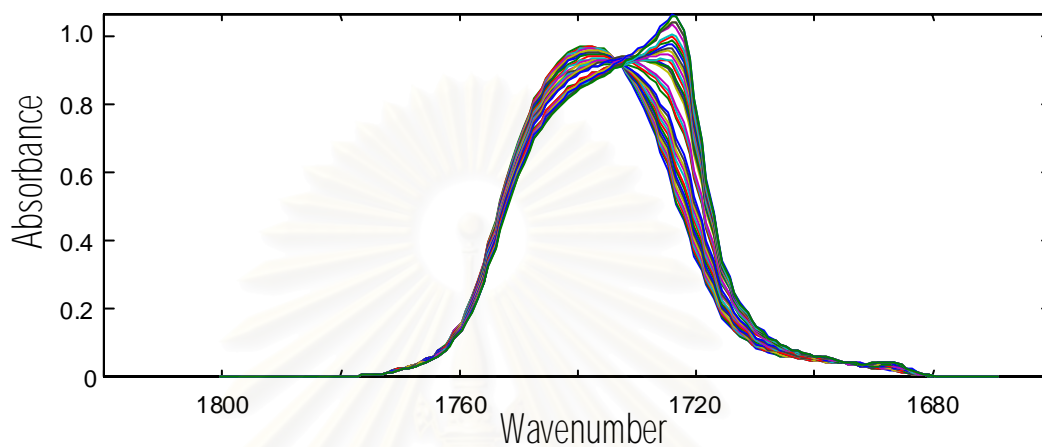
Figure 6.5 Time-dependent spectra of the polymer crystallization.
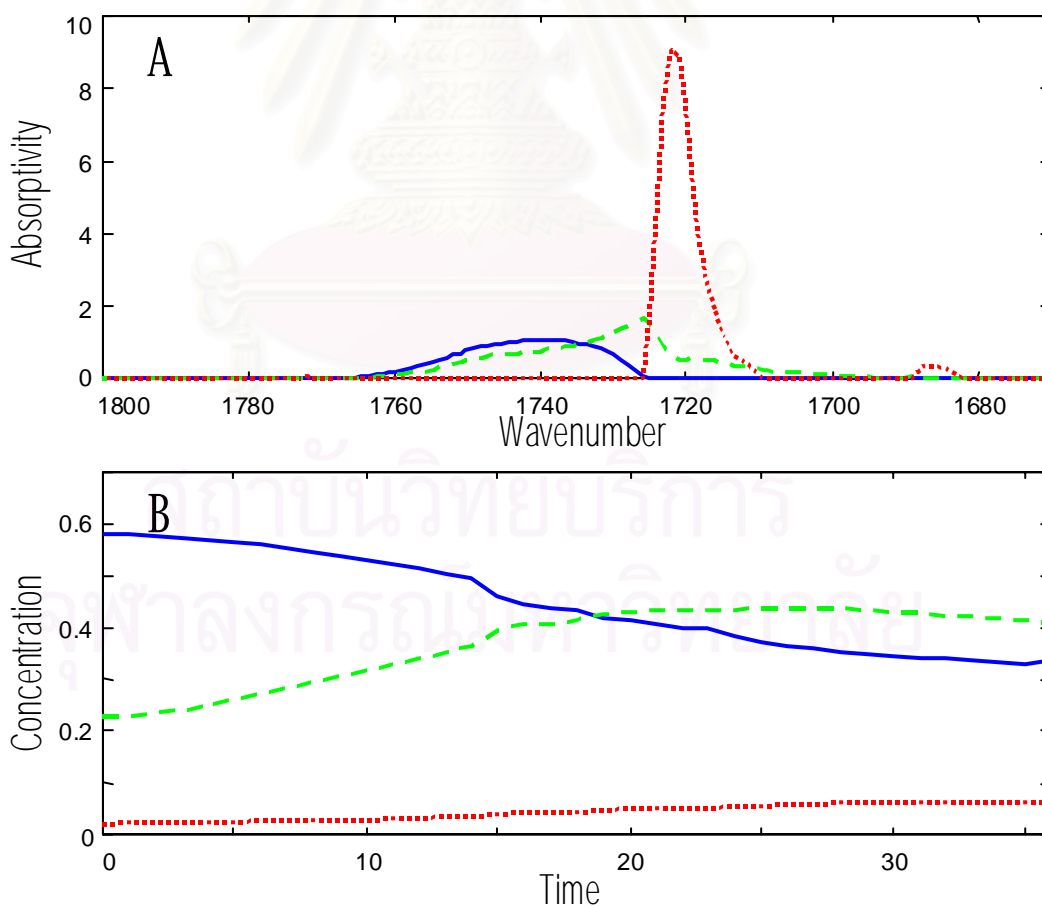
Figure 6.6 Estimated profiles of absorptiviy (A) and (normalized) concentration (B) of the polymer crystallization: amorphous (solid lines), less-order crystalline (dash lines) and high-order crystalline (dash lines) forms.

Figure 6.6 (C) indicated that there are three components: amorphous, less-order crystalline and high-order crystalline forms. As seen in Figure 6.6, the amorphous form was crystallized into the less- and high-order crystalline forms. The characteristic peaks of amorphous, less-order crystalline and high-order crystalline forms are 1740, 1726 and 1722 cm^{-1}, respectively. In addition, the results agree with the prediction of Yoshie et al.[34] that was evaluated by curve fitting and 2D correlation.

CHAPTER VII

CONCLUSIONS

Program `WizardIR` version 1.0 was developed to resolve the infrared spectra of multicomponent mixtures using the chemometric methods such as principal component analysis and multivariate curve resolution. The obtained results are the profiles of concentration (in term of volume fraction or normalized concentration) and absorptance coefficients (or absorptivity) of each component in the mixtures. The profiles of absorptance coefficient would be used to determine the optical constants using Kramers-Kronig transformations and numerical optimization. As demonstrated in Chapter 4 and 6, the program works well on the data that obtained by simulation and experiment. However, some comments should be noted here.

i) The program `WizardIR` version 1.0 contains fourteen files as listed in Table 3.1. The subprograms `MRdel2nk`, `MR2del`, `MsimRdel` and `MKKT` were used to determine the optical constants by Kramers-Kronig transformation while the subprograms `MMCR`, `MPFA`, `MErr` and `MFindPrimary` were employed to resolve the spectra of multicomponent mixtures by the chemometric methods.

ii) According to the theoretical simulations, the subprograms of optical constants determination worked well under the total internal reflection. However, the accuracy of results were acceptable under the external and internal reflections. In addition, the subpart of spectral resolution of the program also worked well for prediction with high accuracy and robustness. The program also employed to test with the simulated system of the three artificial components with free evaporation. The results of prediction agreed very well.

iii) In the actual experiments, the program was employed to resolve the time-dependent spectra of the mixture of acetone, methanol and toluene. The results agreed very well with the reference spectra and the characteristic peaks of each compound were perfectly matched. However, there are some deviations with the starting volume ratios of the three components that due to the problems of not real-time analysis, time

gap from solution preparation until the proper time of measurement and the delayed of the measuring time in order to avoid the over-absorption. Furthermore, the system of polymer crystallization of poly(3-hydroxybutyrate-*co*-3-hydroxyhexanoate) was also analyzed by the program. The results indicate that there are three major components. In such system, one component changed or transformed into the other two components. The three components are amorphous, less-order crystalline and high-order crystalline forms. The prediction agree with that evaluated by curve fitting and 2D correlation.[34]

iv) The applicability of the program depends on several factors such as the number of analyzed spectra, spectral resolution, degree of spectral overlapping between the components, signal-to-noise ratio of spectrum, baseline variation, the formation of unexpected species, and so on. The effect of these factors causes the error of calculations. For example in Section 4.2, when the level of random noise in simulated spectra was increased, the accuracy of the calculations was decreased.

REFERENCES

1. Griffiths, P. R., and de Haseth J. A. <u>Fourier transform infrared spectrometry</u>. New York: John Wiley & Sons, 1986.

2. Massart, D. L., Vandeginste, B. G. M., Buydens, L. M. C., de Jong, S., Lewi, P. J. and Smeyers-Verbeke, J. <u>Handbook of chemometrics and qualimetrics: Part A</u>. Netherlands: Elsevier Science B.V., 1997.

3. Malinowski, E. R. <u>Factor analysis in chemistry</u>. New York: John Wiley & Sons, 1991.

4. Ward, L. <u>The optical constants of bulk materials and films</u>. Philadelphia: Institute of Physics Publishing, 1994.

5. Mirabella, F. M. <u>Internal reflection spectroscopy</u>. New York: Marcel Dekker, 1992.

6. Urban, M. W. <u>Attenuated total reflectance spectroscopy of polymers</u>. Washington, DC: American Chemical Society, 1996.

7. Keefe, C. D. <u>Journal of Molecular Spectroscopy</u> 205 (2001): 261-268.

8. Ohta, K., and Ishida, H. <u>Applied Spectroscopy</u> 42 (1988): 952-957.

9. Huang, J. B., and Urban, M. W. <u>Applied Spectroscopy</u> 46 (1992): 1666-1672.

10. Churchill, R. V. <u>Complex variables and applications</u>. Tokyo: Tosho Printing, 1960.

11. Yamamoto, K., and Ishida, H. <u>Spectrochimica Acta</u> 50 (1994): 2079-2089.

12. Yamamoto, K., Masui, A., and Ishida, H. <u>Applied Optics</u> 33 (1994): 6285-6293.

13. Yamamoto, K., and Masui, A. <u>Applied Spectroscopy</u> 49 (1995): 639-644.

14. Bertie, J. E., and Lan, Z. <u>Journal of Chemical Physics</u> 103 (1995): 10152-10161.

15. Bertie, J. E., and Lan, Z. <u>Journal of Chemical Physics</u> 105 (1996): 8502-8514.

16. Brereton, R. G. <u>Chemometrics: Data analysis for the laboratory and chemical plant</u>. England: John Wiley & Sons, 2003.

17. Malinowski, E. R. <u>Journal of Chemometrics</u> 1 (1987): 33-40.

18. Malinowski, E. R. <u>Journal of Chemometrics</u> 3 (1988): 49-60.

19. Malinowski, E. R. <u>Analytical Chemistry</u> 49 (1977): 606-617.

20. Press, W. H., Teukolsky, S. A., Vetterling, W. T., and Flannery, B. P.
      <u>Numerical recipes in FORTRAN</u>. USA: Cambridge University
      Press, 1992.

21. Tauler, R., and Kowalski, B. <u>Analytical Chemistry</u> 65 (1993): 2040-2047.

22. Tauler, R., Smilde, A., and Kowalski, B. <u>Journal of Chemometrics</u>
      9 (1995): 31-58.

23. Gargallo, R., Tauler, R., Cuesta-Sanchez, F., and Massart, D. L.
      <u>Trends in Analytical Chemistry</u> 15 (1996): 279-286.

24. Mendieta, J., Diaz-Cruz, M. S., Esteban, M., and Tauler, R.
      <u>Biophysical Journal</u> 74 (1998): 2876-2888.

25. Sasic, S., Amari, T., Siesler, H. W., and Ozaki, Y. <u>Applied Spectroscopy</u>
      55 (2001): 1181-1191.

26. Leger, M. N., and Wentzell, P. D. <u>Chemometrics and Intelligent Laboratory</u>
      <u>Systems</u> 62 (2002): 171-188.

27. Ekgasit, S., and Siesler, H. W. <u>Applied Spectroscopy</u> 52 (1998), 367-374.

28. Harrick, N. J. <u>Internal reflection spectroscopy</u>. New York: Harrick Scientific
      Corporation, 1979.

29. Bertie, J. E., Zhang, S. L., and Keefe, C. D. <u>Journal of Molecular Structure</u>
      324 (1994): 157-176.

30. <u>MATLAB: High-performance computation and visualization software</u>.
      USA: MathWorks, Inc., 1992.

31. วุฒิชัย พาราสุข และ อรุณชัย ตั้งเจริญบำรุงสุข. <u>รายงานประกอบโปรแกรมวิเคราะห์</u>
      <u>ตัวประกอบสำหรับการประยุกต์ทางสเปกโทรเคมี</u>.
      กรุงเทพมหานคร: 2547.

32. Nishikawa, Y. <u>Applied Spectroscopy</u> 53 (1999): 1054-1060.

33. อัจฉรา เผดิมโชค. <u>การแปลงเฟสโดยเหนี่ยวนำด้วยความร้อนของโนแด็กซ์โคพอลิเมอร์</u>
      <u>ตรวจสอบโดยอินฟราเรดสเปกโทรสโกปีแบบสองมิติ</u>. วิทยานิพนธ์ปริญญา
      ดุษฎีบัณฑิต สาขาปิโตรเคมีและวิทยาศาสตร์พอลิเมอร์ คณะวิทยาศาสตร์
      จุฬาลงกรณ์มหาวิทยาลัย, 2547.

34. Yoshie, N., Oike, Y., Kasuya, K., Doi, Y., and Inoue, Y. Biomacromolecules
     3 (2002): 1320-1326.

35. Chalmers, J. M., and Griffiths, P. R. Handbook of vibrational spectroscopy:
     Volume 1. Italy: John Wiley & Sons, 2002.

36. Barrow, G. M. Physical chemistry. USA: McGraw-Hill, 1996.

37. Ekgasit, S., Thammacharoen, C., and Knoll, W. Analytical Chemistry
     76 (2004): 561-568.

APPENDICES

WizardIR version 1.0: Program Manual

Program `WizardIR` version 1.0 was developed to resolve the infrared spectra of multicomponent mixtures using the chemometric methods such as principal component analysis and multivariate curve resolution. The obtained results are the profiles of concentration (in term of volume fraction or normalized concentration) and absorptance coefficients (or absorptivity) of each component in the mixtures. The profiles of absorptance coefficient would be used to determine the optical constants (refractive index n and absorption index k) using Kramers-Kronig transformations and numerical optimization. The source codes were written in MATLAB v6.5 (MathWorks, Inc.). This compact manual provided step-by-step instruction and demonstration with an example of input and output in an easy understanding.

Running the Program

1) In MATLAB command window, execute the program by typing WizardIR_v1 as:

>> **WizardIR_v1**

After pressing the ENTER key, the program would clear the screen and start to run as the following:

```
*********************************************************************************
*  WizardIR v 1.0 – Chemometric Program for Infrared Spectroscopic Analysis  *
*  Created by Arunchai Tangcharoenbumrungsuk                                 *
*  Conducted by Dr. Sanong Ekgasit and Dr. Vudhichai Parasuk                 *
*********************************************************************************
```

2) Begin to input the spectra filename such as:

```
Input Elementary Data:
        -   Please type the spectra filename: AMT_mixture.txt
```

The format of the spectra file would be an ASCII format which created by a text editor such as Notepad, Microsoft Editor or Microsoft Excel programs. The structure of the file is correspondent to the spectra matrix which each row associated to the ith wavenumber, and each column associated to the jth mixture except for the first column stands for the column of wavenumber. The example of spectra file was shown below.

4000	0.013	0.013	0.012	0.013	0.012	0.013	0.014	0.015	0.013
3996	0.012	0.013	0.012	0.013	0.012	0.014	0.015	0.016	0.014
3992	0.012	0.013	0.012	0.014	0.016	0.019	0.021	0.023	0.021
3988	0.012	0.013	0.013	0.015	0.018	0.023	0.025	0.028	0.027
3984	0.012	0.013	0.014	0.018	0.024	0.032	0.035	0.039	0.038
3980	0.012	0.015	0.017	0.025	0.036	0.050	0.054	0.060	0.060

………………………………………………………………………………………………

………………………………………………………………………………………………

After complete loading the file, the program would display the dimension of spectra matrix as shown below.

- Please type the spectra filename: **AMT_mixture.txt**
  Dimension of the spectra matrix = **1687 x 38**
  Number of solution = **38**

      3) Specify the range of monitoring time. Here there are two possible ways. The first is to specify with an equally step time as shown below.

- Specify the range of monitoring time: **0:5:100**

The input '0:5:100' means that starting at 0 unit time and stopping at 100 unit time with equal time interval of 5 unit time. The second choice is to specify with a series of typical values as shown below.

- Specify the range of monitoring time: **[0 5.1 10.2 14.9 20.1 25.2]**

At this stage, the program would plot the spectra that loaded from the input file as two and three dimensions.

4) The program would automatically perform the principal component analysis (PCA) and error analysis. The results of this stage are shown in the following example. In the later the user should assign the number of primary eigenvectors by accepting the number of program suggestion or another as request.

- Principal component analysis:
  Number of Eigenvector = 38
  Eigenvalues:
    11.874195
    0.675174
    0.018828
    0.000229
    0.000024
    0.000021
    0.000020
    0.000019

- Error analysis:

n	Eigenvalue	RSD	RMS	IE	IND	%SL
1	11.874198	1.697E-02	1.630E-02	4.706E-03	1.178E-04	3.539E-05
2	0.675174	2.948E-03	2.712E-03	1.156E-03	2.436E-05	2.836E-06
3	0.018828	4.377E-04	3.839E-04	2.103E-04	4.377E-06	2.587E-06
4	0.000229	2.934E-04	2.441E-04	1.628E-04	3.623E-06	3.12
5	0.000024	2.861E-04	2.244E-04	1.774E-04	4.470E-06	42.0
6	0.000021	2.803E-04	2.057E-04	1.904E-04	5.720E-06	44.4
7	0.000020	2.738E-04	1.860E-04	2.009E-04	7.604E-06	44.8
8	0.000019	2.670E-04	1.656E-04	2.095E-04	1.068E-05	45.8

- By computation, the estimated number of primary eigenvector = 4

Note: If the estimation = 0, it means that the data matrix may consist of unsufficient data or contain only pure error. The data, therefore, are not factor analyzable.

- Do you agree with this estimation?
  If "yes", please prees <y>.
  if "no", please input your estimation: **Y**

5) Choose an option for setting the initial guess for the process of Multivariate Curve Resolution (MCR). Here the automatic setting is recommended.

> - Please select the option for setting the initial guess for MCR
>   (1) Automatic setting
>   (2) Manual setting
>   Enter the selection **1**

6) Assign the convergence criteria for the process of MCR as shown in the following example. However, the user also has another choice to use the default values of the program: maximum cycle = 100 and tolerance = $1x10^{-8}$.

> - In the process of MCR, do you want to set the convergence criteria?
>   If "yes", please input the values.
>   If "no", please press <ENTER> to use the default values:

At this stage, the program would perform the MCR, and the user should wait until finishing of the process. Then the program would plot the estimated profiles of concentration in term of volume fraction and absorptance coefficient.

7) Input the experimental parameters: refractive index of incident media, angle of incidence (in the unit of degree) and polarization of the light as shown below.

> - Please input the experimental parameters:
>   Refractive index of incident media = **2.4**
>   Angle of incidence (in the unit of degree) = **45**
>   Polarization of the light = **'s'**

8) Assign the convergence criteria for the process of optical constants determination as shown in the following example. However, the user also has another choice to use the default values of the program: maximum cycle = 20 and tolerance = $1x10^{-8}$.

> - In the process of optical constants determination, do you want to set the convergence criteria?
>   If "yes", please input the values.
>   If "no", please press <ENTER> to use the default values:

At this stage, the program would calculate the optical constants of each component in the mixtures, then the user should wait until the process is complete. After finishing the process, the program would plot the estimated spectra of refractive index and absorption index of each component.

9) Select an option for saving the results as the following below.

Results:

- Do you want to save the results to the disk?
  If "yes", please input the filenames.
  If "no", please press <ENTER>.

Resonance Shifts in SPR Curves of Nonabsorbing, Weakly Absorbing, and Strongly Absorbing Dielectrics

Sanong Ekgasit,[a,b,*] Arunchai Tangcharoenbumrungsuk,[a] Fang Yu,[b]

Akira Baba,[b,c] and Wolfgang Knoll [b]

[a] Sensor Research Unit, Department of Chemistry, Faculty of Science, Chulalongkorn University, Bangkok 10330, Thailand

[b] Max-Planck-Institut für Polymerforschung, Ackermannweg 10, D-55128 Mainz, Germany

[c] Current address: Department of Chemistry, University of Houston, 136 Fleming Building, Houston, TX 77204-5003, USA.

ABSTRACT

The resonance shifts (i.e., the resonance angle and the reflectance minimum) in SPR curves due to the complex refractive index and/or thickness variations of dielectric films were investigated. For both, nonabsorbing and absorbing dielectrics, the resonance angle shifts linearly with the refractive index and/or thickness variations. The reflectance minimum of the nonabsorbing dielectric does not change as the resonance angle shifts. For an absorbing dielectric, the direction of the reflectance change depends strongly on the magnitude of the absorption and thickness of the metal film. The reflectance minimum of the sensor with a thin metal film decreases before increasing while that of the sensor with a thick metal film continuously increases as the absorption of the dielectric film increases. The phenomena were theoretically explained based on the SPR-generated evanescent field at the metal/dielectric interface associated with the optical properties of the sensor architecture.

[*] To whom correspondence should be addressed: sanong.e@chula.ac.th

INTRODUCTION

Surface plasmon resonance (SPR) spectroscopy is a surface sensitive characterization technique that takes advantage of the resonance coupling between the exciting radiation and the surface plasmon wave propagates along the surface of a thin noble metal film for probing changes near the metal surface. The resonance coupling of the incident light and the surface plasmon wave can be tailored for specific applications by altering the structure of the metal film or the environment in the vicinity of the metal surface.[1-4] Due to its highly sensitive nature of the surface plasmon wave towards the optical properties of the dielectric media near the metal surface, SPR sensor becomes a powerful affinity biosensor for monitoring interactions at the interface (i.e., enzyme-substrate, antigen-antibody, receptor-ligand, and drug-protein interactions) or physicochemical phenomena near the metal surface (i.e., chemical reactions, absorption, degradation, swelling, protein hybridizations, and self-assembling). The sensitive nature of the SPR sensor is derived from the unique characteristic of the surface-plasmon-resonance (SPR)-generated evanescent field at the metal/dielectric interface under the total internal reflection condition. The field is very strong at the metal/dielectric interface due to the resonance coupling. The strong SPR-generated evanescent field decays exponentially as a function of distance into the metal film and the dielectric medium. The rapid decay of the evanescent field makes SPR sensor very sensitive to changes of the optical constant

and/or thickness of the dielectric film attached to the metal film. This change can be observed via the shift of the resonance angle of the SPR curve.[2-7]

The physicochemical phenomena at the metal surface, especially those associated with binding or interaction of biomolecules at the interface, involve mass accumulation on the sensor surface, which induces refractive index and/or thickness variation of the dielectric film. By employing a functionalized dielectric film, specific interaction on the sensor surface can be monitored. The molecular structure-biological function and/or structure-property relationship of the molecules associated with the interaction can be studied. The linear relationship between the SPR signal and the refractive index and/or thickness changes enables SPR for quantitative analysis of the interaction. [2-7]

Although SPR sensor has been traditionally employed for monitoring physicochemical phenomena associated with nonabsorbing dielectrics, its sensitivity improvement by absorbing dielectrics has recently gained substantial attentions.[8-21] For a nonabsorbing dielectric film, the resonance angle shifts linearly with the refractive index and/or thickness changes without a significant change of the reflectance minimum. The progress of the interaction at the sensor surface can be derived from the linear shift of the resonance angle or the reflectance change monitored at an angle slightly lower than the resonance angle.[2-4] In the SPR sensitivity improvement scheme via the absorbing dielectric, the combination of resonance angle shift due to refractive index and/or thickness changes and reflectance change due to the additional absorption makes SPR sensor very sensitive when it is used for monitoring the physicochemical phenomena associated with absorbing dielectrics. Gold and silver nanoparticles and gold colloid have been employed for sensitivity enhancement of SPR-based biosensor.[8-13] The enhancement

techniques take advantage of the reflectance change due to the high absorption index of the additionally bound nanoparticles. Based on the specific binding scheme, the additionally bound gold nanoparticles enhance the detection limit of binding events, especially those of small molecules such as DNA fragments. In general, the binding of small molecules induces insignificant changes in the SPR curve due to the extremely small refractive index and/or thickness variation.[21-22] The reflectance minimum change due to absorption at a low concentration of bulk dielectric has been employed as a sensitive detection scheme for enzyme-based SPR sensor.[15] The strong SPR-generated evanescent field has also been employed for excitation of the surface-confined fluorophore near the metal surface in surface-plasmon field-enhanced fluorescence spectroscopy.[17-21]

This paper will show that various unique characteristics and sensitive nature of the SPR technique are governed by the SPR-generated evanescent field at the metal/dielectric interface. The changes of SPR curve associated with complex refractive index and/or thickness variations of the nonabsorbing dielectrics, weakly absorbing dielectric, and strongly absorbing dielectrics are theoretically explained via the SPR-generated evanescent field.

THEORY

For an SPR setup in the Kretschmann-Raether ATR configuration, reflectance depends strongly on the experimental conditions (i.e., polarization, angle of incidence, and wavelength of the coupled radiation) and material characteristics (i.e., the complex refractive indices of the metal films, the dielectric films and the dielectric substrate, and

the thickness of the metal and the dielectric films). Under the total internal reflection condition, the reflectance $R(\theta)$ of the coupled radiation with parallel polarization can be expressed in terms of the evanescent field amplitude and optical properties of the materials by the following expression:[23,24]

$$R(\theta) = 1 - A(\theta) = 1 - \left(\frac{2\pi}{\lambda}\right)^2 \frac{1}{k_{zP}(\theta)} \sum_{j=1}^{N} \left[\int_{z_j}^{z_{j+1}} \text{Im}\left[\hat{\varepsilon}_j\right] \left\langle E_z^2(\theta)\right\rangle dz\right] \qquad (1)$$

where θ is the angle of incidence, $A(\theta)$ is the absorption in *absorptance unit*, λ is the wavelength of the coupled radiation, $\hat{\varepsilon}_j$ is the complex dielectric constant of the jth layer, and $\left\langle E_z^2(\theta)\right\rangle$ is the mean square evanescent electric field at a distance z from the prism/metal interface. N is the number of the dielectric film in the sensor architecture with the metal film as the first layer. $k_{zP}(\theta)$ is the z-component of the wavevector in the prism. $k_{zP}(\theta)$ can be expressed in terms of the x-component of the wavevector $k_{xP}(\theta)$ by

$$k_{zP}(\theta) = \left[(2\pi/\lambda)^2 \varepsilon_P - k_{xP}^2(\theta)\right]^{1/2} \quad \text{with} \quad k_{xP}(\theta) = (2\pi/\lambda)\left[\varepsilon_P \sin^2\theta\right]^{1/2} \quad \text{and} \quad \varepsilon_P \text{ is the}$$

dielectric constant of the prism. The complex dielectric constant is related to the complex refractive index by $\hat{\varepsilon} = \hat{n}^2 = (n + ik)^2$; where n and k, respectively, are refractive index and absorption index. The detailed derivations of the electric field and the SPR-reflectance based on the surface-plasmon-wave-generated evanescent field are given elsewhere.[23-25]

For SPR of a nonabsorbing dielectric, the metal film is the only absorbing medium in the sensor architecture. The reflectance can be expressed in terms of the evanescent field within the metal film and the optical property of the metal film by:[23,24]

$$R(\theta) = 1 - \left(\frac{2\pi}{\lambda}\right)^2 \frac{1}{k_{zP}(\theta)} \int_0^{d_M} \mathrm{Im}[\hat{\varepsilon}_M] \langle E_z^2(\theta) \rangle dz \qquad (2)$$

where d_M and $\hat{\varepsilon}_M$, respectively, are thickness and complex dielectric constant of the

metal film. Although the nonabsorbing dielectric does not contribute to the reflection loss

in the SPR curve, its refractive index and thickness govern the resonance condition of the

SPR curve. The resonance angle shifts to a greater value without a significant change in

the reflectance minimum as the thickness and/or refractive index of the nonabsorbing

dielectric film increase.

   The SPR curve of an absorbing dielectric is characterized by a broader curve shape

together with a greater reflectance minimum compared to that of the nonabsorbing

dielectric. This is due to the presence of an additional absorbing media in the sensor

architecture. When an absorbing dielectric presents in the system, smaller evanescent

field amplitude at the metal/dielectric interface compared to that of the nonabsorbing

dielectric is observed. The reflectance with absorbing dielectrics can be expressed in

terms of the evanescent field by: [24]

$$R(\theta) = 1 - \left(\frac{2\pi}{\lambda}\right)^2 \frac{1}{k_{zP}(\theta)} \left\{ \int_0^{d_M} \mathrm{Im}[\hat{\varepsilon}_M] \langle E_z^2(\theta) \rangle dz + \sum_{l=1}^{L} \left[\int_{d_D} \mathrm{Im}[\hat{\varepsilon}_D] \langle E_z^2(\theta) \rangle dz \right] \right\} \qquad (3)$$

where d_D and $\hat{\varepsilon}_D$, respectively, are thickness and complex dielectric constant of the

absorbing dielectric film, L is the number of absorbing dielectric films while $\int_{d_D}$ indicates

integration over the thickness of the film.

EXPERIMENTAL SECTION

SPR Setup

A schematic illustration of an SPR setup is shown in Figure 1. A radiation from a HeNe laser (632.8 or 1152 nm) was modulated by a chopper. The plane of polarization and intensity of the modulated radiation were controlled by two polarizers. The radiation was coupled to the systems via a right-angled prism (LaSFN9 or BK7). The reflected beam was then focused onto a photodiode detector. The SPR signals were collected as a function of the measured incidence angle θ_e defined with respect to the direction normal to the prism/metal interface. The measured incidence angle θ_e is slightly different from the incident angle θ at the prism/metal interface due to the refraction at the air/prism interface. For direct comparisons with the experimental results, the simulated results were expressed in terms of the measured incidence angle θ_e while the calculated reflectance was corrected for the reflection at the prism surfaces.

Sensor Fabrications

Glass wafers (LaSFN9 or BK7) were cleaned and coated with a ~50 nm gold film via a commercial thermal evaporation instrument (Edwards FL400, England) at a deposition rate of 0.1 nm/s under UHV condition (5×10^{-6} mbar). The BK7 wafers were pre-coated with ~1 nm chromium adhesion promoter layer prior to the coating of gold film. Freshly gold-coated wafers were employed for all experiments.

Antibody binding experiment (SPR of nonabsorbing and weakly absorbing dielectrics): The self-assembled monolayer (SAM) was fabricated by immersing the gold-coated LaSFN9 wafers in the thiol solutions over night at room temperature. Ethanol solutions of mixed thiols (OH-terminated thiol and biotin-terminated thiol with a

net thiol concentration of 500 μM) with mole fractions of the biotin-terminated thiol χ of 0.1 and 0.04 were employed. After the SAM fabrication, the substrates were rinsed thoroughly with absolute ethanol, blown-dry with dry nitrogen, and kept under argon environment until being used. The experiments were performed by injecting an aliquot of 1 mL fluorophore-labeled antibody AF-2F5 (Alexa Fluor 647-labeled mouse monoclonal antibody 2F5 (isotype IgG$_{1,k}$) with dye-to-protein ratio of 4.4, Molecular Probes) into the flow cell. The solution was left in the flow cell for 15 minutes in order to allow the complete binding of the antibody onto the surface of SAM. The sensors were regenerated by flow washing the antibody-bound SAM with a sodium dodecyl sulfate solution (5mg/mL in HBS-EP). Once the regeneration is completed (i.e., no additional change in the observed SPR curve after prolonged washing), a binding with a non-labeled antibody 2F5 was performed. After the binding of the non-labeled antibody, the final binding with fluorophore-labeled antibody AF-RaM (Alexa Fluor 647-labeled rabbit anti-mouse IgG with dye-to-protein ratio of 4.8, Molecular Probes) was then carried out. All experiments were performed at room temperature (21 $\pm$ 2 ^{o}C) with HBS-EP buffer solution (degassed 10 mM HEPES-buffered saline, pH 7.4, 150 mM NaCl, 3 mM EDTA with 0.005% (v/v) surfactant P-20, Biacore, Sweden). An equal working concentration of 20 nM was employed for the fluorophore-labeled antibody AF-2F5 and the non-labeled antibody 2F5 while a concentration of 33 nM was employed for the fluorophore-labeled antibody AF-RaM. In order to avoid bulk solution effect, the cell was flow-washed and filled with running buffer before an SPR acquisition. The SPR curves of the step-by-step binding events are shown in Figure 2.

Self-assembled conducting polymer experiment (SPR of a strongly absorbing dielectric with thickness variation): The gold-coated BK7 wafer was functionalized by immersing in the solution of 3-mercapto-1-propanesulfonic acid, sodium salt (0.001 M in ethanol). The uniform and negatively charged substrate was immersed in a dilute HCl solution prior to the self-assembled fabrications. The substrates were alternatively immersed, for 15 minutes, in aqueous solution of the polycation and the polyanion until the desired numbers of self-assembled layers were achieved (i.e., 2, 4, and 6 layers).[26] The fabricated wafer was rinsed thoroughly with deionized water (Milli-Q, 18 MΩ, pH 5.6) between the successive depositions. Structures of the polyelectrolyte are shown in Figure 1. Polyaniline (PANI) and sulfonated polyaniline (SPANI) were synthesized following the procedures given by MacDiarmid et al.[27] and Yue et. al.,[28] respectively. Poly(allylamine hydrochloride) (PAH, MW 50000–65000) and poly(sodium 4-styrenesulfonate) (PSS, MW 70000) were purchased from Aldrich. The synthesized emeraldine hydrochloride was converted to emeraldine base by reacting with ammonium hydroxide for 24 h. The polymer can be made water soluble according to a procedure given by Cheung et. al.[29] A dilute solution of the polymer (20 mg/mL in dimethylacetamide) was subsequently diluted (1:10) in water (pH 3.0–3.3). The pH of the aqueous solution was then adjusted to approximately pH 2.6. Sulfonation of PANI was performed by reacting with fuming sulfuric acid and isolating the product, which is soluble in 0.1 M sodium hydroxide. The pH of the SPANI solution was adjusted to approximately pH 3.0 prior to self-assembled fabrication.[30] The SPR curves of the multilayer PANI/SPANI films under ambient air environment are shown in Figure 3.

PEDOT film under applied potential experiment (SPR of strongly absorbing dielectrics with complex refractive index variation): The ultra thin PEDOT, poly(3,4-ethylenedioxythiophene), film was electropolymerized from a 0.01 M of EDOT monomer (3,4-ethylenedioxythiophene) in acetonitrile with 0.1 M TBAPF6 (tetrabutylammonium hexafluorophosphate) on the surface of a gold-coated LaSFN9 wafer at an applied potential of 0.9 V for 30 s.[31] A conventional three-electrode cell was employed (i.e., the gold-coated LaSFN9 working electrode, a platinum wire counter electrode, and an Ag/Ag$^+$ non-aqueous reference electrode). The ultra thin PEDOT film was then subjected to different applied potentials via a potentiostat (Princeton Applied Research 263A, EG&G) under a monomer-free solution of 0.1 M TBAPF6 in acetonitrile. The SPR curves with the coupled wavelengths of 632.8 and 1152 nm were acquired after applying a desired potential for 2.5 min. The SPR curves of the ultra thin PEDOT film with the applied potentials of 0.5, -0.2, -0.65, and –1.0 V are shown in Figure 4.

RESULTS

The SPR curves of nonabsorbing and weakly absorbing dielectrics with mole fractions of the biotin-terminated thiol χ of 0.10 and 0.04 are shown in Figures 2A and 2B, respectively. The broad SPR curve in Figure 2A(a) compared to that in Figure 2B(a) indicates a thinner gold film. When a weakly absorbing dielectric, the fluorophore-labeled antibody AF-2F5, was bound onto the surface of SAM with $\chi = 0.10$, the resonance angle shifted to a greater angle while the reflectance minimum slightly decreased, Figure 2A(b). The SPR curve retreated back and almost superimposed with that of the virgin SAM when the fluorophore-labeled antibody was removed by the

regeneration process, Figure 2A(c). When a nonabsorbing dielectric, the non-labeled antibody 2F5, was bound onto the regenerated surface, the resonance angle shifted to a greater angle without a significant change of the reflectance minimum, Figure 2A(d). The magnitude of the shift is slightly greater than that of the fluorophore-labeled antibody. When the fluorophore-labeled antibody AF-RaM was additionally bound onto the sensor, the resonance angle shifted further with a slight decrease of the reflectance minimum, Figure 2A(d).

Similar resonance angle shifts were observed when the same binding events were performed on the sensor with $\chi = 0.04$, Figure 2B. The change in the reflectance minimum was not observed after the binding of the non-labeled antibody, Figure 2B(d). However, the increments of the reflectance minimum were detected after the binding of the fluorophore-labeled antibodies, Figures 2B(b) and 2B(e).

For SPR of a strongly absorbing dielectric, the influences of the absorption via thickness increment were clearly observed in the SPR curves of the self-assembled PANI/SPANI conducting polymer film, Figure 3. The resonance angle shifted to a greater value, the reflectance minimum increased, the SPR curve became broader while the resonance angle and the critical angle were less obvious as the number of layers of the self-assembled PANI/SPANI film increased. The largest reflectance increment was observed when the first layer of PANI/SPANI film was fabricated onto the gold surface. Smaller increments were detected with the successive self-assembled layers.

The influence of the absorption by the complex refractive index variations was examined via the SPR curves of PEDOT conducting polymer films under various applied potentials, Figure 4. The SPR curve of the bare gold with 0.1 M TABPF6 solution at the

coupled wavelength of 1152 nm, Figure 4B, was narrower than that with the coupled wavelength of 632.8 nm. At the coupled wavelength of 632.8 nm, Figure 4A, the resonance angle and the reflectance minimum of the SPR curve with the 0.5 V applied potential were smaller than those with negatively applied potentials. When the film was subjected to a negatively applied potential (i.e., -0.2, -0.65, and -1.0 V), the reflectance minimum increased while the resonance angle shifted to greater value and became less obvious.

With the same potentials applied on the exact same PEDOT film, opposite phenomena were observed with the coupled wavelength of 1152 nm. The broadest SPR curve with the highest reflectance minimum and the smallest resonance angle was observed at the 0.5 V applied potential. The resonance angle shifted to a greater value while the reflectance minimum decreased as the film was subjected to a greater negatively applied potential (i.e., -0.2, -0.65 and -1.0 V, respectively)

In order to determine the layer architectures and to gain insight understandings of the investigated systems, the observed SPR curves were fitted by Fresnel equation. The fitted parameters are shown in Tables 1 – 3.

DISCUSSION

For binding events of nonabsorbing dielectrics, the resonance angle increases without a significant change of the reflectance minimum (i.e., Figure 2A(c) to 2A(d) and Figure 2B (c) to 2B(d)). This phenomenon associates with the evanescent field in the metal film. The evanescent field at the resonance angle does not change significantly as it shifts to a greater angle by the deposition of a nonabsorbing dielectric. Figure 5A shows the

resonance shift (i.e., the resonance angle and the reflectance minimum) of the SPR curve induced by thickness and refractive index increments. The resonance angle shifts linearly with thickness and refractive index of the nonabsorbing film. The reflectance minimum, however, stays unchanged. Since the metal film is the only absorbing medium in the SPR of the nonabsorbing dielectrics, the attenuation of the reflectance can be assigned to the absorption of the metal.[23,24] According to Eq. (2), the reflectance is proportional to the integration of the product between the evanescent field amplitude and the imaginary part of the dielectric constant of the metal film, the evanescent field integration must be constant or insignificantly changed as the resonance angle shifts. Figure 5B shows the evanescent field decay profile at three different resonance conditions defined in Figure 5A. Although their resonance angles are different, the corresponding evanescent field decay profiles within the metal film are almost the same. The same magnitudes of the evanescent field integrations make their reflectance minimums almost the same (i.e., cannot be differentiated experimentally, see Figure 5A).

SPR of an absorbing dielectric is more complicated than that of the nonabsorbing dielectric due to the presence of an additional absorbing medium. The resonance angle shifts to a greater angle due to the thickness and/or refractive index increment. The reflectance minimum also changes while the SPR curve becomes broader as the absorption of the absorbing dielectric increases. The direction of the reflectance change (i.e., increasing or decreasing) depends strongly on the thickness of the metal film. For a weakly absorbing dielectric, if the thickness of the metal film is smaller than the optimal thickness, the reflectance minimum decreases as the absorption of the dielectric film

increases (see Figure 2A). The opposite phenomenon is observed when the thickness of the metal film is greater than the optimal thickness (see Figure 2B).

The optimal thickness of the metal film in SPR measurement depends strongly on the wavelength of the coupled radiation and optical constants of the metal film and the dielectric medium. As shown in Figure 6, the optimal thickness of the gold film decreases as the absorption of the dielectric film increases. For a weakly absorbing thin dielectric film, the optimal gold thickness can be estimated from that of the nonabsorbing dielectric since their evanescent field profiles are not significantly different. Based on the complex dielectric constant from Fresnel fitting, the optimal thickness of the gold film in Figure 2A is 45.56 nm while that in Figure 2B is 45.40 nm. The calculated optimal thickness, thus, confirms that the gold film in Figure 2A is thinner than optimal thickness.

The evanescent field decay profiles at the resonance angles of the SPR curves in Figure 2 are shown in Figure 7. The weaker evanescent field of the absorbing dielectric film makes the absorption of the gold film smaller compared to that of the nonabsorbing dielectric. For the system with a thin gold film, Figure 2A, the decreased absorption of gold film can be compensated by the absorption of the fluorophore-labeled antibody. The summation of the absorption of the gold film and that of the fluorophore-labeled antibody (i.e., Figures 2A(b) and 2A(e)) is greater than that of the gold film with unbound SAM or with non-labeled antibody (i.e., Figures 2A(a), 2A(c), and 2A(d)). As a result, according to Eq. (3), smaller reflectance minimums in SPR curves of absorbing dielectric compared to that of the nonabsorbing dielectric are observed. If the absorption of the dielectric film is greatly increased, the evanescent field is significantly decreased. The absorption of the dielectric will not compensate the decreased absorption of the metal film, thus, a greater

reflectance minimum compared to that of the nonabsorbing dielectric will be observed. The opposite phenomena are observed in the system with a thick gold film. As shown in Figure 7, the evanescent field is significantly decreased as the dielectric film becomes absorbing. The absorption of the dielectric film cannot compensate the decreased absorption of gold, thus, a greater reflectance is observed (Figures 2B(b) and 2B(e)).

The changes associated with the increased absorption of the dielectric film via the thickness increment, as summarized in Figure 8, include: the resonance angle linearly shifts to a greater value, the evanescent field at the metal/dielectric interface decreases, the absorption of the metal film decreases while the absorption of the absorbing dielectric increases. However, the change of the reflectance minimum depends strongly on the thickness of the gold film. For a sensor with a gold film thinner than the optimal thickness, Figure 8A, the reflectance minimum decreases to a minimal value (almost zero) before continuously increasing as the thickness of the dielectric film increases. This is due to the associated absorptions of the gold film and the absorbing dielectric film. The absorption of a thin dielectric film (i.e., less than 20 nm in this case) is greater than the decreased absorption of the metal film. Thus, the total absorption increases with the thickness of the dielectric film. The high absorption of the dielectric film is due to the strong evanescent field at the metal/dielectric interface. Although the absorption index and thickness of the dielectric film are much smaller than those of the metal film, the evanescent field in the dielectric medium is much greater than that in the metal film. According to the employed sensor architecture, the evanescent field at the metal/dielectric interface on the dielectric side is 30 times greater than that of the coupled radiation. The evanescent field at the metal/dielectric interface on the metal side, on the

other hand, is only 6 times greater (see Figure 8). As the thickness of the absorbing dielectric film is further increased, the SPR-generated evanescent field is further decreased. Although the absorption of the dielectric film increases, the increased absorption cannot compensate the decreased absorption of the metal film. As a result, the total absorption decreases as the thickness of the metal film increases. According to Eq. (3), this results in a greater reflectance minimum compared to that of the nonabsorbing dielectric film.

For a sensor with a thick gold film, Figure 8B, the reflectance minimum increases with the thickness of the absorbing dielectric film. The evanescent field decreases as the absorption of the dielectric film increases. The absorption of the metal film, then, decreases due to the weaker evanescent field. Although the absorption of the dielectric film increases with the thickness of the dielectric film, the increased absorption cannot compensate the decreased absorption of the metal film. As a result, the reflectance minimum of the absorbing dielectric is greater than that of the nonabsorbing dielectric.

The broader SPR curve with high reflectance minimum in the SPR curve of a strongly absorbing self-assembled PANI/SPANI film is due to the substantially weak evanescent field associated with the absorption of the dielectric. The increased absorption of the dielectric film due to thickness increment cannot compensate the decreased absorption of the metal film. As shown in Figure 9, a large decrement of the evanescent field is observed at the first deposition of the self-assembled PANI/SPANI while smaller decrements are observed in the consecutive depositions. As a result, the largest reflectance change is observed upon the deposition of the first layer. Beside the decreased evanescent field amplitude at the metal/dielectric interface, the difference between the

absorption maximum of the metal film and that of the dielectric is a contributing factor to the broadening of the SPR curve.[23]

When the physicochemical phenomenon induces a significant change in the complex refractive index of the dielectric film attached to the gold surface, the corresponding SPR curve changes substantially. The refractive index and/or thickness variation shifts the resonance angle while the absorption index change alters the minimum reflectance. The smaller resonance angle in Figures 4A(a) and 4B(a) compared to that of the bare gold implies that the refractive index of the PEDOT film with 0.5 V applied potential is smaller than that of the ambient solution (0.1 M TBAPF6 in acetonitrile). Although the thickness variations of the PEDOT film in Figure 4 were very small, as confirmed by the quartz crystal microbalance (QCM) measurement,[31] substantial SPR curve variations caused by the complex refractive index changes were clearly observed. The thickness changes of the conducting polymer films upon applied potential were also reported elsewhere.[32,33] The greater reflectance minimums and the broader SPR curves compared to that of the bare gold film indicate absorptions of the PEDOT film at the coupled wavelengths. The broad SPR curve of bare gold in Figure 4A(Au) indicates that the 40 nm gold thickness is smaller than the optimal value at 632.8 nm excitation wavelength. According to the dielectric constant of the gold film obtained from the Fresnel fitting, the optimal gold thickness equals 45.48 nm. The above statement is confirmed by the SPR curve with 0.5 V applied potential where the reflectance minimum is smaller than that of the bare gold film. Although the film is weakly absorbing at 0.5 V applied potential, it becomes highly absorbing under the negatively applied potentials. Thus, the reflectance

minimum becomes greater than that of the bare gold film as the absorption increases. The observation in Figure 4A confirms the prediction shown in Figure 8A.

According to the results from Fresnel fitting, the optimal thickness of the gold film at 1152 nm is 40.48 nm. Despite the slightly smaller film thickness compared to the optimal thickness, the greater absorption index of the gold at 1152 nm makes the SPR curves narrower than that at 632.8 nm. The SPR curve at 0.5 V applied potential indicates that the PEDOT film is strongly absorbing at 1152 nm. In contrast to those at 632.8 nm, PEDOT film becomes less absorbing under the negatively applied potential. The phenomenon predicted in Figure 8A is not observed in Figure 4B due to the strong absorption of the PEDOT film and a slightly smaller thickness of the gold film compared to the optimal thickness at the coupled wavelength of 1152 nm.

CONCLUSIONS

The resonance condition of an SPR curve is greatly influenced by the experimental parameters and optical properties of the materials involving in the sensing scheme. The physicochemical phenomena induce changes in the optical properties of the dielectric film attached to the metal film thus shift the resonance condition. The resonance angle shifts linearly with the refractive index and/or thickness variations. The reflectance minimum change, on the other hand, depends strongly on the absorption of the dielectric film and thickness of the metal film. For a nonabsorbing dielectric, the resonance angle shifts without a significant change in the reflectance minimum. For a sensor with a thin metal film, the reflectance minimum decreases before continuously increases as the absorption of the dielectric film increases. The reflectance minimum of the sensor with a

thick metal film, on the other hand, continuously increases as the absorption of the absorbing dielectric increases.

ACKNOWLEDGMENTS

REFERENCES

[1]   W. L. Barns, A. Dereux, T. W. Ebbesen, Surface plasmon subwavelength optics, Nature 424 (2003) 824-830.

[2]   W. Knoll, Interfaces and thin films as seen by bound electromagnetic waves, Annu. Rev. Phys. Chem. 49 (1998) 569-638.

[3]   J. Homola, S. S. Yee, G. Gauglitz, Surface plasmon resonance sensors: Review, Sen. Actuators B, Chem. 54 (1999) 3-15.

[4]   Z. Salamon, H. A. Macleod, G. Tollin, Surface plasmon resonance spectroscopy as a tool for investigating the biochemical and biophysical properties of membrane protein systems .1. Theoretical principles, Biochim. Biophy. Acta 1331 (1997) 117-129.

[5]   J. Homola, Present and future of surface plasmon resonance biosensors, Anal. Bioanal. Chem. 377 (2003) 528-539.

[6]   R. J. Green, R. A. Frazier, K. M. Shakesheff, M. C. Davies, C. J. Roberts, S. J. B. Tendler, Surface plasmon resonance analysis of dynamic biological interactions with biomaterials, Biomaterials, 21 (2000) 1823-1835.

[7]   M. A. Cooper, Label-free screening of bio-molecular interactions, Anal. Bioanal. Chem. 377 (2003) 834-842.

[8]   L. A. Lyon, D. J. Peña, M. J. Natan, Surface plasmon resonance of Au colloid-modified au films: particle size dependence, J. Phys. Chem. B. 103 (1999) 5826-5831.

[9]   E. Hutter, J. H. Fendler, D. Roy, Surface plasmon resonance studies of gold and silver nanoparticles linked to gold and silver substrates by 2-aminoethanethiol and 1,6-hexanedithiol, J. Phys. Chem. B 105 (2001) 11159-11168.

[10]   T. Okamoto, I. Yamaguchi, Optical absorption study of the surface plasmon resonance in gold nanoparticles immobilized onto a gold substrate by self-assembly technique, J. Phys. Chem. B. 107 (2003) 10321-10324.

[11]   L. He, M. D. Musick, S. R. Nicewarner, F. G. Salinas, S. J. Benkovic, M. J. Natan, C. D. Keating, Colloidal Au-enhanced surface plasmon resonance for ultrasensitive detection of DNA hybridization, J. Am. Chem. Soc. 122 (2000) 9071-9077.

[12]   W. Fritzsche, T. A. Taton, Metal nanoparticles as labels for heterogeneous, chip-based DNA detection, Nanotechnology 14 (2003) R63-R73.

[13] T. Liu, J. Tang, L. Jiang, The enhancement effect of gold nanoparticles as a surface modifier on DNA sensor sensitivity, Biochem. Biophys. Res. Commun. 313 (2004) 3-7.

[14]   A. Hanning, J. Roeraade, J. J. Delrow, R. C. Jorgenson, Enhanced sensitivity of wavelength modulated surface plasmon resonance devices using dispersion from a dye solution, Sens. Actuators, B 54 (1999) 25-36.

[15]   K. Kurihara, K. Nakamura, E. Hirayama, K. Suzuki, An absorption-based surface plasmon resonance sensor applied to sodium ion sensing based on an ion-selective optode membrane, Anal. Chem. 74 (2002) 6323-6333.

[16] T. Wakamatsu, T. Nakano, K Shinbo, K. Kata, F. Kaneko, Detection of surface-plasmon evanescent fields using a metallic probe tip covered with fluorescence, Rev. Sci. Instrum. 70 (1999) 3962-3966.

[17] T. Liebermann, W. Knoll, P. Sluka, R. Herrmann, Complement hybridization from solution to surface-attached probe-oligonucleotides observed by surface-plasmon field-enhanced fluorescence spectroscopy, Colloids Surf. A 169 (2000) 337-350.

[18] T. Liebermann, W. Knoll, Surface-plasmon field-enhanced fluorescence spectroscopy, Colloids Surf. A 171 (2000) 115-130.

[19] R. Roy, J. Kim, J. T. Kellis, A. J. Poulose, Jr., C. R. Robertson, A. P. Gast, Surface plasmon resonance/surface plasmon enhanced fluorescence: An optical technique for the detection of multicomponent macromolecular adsorption at the solid/liquid interface, Langmuir 18 (2002) 6319-6323.

[20] F. Yu, D. F. Yao, W. Knoll, Surface plasmon field-enhanced fluorescence spectroscopy studies of the interaction between an antibody and its surface-coupled antigen, Anal. Chem. 75 (2003) 2610-2617.

[21] T. Neumann, M. L. Johansson, D. Kambhampati, W. Knoll, Surface-plasmon fluorescence spectroscopy, Adv. Funct. Mater. 12 (2002) 575-586.

[22] J. Spinke, M. Liley, H.-J. Guder, L. Angermaier, W. Knoll, Molecular recognition at self-assembled monolayers - the construction of multicomponent multilayers, Langmuir 9 (1993) 1821-1825.

[23] S. Ekgasit, C. Thammacharoen, W. Knoll, Surface plasmon resonance spectroscopy based on evanescent field treatment, Anal. Chem. 76 (2004) 561-568.

[24] S. Ekgasit, C. Thammacharoen, F. Yu, W. Knoll, Evanescent field in surface plasmon resonance and surface-plasmon field-enhanced fluorescence spectroscopies, Anal. Chem. 75 (2004) 2210-2219.

[25] W. N. Hansen, Electric fields produced by propagation of plane coherent electromagnetic radiation in a stratified medium, J. Opt. Soc. Am. 58 (1968) 380-390.

[26] A. Baba, M.-K. Park, R. C. Advincula, W. Knoll, Simultaneous surface plasmon optical and electrochemical investigation of layer-by-layer self-assembled conducting ultrathin polymer films, Langmuir 18 (2002) 4648-4652.

[27] A. G. MacDiarmid, J. C. Chiang, A. F. Richter, N. L. D. Somasiri, A. J. Epstein, in Conducting Polymers; L. Alcacer, Ed.; Reidel, Dordrecht, 1985; pp. 105-120

[28] J. Yue, A. J. Epstein, Synthesis of self-doped conducting polyaniline, J. Am. Chem. Soc. 112 (1990) 2800-2801.

[29] J. H. Cheung, W. B. Stockton, M. F. Rubner, Molecular-level processing of conjugated polymers. 3. layer-by-layer manipulation of polyaniline via electrostatic interactions, Macromolecules 30 (1997) 2712-2716.

[30] A. Baba J. Lübben, K. Tamada, W. Knoll, Optical properties of ultrathin poly(3,4-ethylenedioxythiophene) films at several doping levels studied by in situ electrochemical surface plasmon resonance spectroscopy, Langmuir 19 (2003), 9058-9064.

[31] M. Ferreira, M. F. Rubner, M. F. Molecular-level processing of conjugated polymers. 1. layer-by-layer manipulation of conjugated polyions, Macromolecules 28 (1995) 7107-7114.

[32] N. S. Murthy, L. W. Shacklette, R. H. Baughmann, Effect of charge-transfer on chain dimension in transpolyacetylene, J. Chem. Phys. 87 (1987) 2346-2348.

[33] M. J. Winokur, P. Walmsley, J. Moulton, P. Smith, A. J. Heeger, Structural evolution in iodine-doped poly(3-alkylthiophenes), Macromolecules 24 (1991) 3812-3815.

[34] D. Roy, Surface plasmon resonance spectroscopy of dielectric coated gold and silver film on supporting metal layers: reflectivity formulas in the Kretschmann formalism, Appl. Spectrosc. 55 (2001) 1046-1052.

FIGURE CAPTIONS

Figure 1. (A) A schematic illustration of an SPR experimental setup. (B) Structures of polyaniline (PANI) and sulfonated polyaniline (SPANI). (C) Structures of 3,4-ethylenedioxythiophene (EDOT) and poly(3,4-ethylenedioxythiophene) (PEDOT).

Figure 2. SPR curves of the binding of antibodies onto the surface of SAM with the mole fraction of biotin-terminated thiol of (A) $\chi = 0.1$ and (B) $\chi = 0.04$. The sensor architectures are: (a) Au/SAM; (b) Au/SAM/AF-2F5; (c) Au/SAM (regenerated); (d) Au/SAM/2F5; and (e) Au/SAM/2F5/AF-RaM. Note: AF-2F5 and AF-RaM are fluorophore-labeled antibodies (weakly absorbing dielectrics).

Figure 3. SPR curves of self-assembled PANI/SPANI conducting polymer films with air as an ambient substrate: (a) Au; (b) Au/(PANI/SPANI); (c) Au/(PANI/SPANI)x2; (d) Au/(PANI/SPANI)x3.

Figure 4. SPR curves of ultra thin electropolymerized PEDOT at the coupled wavelengths of (A) 632.8 nm and (B) 1152 nm at various applied potentials: (a) +0.50; (b) –0.20; (c) –0.65; and (d) –1.00 V. SPR curves of the bare gold film under the monomer-free solution of 0.1 M TBAPF6 in acetonitrile are shown (dotted lines).

Figure 5. (A) The resonance condition of a nonabsorbing dielectric film: (**I**) thickness variation of a film with $n_D = 1.45$; refractive index variation for a film with $d_D = 5$ nm thick. The solid lines indicate the resonance angle while the dotted lines (two lines are superimposed) indicate the reflectance minimum. (B) The evanescent field decay profile within the metal film at three different conditions: a, b, and c, defined in (A). The insert

shows the evanescent field integrations at the resonance angles. The layer architecture of the system and the coupled wavelength are shown in the figure. Note: the positions labeled-(b) have the same layer architecture.

Figure 6. (A) SPR curves at various metal film thickness. The resonance conditions (resonance angle and reflectance minimum) at various absorption indices k of the bulk absorbing dielectric with $\hat{n} = 1.346 + ik$: (B) $k = 0.000$; (c) k 0.002; and (d) $k = 0.005$. The simulation parameters are shown. Note: the resonance conditions in (B) are those of the SPR curves in (A).

Figure 7. The evanescent field decay profiles at the resonance angles of the SPR curves: (A) in Figure 2A and (B) in Figure 2B. The dotted lines indicate the metal/dielectric interfaces. The simulation parameters are shown in Table 1. The curve labels are associated with those of Figure 2.

Figure 8. Parameters at the resonance condition as the thickness of the absorbing dielectric film increases (i.e., via thickness increment) for sensors with thickness of the gold film (A) thinner than the optimal thickness and (B) thicker than the optimal thickness. The simulation parameters are shown in Table 1 (i.e., fitting parameters of Figures 2A(b) and 2B(b), respectively) with an increasing thickness of AF-2F5 layer. The y-axes are parameters at the resonance condition (θ_{SPR}: resonance angle; R_{SPR}: reflectance minimum; A_M: absorptance of the metal film; A_D: absorptance of the absorbing dielectric; $A_M + A_D$: the total absorptance; $\left\langle E^2_{z=d_M-} \right\rangle$: evanescent field at the metal/dielectric interface on the metal side and $\left\langle E^2_{z=d_M+} \right\rangle$: that on the dielectric side).

Figure 9. The evanescent field decay profiles at the resonance angles of the SPR curves in Figure 3. The simulation parameters are shown in Table 2. The curve labels are associated with those of Figure 3.

Table 1. Fitting parameter of the observed SPR Curves in Figure 2.

SPR Curve	Layer architecture of the sensor [a]				θ_{SPR} [d]
	Complex Refractive Index ($\hat{n} = n + ik$) Thickness (nm)				
	Au	SAM	AF-2F5 [b] or 2F5	AF-RaM [c]	
Figure 2A(**a**)	**0.139 + i3.607**	**1.500**			56.9°
	42.00	1.60			
Figure 2A(**b**)	**0.139 + i3.607**	**1.500**	**1.450 + i0.019** [b]		57.6°
	42.00	1.60	5.00		
Figure 2A(**c**)	**0.139 + i3.607**	**1.500**			56.9°
	42.00	1.60			
Figure 2A(**d**)	**0.139 + i3.607**	**1.500**	**1.450**		57.8°
	42.00	1.60	6.32		
Figure 2A(**e**)	**0.139 + i3.607**	**1.500**	**1.450**	**1.450 + i0.017**	58.3°
	42.00	1.60	6.32	4.40	
Figure 2B(**a**)	**0.198 + i3.580**	**1.500**			56.9°
	51.00	1.40			
Figure 2B(**b**)	**0.198 + i3.580**	**1.500**	**1.450 + i0.034** [b]		57.4°
	51.00	1.40	4.05		
Figure 2B(**c**)	**0.198 + i3.580**	**1.500**			56.9°
	51.00	1.40			
Figure 2B(**d**)	**0.198 + i3.580**	**1.500**	**1.450**		57.6°
	51.00	1.40	5.15		
Figure 2B(**e**)	**0.198 + i3.580**	**1.500**	**1.450**	**1.450 + i0.032**	58.2°
	51.00	1.40	5.15	4.33	

[a] An LASFN9 Glass (n = 1.845) is employed as a coupling prism while the HBS-EP buffer (1.333) is employed as a semi-infinitely thick nonabsorbing ambient substrate.

[b] Alexa Fluor 647-labeled mouse monoclonal antibody 2F5 (isotype IgG$_{1,k}$).

[c] Alexa Fluor 647-labeled rabbit anti-mouse IgG.

[d] The measured angle of incidence θ has a resolution of 0.1° near the resonance angle.

Table 2. Fitting parameter of the observed SPR Curves in Figure 3.

SPR Curve	Layer architecture of the sensor [a]					θ_{SPR} [c]
	Complex Refractive Index ($\hat{n} = n + ik$) Thickness (nm)					
	Cr [b]	Au	PANI/SPANI	PANI/SPANI	PANI/SPANI	
Figure 3a	**3.66 + i4.36**	**0.20 + i3.48**				43.1^{o}
	0.70	55.30				
Figure 3b	**3.66 + i4.36**	**0.20 + i3.48**	**1.50 + i0.22**			44.4^{o}
	0.70	55.30	6.00			
Figure 3c	**3.66 + i4.36**	**0.20 + i3.48**	**1.50 + i0.22**	**1.50 + i0.22**		46.3^{o}
	0.70	55.30	6.00	7.40		
Figure 3d	**3.66 + i4.36**	**0.20 + i3.48**	**1.50 + i0.22**	**1.50 + i0.22**	**1.50 + i0.22**	48.5^{o}
	0.70	55.30	6.00	7.40	7.20	

[a] A BK7 Glass ($n = 1.515$) is employed as a coupling prism while air ($n = 1.00$) is employed as a semi-infinitely thick nonabsorbing ambient substrate.

[b] The complex refractive index is obtained from reference 34.

[c] The measured angle of incidence θ has a resolution of 0.1^{o} near the resonance angle.

Table 3.   Fitting parameter of the observed SPR Curves in Figure 4.

SPR Curve	Layer architecture of the sensor [a]		θ_{SPR} [b]
	Complex Refractive Index ($\hat{n} = n + ik$) Thickness (nm)		
	Au	PEDOT	
Figure 4A(**a**)	0.198 + i3.569		58.3°
	40.00		
Figure 4A(**b**)	0.198 + i3.569	1.328 + i0.049	58.0°
	40.00	22.50	
Figure 4A(**c**)	0.198 + i3.569	1.343 + i0.067	58.5°
	40.00	22.10	
Figure 4A(**d**)	0.198 + i3.569	1.404 + i0.178	60.4°
	40.00	21.30	
Figure 4A(**e**)	0.198 + i3.569	1.406 + i0.341	61.9°
	40.00	19.70	
Figure 4B(**a**)	0.230 + i8.066		51.2°
	40.00		
Figure 4B(**b**)	0.230 + i8.066	1.230 + i0.239	51.1°
	40.00	22.50	
Figure 4B(**c**)	0.230 + i8.066	1.322 + i0.170	51.3°
	40.00	22.10	
Figure 4B(**d**)	0.230 + i8.066	1.445 + i0.083	51.7°
	40.00	21.30	
Figure 4B(**e**)	0.230 + i8.066	1.514 + i0.026	51.7°
	40.00	19.70	

[a] An LASFN9 Glass ($n = 1.845$) is employed as a coupling prism while the 0.1 M TBAPF6 in acetonitrile ($n = 1.340$) is employed as a semi-infinitely thick nonabsorbing ambient substrate..

[b] The measured angle of incidence θ has a resolution of 0.1° near the resonance angle.
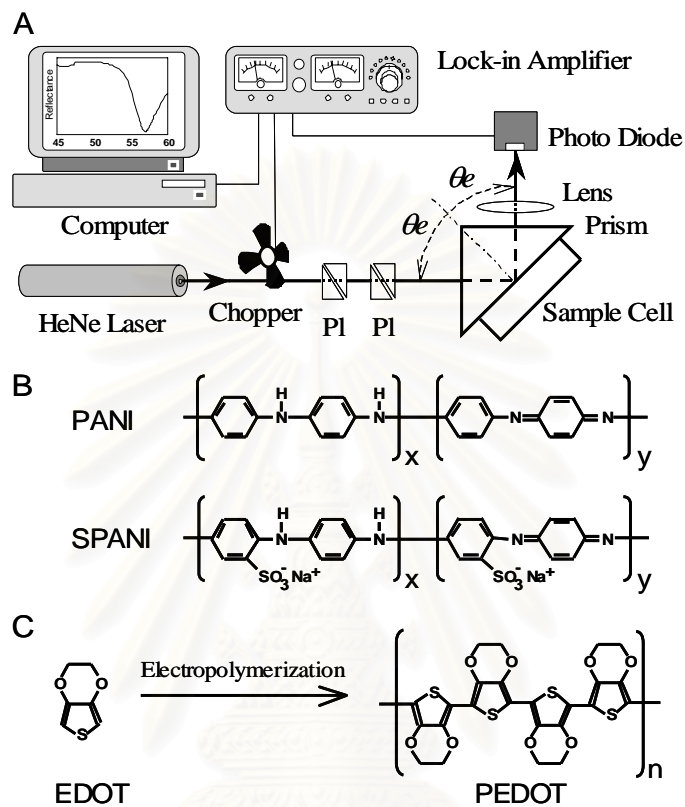
Figure 1. (A) A schematic illustration of an SPR experimental setup. (B) Structures of polyaniline (PANI) and sulfonated polyaniline (SPANI). (C) Structures of 3,4-ethylenedioxythiophene (EDOT) and poly(3,4-ethylenedioxythiophene) (PEDOT).
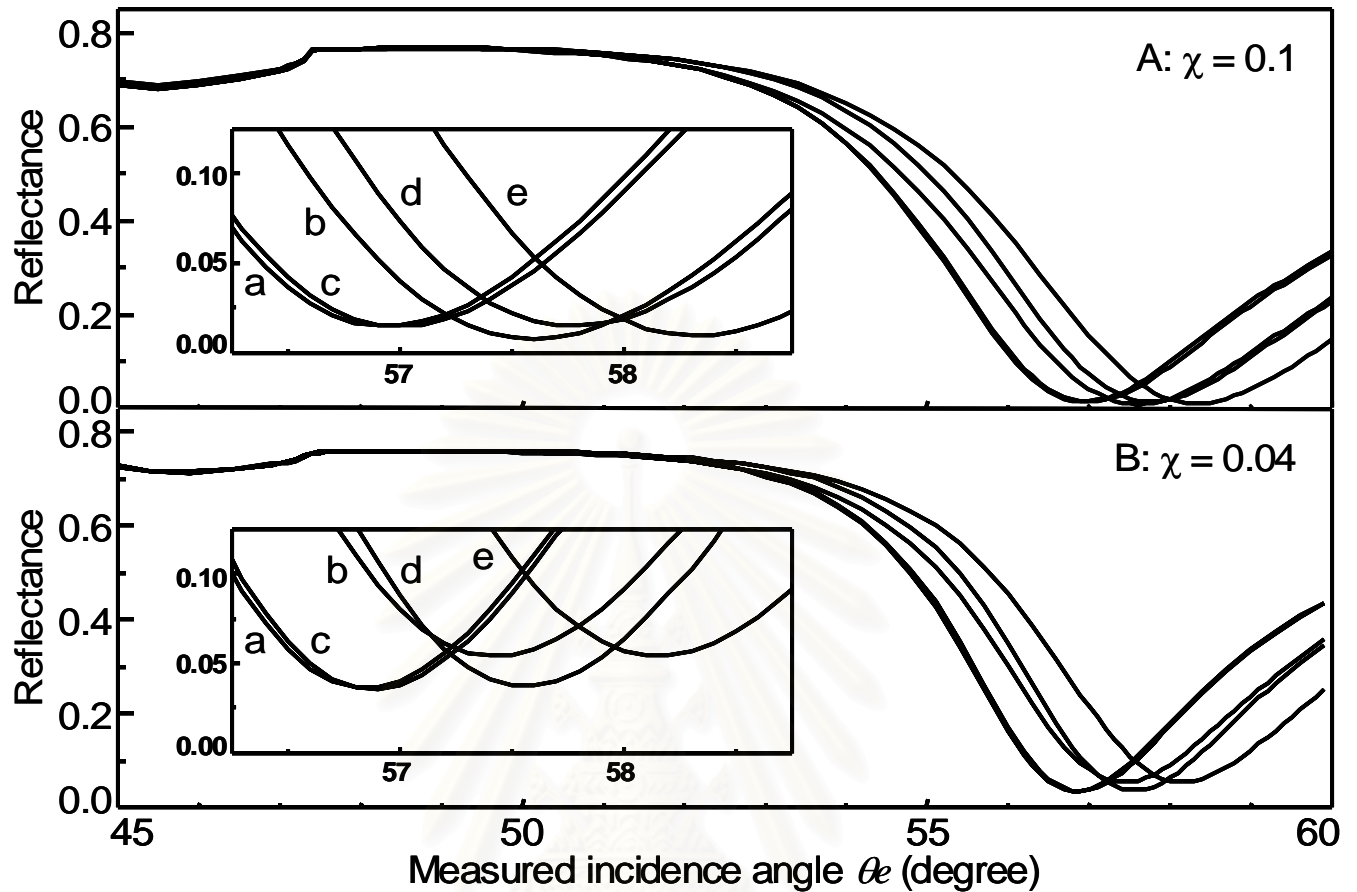
Figure 2. SPR curves of the binding of antibodies onto the surface of SAM with the mole fraction of biotin-terminated thiol of (A) χ = 0.1 and (B) χ = 0.04. The sensor architectures are: (a) Au/SAM; (b) Au/SAM/AF-2F5; (c) Au/SAM (regenerated); (d) Au/SAM/2F5; and (e) Au/SAM/2F5/AF-RaM. Note: AF-2F5 and AF-RaM are fluorophore-labeled antibodies (weakly absorbing dielectrics).
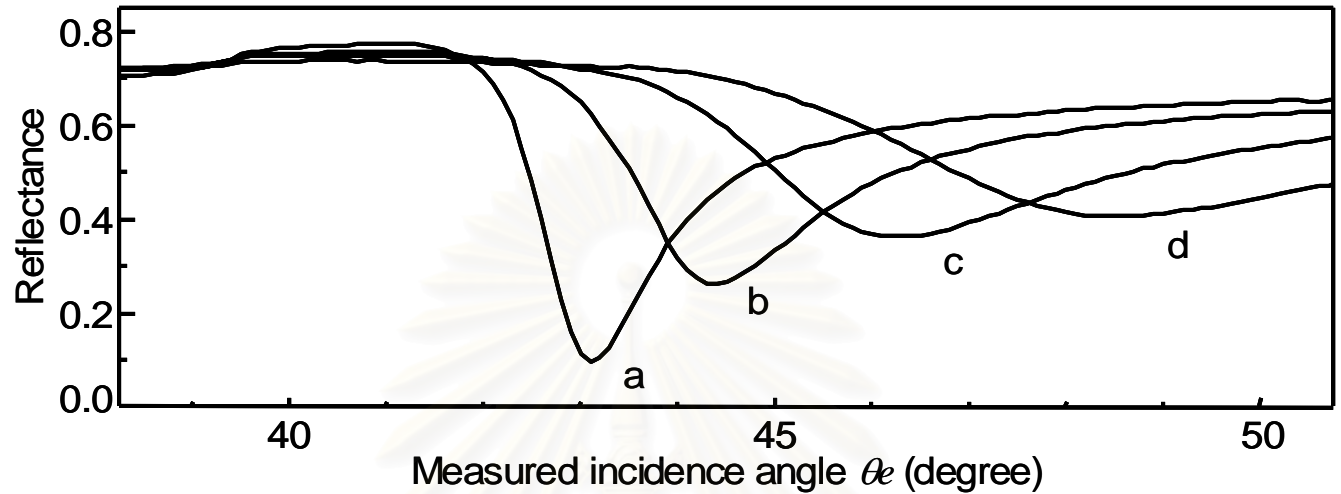
Figure 3. SPR curves of self-assembled PANI/SPANI conducting polymer films with air as an ambient substrate: (a) Au; (b) Au/(PANI/SPANI); (c) Au/(PANI/SPANI)x2; (d) Au/(PANI/SPANI)x3.
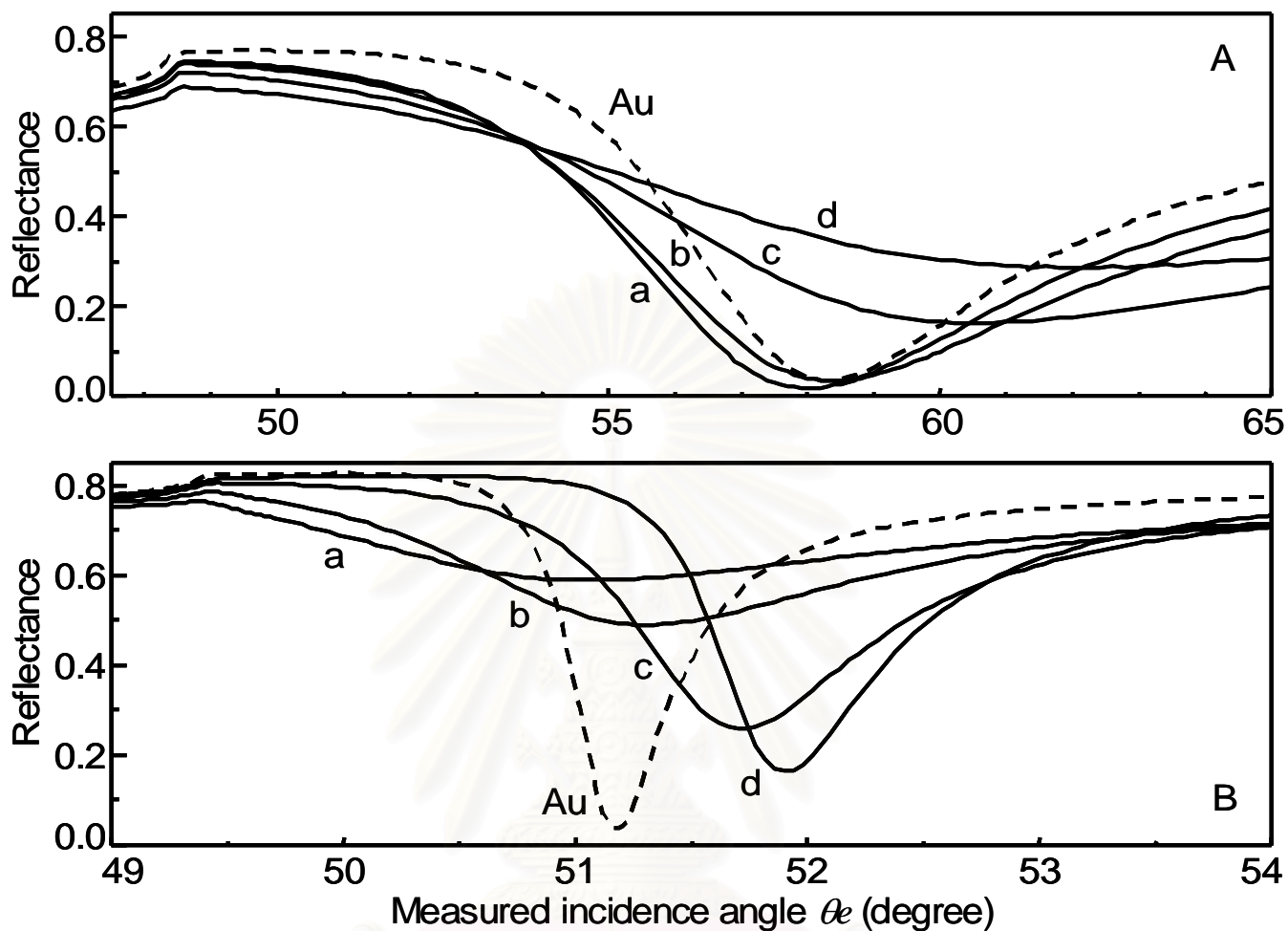
Figure 4. SPR curves of ultra thin electropolymerized PEDOT at the coupled wavelengths of (A) 632.8 nm and (B) 1152 nm at various applied potentials: (a) +0.50; (b) –0.20; (c) –0.65; and (d) –1.00 V. SPR curves of the bare gold film under the monomer-free solution of 0.1 M TBAPF6 in acetonitrile are shown (dotted lines).
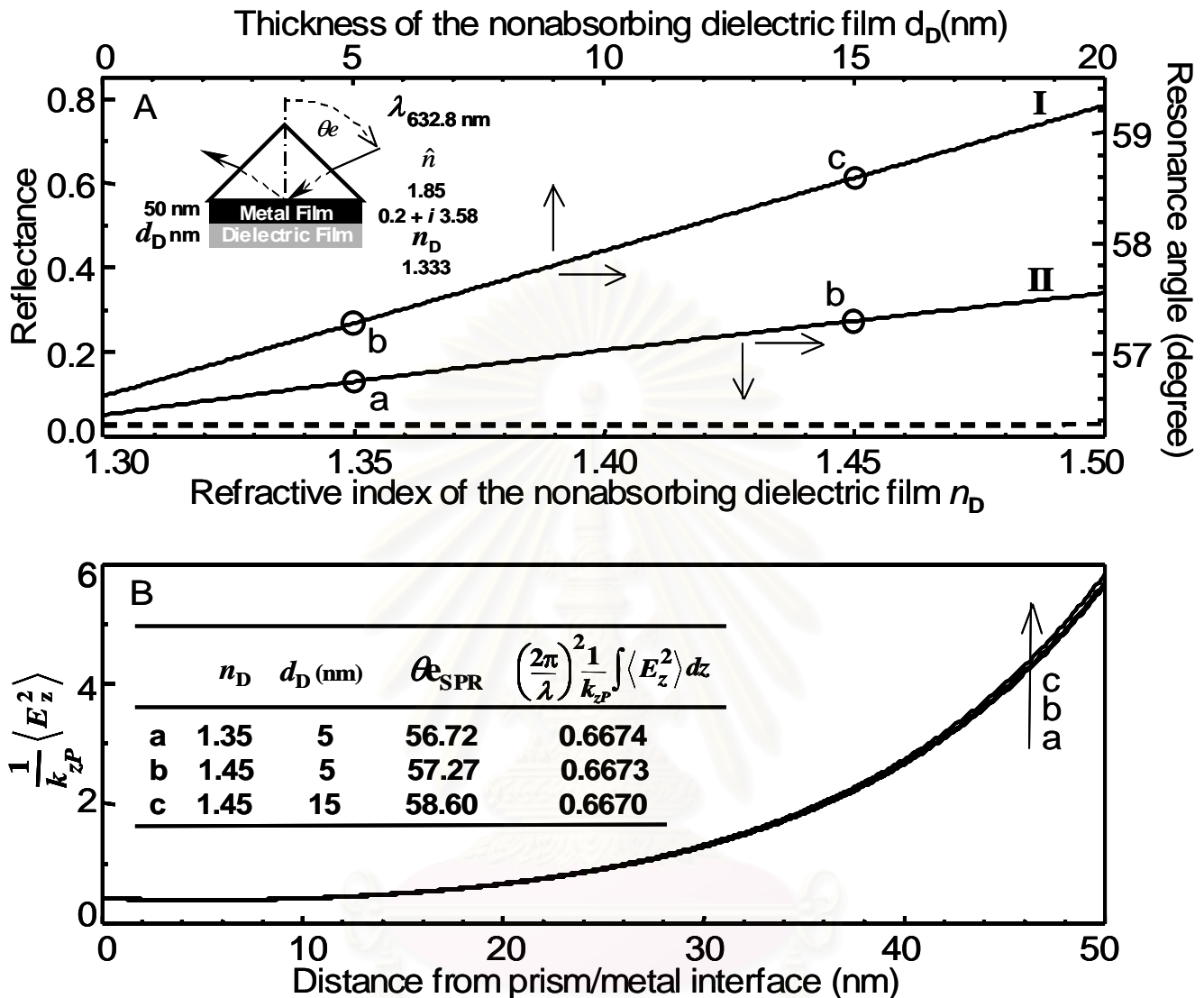
Figure 5. (A) The resonance condition of a nonabsorbing dielectric film: (**I**) thickness variation of a film with n_D = 1.45; refractive index variation for a film with d_D = 5 nm thick. The solid lines indicate the resonance angle while the dotted lines (two lines are superimposed) indicate the reflectance minimum. (B) The evanescent field decay profile within the metal film at three different conditions: a, b, and c, defined in (A). The insert shows the evanescent field integrations at the resonance angles. The layer architecture of the system and the coupled wavelength are shown in the figure. Note: the positions labeled-(b) have the same layer architecture.
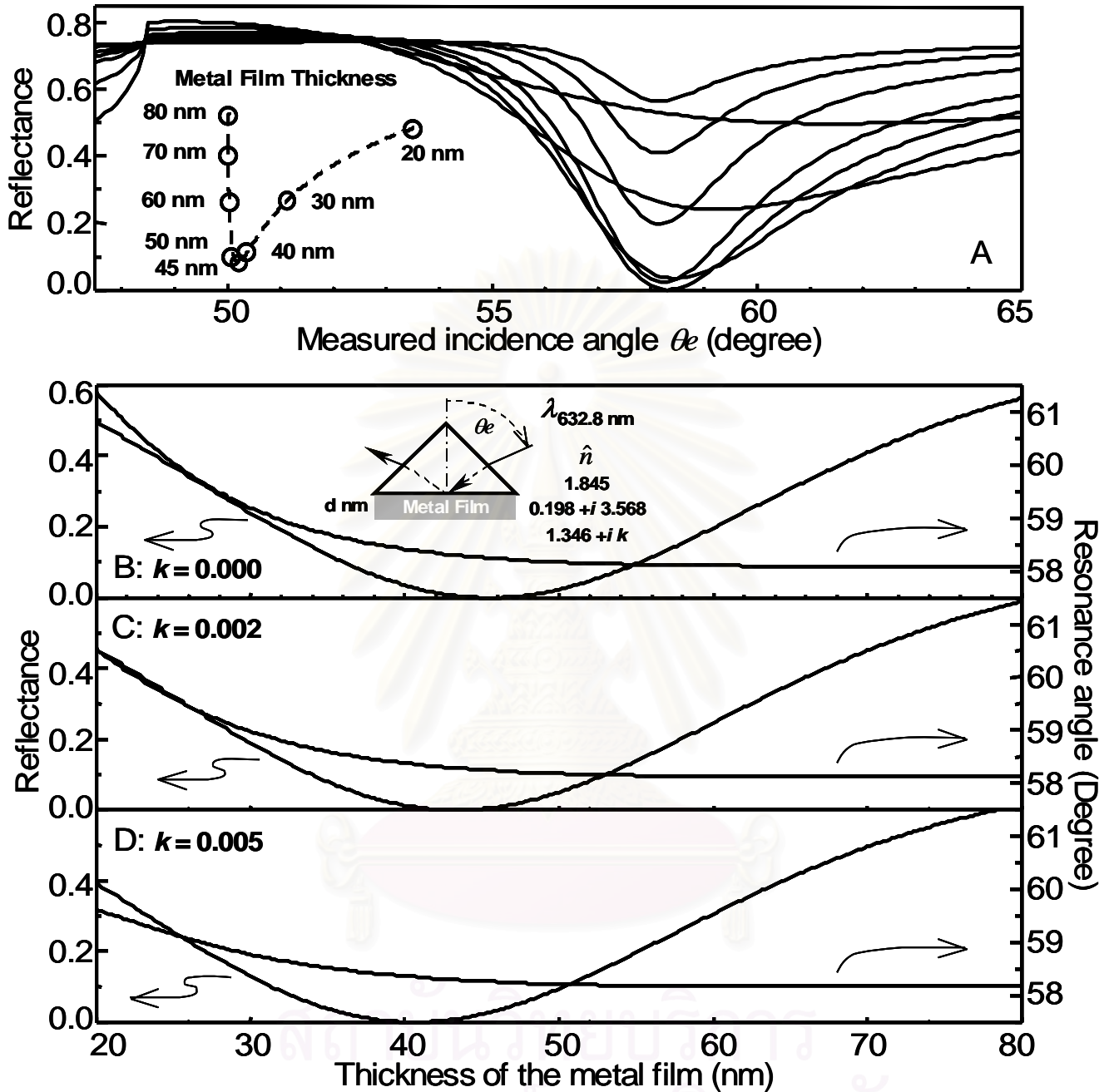
Figure 6. (A) SPR curves at various metal film thickness. The resonance conditions (resonance angle and reflectance minimum) at various absorption indices k of the bulk absorbing dielectric with $\hat{n} = 1.346 + ik$: (B) k = 0.000; (c) k 0.002; and (d) k = 0.005. The simulation parameters are shown. Note: the resonance conditions in (B) are those of the SPR curves in (A).

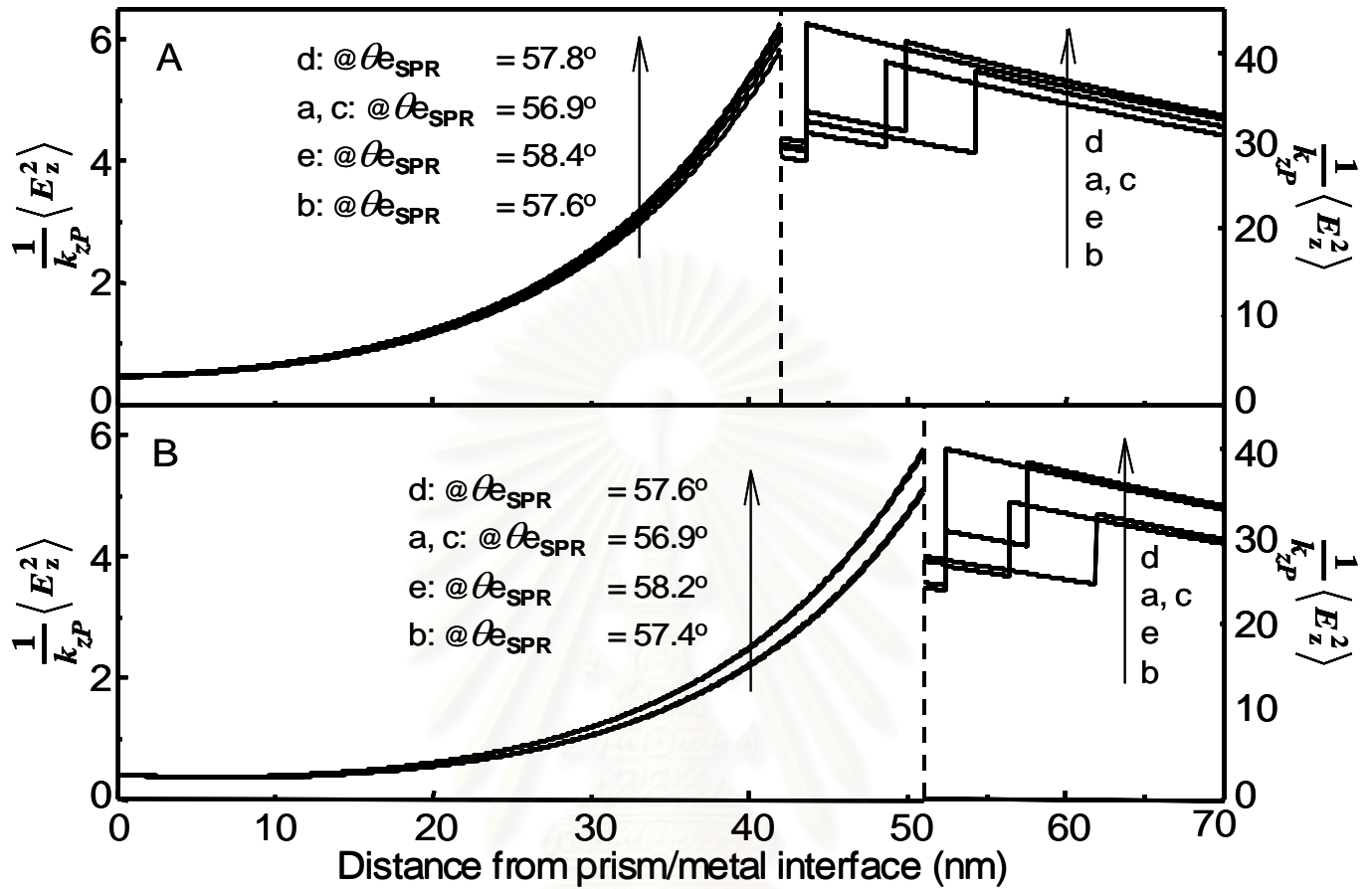Resonance Shifts in SPR Curves: S. Ekgasit, A. Tangcharoenbumrungsuk, F. Yu, A. Baba, and W. Knoll .

Figure 7. The evanescent field decay profiles at the resonance angles of the SPR curves: (A) in Figure 2A and (B) in Figure 2B. The dotted lines indicate the metal/dielectric interfaces. The simulation parameters are shown in Table 1. The curve labels are associated with those of Figure 2.
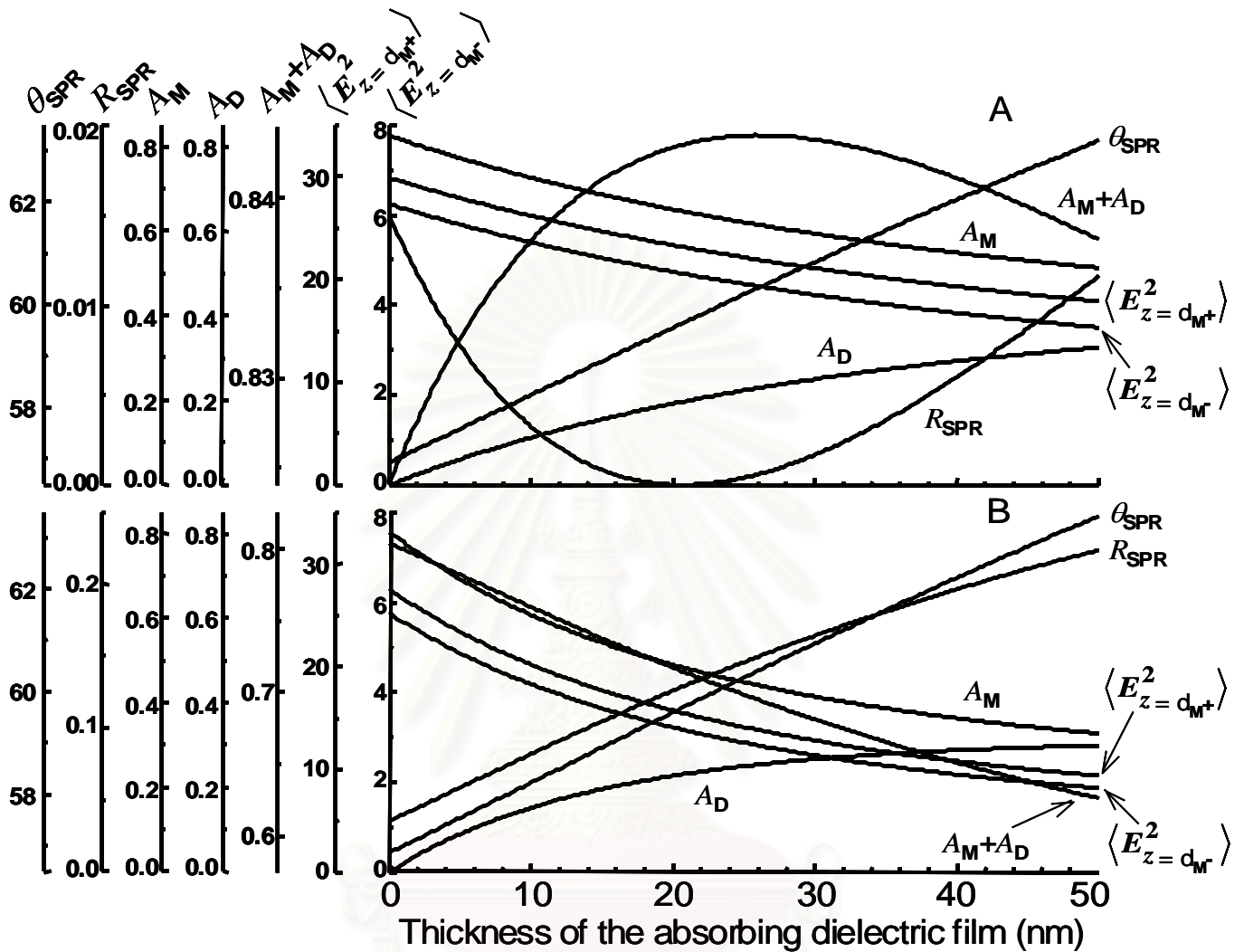
Figure 8. Parameters at the resonance condition as the thickness of the absorbing dielectric film increases (i.e., via thickness increment) for sensors with thickness of the gold film (A) thinner than the optimal thickness and (B) thicker than the optimal thickness. The simulation parameters are shown in Table 1 (i.e., fitting parameters of Figures 2A(b) and 2B(b), respectively) with an increasing thickness of AF-2F5 layer. The y-axes are parameters at the resonance condition (θ_{SPR}: resonance angle; R_{SPR}: reflectance minimum; A_M: absorptance of the metal film; A_D: absorptance of the absorbing dielectric; A_M+A_D: the total absorptance; $\left\langle E^2_{z=d_M-} \right\rangle$: evanescent field at the metal/dielectric interface on the metal side and $\left\langle E^2_{z=d_M+} \right\rangle$: that on the dielectric side).

Resonance Shifts in SPR Curves: S. Ekgasit, A. Tangcharoenbumrungsuk, F. Yu, A. Baba, and W. Knoll.
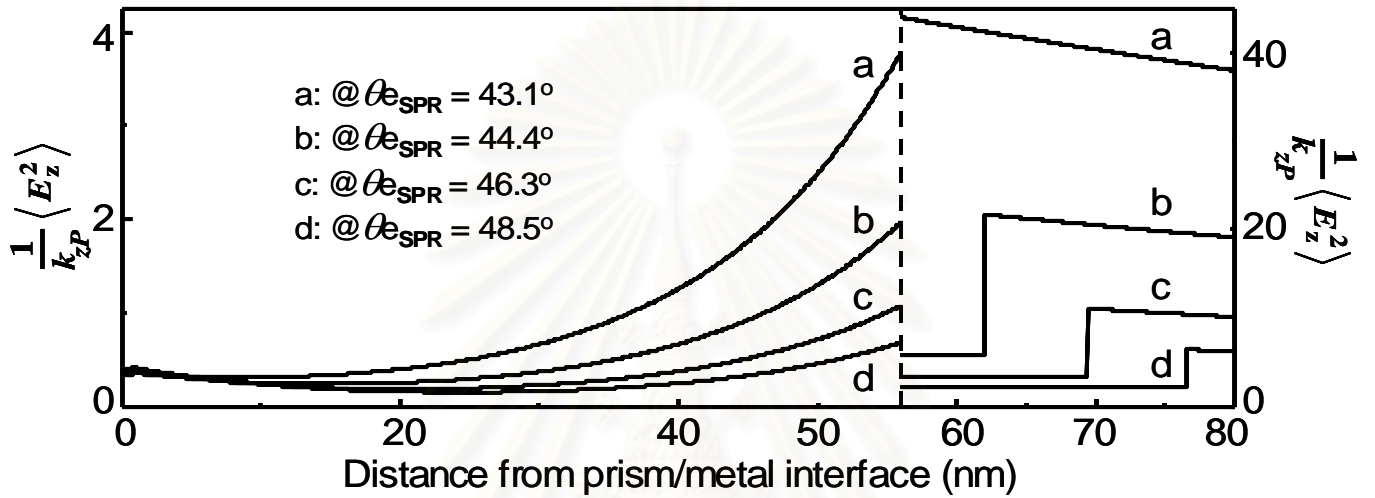
Figure 9. The evanescent field decay profiles at the resonance angles of the SPR curves in Figure 3.

The simulation parameters are shown in Table 2. The curve labels are associated with those of Figure 3.

VITA

Name: Arunchai Tangcharoenbumrungsuk

Date of Birth: December 15, 1969

Birth Place: Phetchaburi, Thailand

Marital Status: Married

Current Address:

77/5 M 7 Timroungwes village

Boromratchananee road,

Kwang Salathammasorp,

Khet Thaveewattana,

Bangkok 10170

Phone: 02-441-2391

Education:

Ph.D. Candidate, Chemistry, September 2004, Chulalongkorn University, Bangkok.

Master of Science, Chemistry, October 1999, Chulalongkorn University, Bangkok.

Bachelor of Science, Chemistry, May 1993, Mahidol University, Bangkok.

Award:

Admiring reward in computer programmer in subdivision of the program for development of science and technology in National Software Contest 2004 and The Third Thailand ICT Contest Festival which prepared by National Electronics and Computer Technology Center (NECTEC) THAILAND.

Professional Experience:

11/95-04/96   *Chemist*, Sithiporn Associates Co., Ltd. 101 Sirinthorn, Bangplud, Bangkok.

05/93-05/95   *Chemistry Lecturer*, Rajabhat Institute Suan Dusit, Ratchasrima road, Dusit, Bangkok.